NUMERICAL AND EXPERIMENTAL PERFORMANCE EVALUATION OF TWO MULTI-STAGE CLOUD COLLECTORS

Derek J. Straub and Jeffrey L. Collett, Jr.
Department of Atmospheric Science
Colorado State University
Fort Collins, CO

Research Supported by:
The National Science Foundation (ATM-9509596) and the
U.S. Environmental Protection Agency National Center for
Environmental Research and Quality Assurance (R82-3979-010)

January, 1999

Colorado State University

DEPARTMENT OF ATMOSPHERIC SCIENCE

PAPER NO. 676

NUMERICAL AND EXPERIMENTAL PERFORMANCE EVALUATION OF TWO MULTI-STAGE CLOUD COLLECTORS

By:

Derek J. Straub

and

Jeffrey L. Collett, Jr.

Department of Atmospheric Science

Research Supported by:

The National Science Foundation (ATM-9509596) and the

U.S. Environmental Protection Agency National Center for

Environmental Research and Quality Assurance (R82-3979-010)

January, 1999

ABSTRACT

NUMERICAL AND EXPERIMENTAL PERFORMANCE EVALUATION OF TWO MULTI-STAGE CLOUD COLLECTORS

An evaluation of the collection characteristics of two new multi-stage cascade inertial impactors designed for size-resolved cloud drop collection has been performed. The FROSTY supercooled cloud collector is intended for the collection of supercooled cloud drops in a winter environment in three independent size fractions with stage 50% cut diameters of 15 μm, 10 μm, and 4 μm. The CSU 5-Stage cloud collector is designed for sampling warm clouds in five distinct fractions on five stages that have desired 50% cut diameters of 30, 25, 15, 10, and 4 μm.

Two approaches were selected for the evaluation of the FROSTY and CSU 5-Stage cloud collectors. Numerical simulations provided a visualization of the air flow patterns and drop trajectories through the collectors while experimental laboratory calibrations provided a quantitative analysis of true collection performance. For each of these methods, 50% cut diameters, efficiency curves, and wall losses for each stage of the FROSTY and CSU 5-Stage collectors were derived.

The experimental calibration work indicated that distinct fractions of cloudwater are collected in each stage of the FROSTY and CSU 5-Stage collectors. At laboratory conditions, the experimentally determined 50% cut diameters for the three stages of the FROSTY supercooled cloud collector were 19, 11.5, and 5 μm. Drop losses to the interstage wall surfaces in the FROSTY collector peaked at approximately 35% for 16 μm drops and were lower for larger and

smaller drop sizes. For operation at design conditions of 3000 m elevation and -4° C, the 50% cut diameters are expected to decrease to 17, 10.5, and 4.5 μm.

The experimentally determined 50% cut diameters, measured at laboratory conditions, for the CSU 5-Stage cloud collector were 25.5, 29, 17.5, 10.5, and 4.5 μm for stages 1 through 5, respectively. Wall losses tended to be higher than those for the FROSTY cloud collector across the drop size range under consideration. Losses peaked at nearly 45% for drops between 10 and 18 μm in diameter and decreased to about 20% at the largest and smallest drop sizes. 50% cut diameters are expected to remain essentially unchanged for CSU 5-Stage collector operation at sea level design conditions.

Numerical modeling of the air flow patterns as well as drop trajectories through the FROSTY and CSU 5-Stage cloud collectors was performed with the commercially available Computational Fluid Dynamics (CFD) software package FLUENT, from Fluent, Inc. FLUENT offered two alternatives for the calculation of drop trajectories. Trajectory simulations based on the average continuous phase (air) velocity field as well as trajectory simulations which included the effects of statistically derived turbulent velocity fluctuations on drop motion were performed. Drop collection patterns based on these types of trajectory calculations were used to generate collection efficiency curves.

Comparisons were made between the numerically predicted collection efficiency curves and efficiency curves established through experimental calibration. These comparisons indicated that the inclusion of turbulent fluctuation effects on drop motion provided better agreement with experimental observations than trajectories based only on average flow field velocities. However, the use of velocity fluctuations defined by default parameters also produced unrealistic losses to wall surfaces for small drop sizes. The parameters controlling turbulent velocity fluctuation effects on drop motion were examined in an effort to provide better agreement between the numerical and experimental results. Despite this shortcoming, numerically derived 50% cut

diameters and overall collection efficiency curve shapes, for drop trajectories including turbulent velocity fluctuations, agreed reasonably well with experimental observations in most cases.

ACKNOWLEDGMENTS

We would like to thank Dr. Sonia Kreidenweis and Dr. Robert Meroney for contributing insight and valuable suggestions that helped guide this research work. We would also like to express our gratitude to the members of the atmospheric chemistry research group for providing advice and technical assistance, especially Katharine Moore, Eli Sherman, and Katherine Hoag.

This work was supported financially by the National Science Foundation (ATM-9509596) and the U.S. Environmental Protection Agency National Center for Environmental Research and Quality Assurance (R82-3979-010).

TABLE OF CONTENTS

LIST OF FIGURES

LIST OF TABLES

1 Introduction

1.1 Chemical processing in cloud drops

The role that clouds play in the processing of atmospheric aerosols and trace gases is recognized as an important component of atmospheric chemistry. In the presence of clouds, aerosols and trace gases can undergo transformations that substantially alter their concentrations and chemical compositions. Soluble trace gases can be absorbed into cloud drops, while aerosols can serve as cloud condensation nuclei (CCN) or be incorporated through other scavenging processes. Once these species are integrated into cloud drops, a number of fates are possible. For example, chemical reactions within the cloud drops can modify the chemical form of the species. These reactions in the aqueous phase can often proceed more rapidly than in the gas phase, accelerating the rate of transformation.

Depending on ambient conditions, after a cloud drop is formed it may or may not be incorporated into precipitation. If the cloud drop is transferred into precipitation, the aerosols and trace gases that it contains may be removed from the atmosphere along with the precipitation as it falls to the earth. Removal of a species by this mechanism may occur much more quickly than if it remains in its original form as a trace gas or dry aerosol. Cloud drops that evaporate before being incorporated into precipitation can result in the production of new aerosol particles with altered chemical or size characteristics. In this case, the drying process can leave behind an aerosol that has been modified from the original aerosol through aqueous phase chemical reaction or through combination of multiple aerosol particles that have been scavenged into the individual drops. Aerosol particles scavenged by cloud drops can also be combined as a result of cloud drop

interactions. This ability of clouds to produce extensive chemical and physical modifications to aerosols and trace gases has resulted in ongoing research in this area.

1.2 Effects of chemical heterogeneity

The processing of trace gases and aerosols that takes place in cloud drops may not be identical for every cloud drop size. Researchers have predicted and observed that solute concentrations and compositions can vary with drop size due to complex and often competing factors such as differences in CCN, varying drop growth rates, and differences in trace gas uptake (Ogren and Charlson, 1992). These chemical variations with drop size can result in variations in the type and extent of aerosol and trace gas processing from one drop size to another.

A study by Collett et al. (1994) indicates that the rate of sulfur oxidation in a cloud drop can be dependent on drop size due to a variation of acidity with drop size. The findings show that small drops (smaller than 10 to 23 μm) sampled in a variety of environments typically had a lower pH than large drops (larger than 10 to 23 μm). Because the rate of aqueous sulfur oxidation by the ozone and trace metal catalyzed oxygen pathways increases nonlinearly with increasing pH (Hoffmann, 1986; Ibusuki and Takeuchi, 1987), large drops will have substantially higher oxidation rates than small drops. If calculations of sulfur oxidation rates are based on bulk cloudwater properties, considerable under prediction of the oxidation rates will result. Under prediction by factors of 1.5 to 9 times (Hoag, 1997) have been estimated in California's San Joaquin Valley. Rao and Collett (1998) have illustrated that covariance of metal catalyst concentrations and pH can exert an even greater effect than the pH variations alone.

In addition to sulfur oxidation rate variation with drop size, solute composition has also been observed to vary with drop size by Bator and Collet (1997). In this study, small drops were found to be enriched in sulfate, nitrate, and ammonium, while the large drops tended to be enriched in calcium, magnesium, and sodium. These differences in composition between the large and small fraction of cloud drops were attributed to the fact that small cloud drops tend to

form on accumulation mode aerosol while large cloud drops form on coarse mode aerosol. The accumulation mode aerosol is usually composed of nitrate, sulfate, and ammonium and the coarse mode aerosol is usually composed of mechanically generated sodium, calcium, chloride, and magnesium particles. This partitioning of species between different populations of cloud drops may have several consequences. Because the deposition rate of cloud drops to the ground and other surfaces is dependent on drop size, certain chemical species may be preferentially removed from the atmosphere (Hoag et al., 1999). Similarly, the efficiency with which cloud drops are scavenged by precipitation will be dependent on the size of the cloud drops, again resulting in the possibility of preferential removal of certain chemical species from the atmosphere (Xu et al., 1999).

1.3. Cloudwater collection approaches

A number of approaches have been used in the past to collect cloudwater for investigations of the chemical composition and aerosol processing capabilities of cloudwater. Most of these approaches use some form of inertial impaction as the collection method. Collection by inertial impaction is accomplished by accelerating air containing cloud drops toward a surface, such as a plate or a rod. As the air stream impinges on the surface, it is forced to flow around the surface. When this happens, cloud drops larger than a critical size that are being transported by the air stream will possess too much inertia to remain with the air as it flows past the surface. These drops deviate from the air streamlines and impact the surface while drops smaller than the critical diameter will remain with the air stream (see Figure 1.1). This critical diameter is referred to as the cut size or cut diameter, and is determined by the physical configuration of the impactor. After a sufficient duration, enough drops will accumulate on the surface for chemical or other analysis to be possible. The method of accelerating the air past a surface can be accomplished by simply using the motion of the ambient wind to provide air flow past a collection surface or by employing a pump to draw air at a constant rate past a collection

surface. These are referred to as passive and active collectors, respectively. The impaction surface is commonly a flat plate, as illustrated in Figure 1.1, or a cylinder, as used in strand-based collectors.

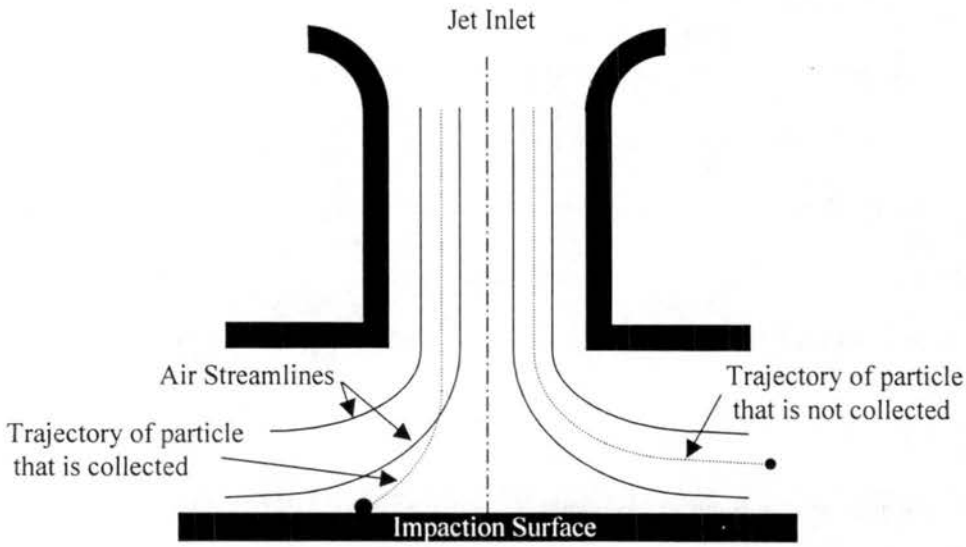

Figure 1.1 Trajectories of collected and uncollected particles in an inertial impactor.

A number of parameters are useful when describing the collection characteristics of an inertial impactor. The efficiency with which drops are collected by an inertial impactor varies by drop size. A curve depicting this variation of efficiency with drop size is referred to as a collection efficiency curve. An ideal impactor would collect no drops smaller than the cut diameter and 100% of the drops larger than the cut diameter. The collection efficiency curve for an ideal impactor would therefore appear as a step function (see Figure 1.2). This would provide the sharpest possible distinction between the population of drops that are collected and those that are not collected. Although this is the objective when designing an impactor, actual collectors do not achieve this goal due to nonidealities such as incomplete sampling of the air, turbulent dispersion, and interception. Some fraction of drops that are smaller than the cut diameter will be collected while another fraction of drops larger than the cut diameter will be missed. This behavior in a real impactor results in a collection efficiency curve that is not a step function, but

instead has an "S" shape (see Figure 1.2). The diameter that corresponds to a collection efficiency of 50% is referred to as the 50% cut diameter.

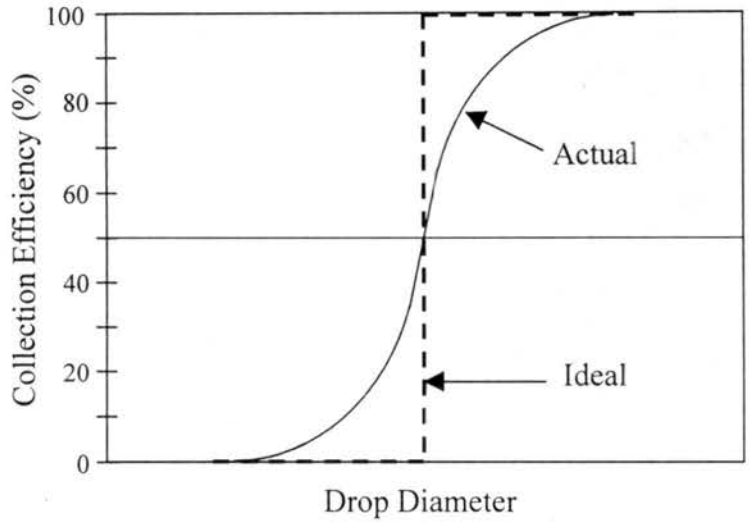

Figure 1.2 Characteristic collection efficiency curves for an inertial impactor.

Use of a single inertial impactor for the collection of cloudwater yields a single population of collected cloud drops, limiting the analysis that can be performed to quantities that are averaged over that cloud drop size range. When an investigation into chemical variations across the drop size spectrum is desired, cascade inertial impactors have frequently been used in the past to provide size-resolved measurements. Cascade inertial impactors collect multiple independent size fractions of cloudwater simultaneously by placing multiple inertial impactors in series. Air is drawn into the inlet of a cascade impactor and accelerated toward a collection surface where drops larger than a predetermined size are collected. After the largest fraction of drops is removed from the air stream, the air is then further accelerated toward a second collection surface where a size fraction of smaller drops will be collected. This process of directing the air flow past additional collection surfaces while continuing to accelerate it will result in the collection of additional smaller size fractions of cloudwater. The number of fractions

into which the total drop population can be divided may be limited by the cloud's available liquid water content, such that sufficient sample can be collected in each fraction in a time period that allows for adequate resolution of composition changes in time. Previous cascade inertial impactors typically have had two or three stages to collect two or three size fractions of cloudwater. The two collectors that are the focus of this research work are both used to investigate size dependent chemical variations in cloud drop chemistry and consist of multiple stages using the principles of cascade inertial impaction.

1.3.1 Previous bulk cloudwater collectors

Two cloudwater collectors based on modifications to the Caltech Active Strand Cloudwater Collector (CASCC) have traditionally been used in the past to collect bulk cloudwater samples for chemical analysis (Demoz et al., 1996). They are the CASCC2 and the Caltech Heated Rod Cloudwater Collector (CHRCC). Both are similar in design, relying on inertial impaction to collect cloud drops on strands or cylinders mounted within the collectors. They are active, requiring a fan to provide the necessary air flow over the collection surfaces. Each of the collectors has been altered from the original CASCC design to reflect the differences in their intended use.

The CASCC2, seen in Figure 1.3, is a compact version of the CASCC. Whereas the original CASCC measured 30 cm by 30 cm by 90 cm, the CASCC2 measures 18 cm by 18 cm by 60 cm. Air is drawn into the collector at a rate of 5.8 m^3/min by a fan located at the back of the unit. The air passes over six rows of 0.508 mm diameter Teflon strands which serve as collection surfaces. The strands are oriented at an angle with respect to the inlet to promote the flow of accumulated cloud drops downward into a Teflon trough that drains into a removable sample bottle. With a 50% cut diameter of 3.5 μm for this arrangement, drops of nearly all available sizes are collected, providing a bulk cloudwater sample for analysis. The CASCC2 collector is capable of collecting large quantities of cloudwater, but because they are bulk samples,

subsequent analysis can not provide any information regarding the nature of chemical variations with drop size that may exist.

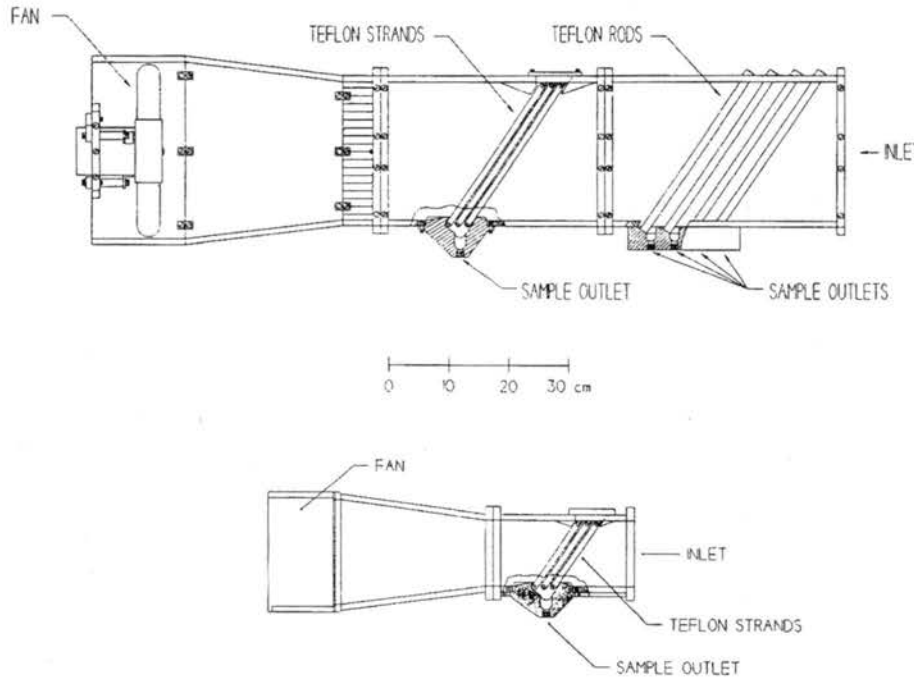

Figure 1.3 The size-fractionating Caltech Active Stand Cloudwater Collector (sf-CASCC) (top) collects two independent size fractions of cloudwater. The CASCC2 (bottom) collects bulk cloudwater samples (from Demoz et al., 1996).

The CHRCC is identical in most respects to the CASCC2. However, the CHRCC is intended for sampling wintertime clouds. The drops that comprise these clouds are supercooled, freezing immediately upon contact with a surface. Because of this feature, if the Teflon strand collection surfaces of the CASCC2 were used, frozen cloud drops would simply accumulate on the strands with no mechanism for removal. In place of the Teflon strands, therefore, the CHRCC uses stainless steel rods that can be heated. When heat is applied to the rods for a brief interval after a collection period, the accumulated frozen cloud drops melt and flow down the rods into a Teflon trough where they are funneled into a collection bottle. The CHRCC operates at the same 5.8 m^3/min flow rate as the CASCC2. However, because the metal collection rods are 3.2 mm in diameter and are placed farther apart, the 50% cut diameter is raised to 9μm.

1.3.2 Previous size-resolved cloudwater collectors

While the CASCC2 and CHRCC perform admirably to provide large volumes of cloudwater in relatively short intervals for analysis, more attention is being focused on the importance of investigating the chemical variations that occur with drop size and the relationships that those variations have on cloud processing. Therefore, the emphasis of more recent cloudwater collector development has been on the ability to collect cloud drops in multiple size ranges that span a portion of or the entire drop size distribution. A number of such devices that have been designed, built, and used in field studies have been cited in the literature.

The original single stage CASCC, which provided the basis for the CASCC2 and CHRCC, as described above, was also modified into a two-stage version in order to examine possible variations in chemical composition with drop size. This new variant of the CASCC is called the size-fractionating CASCC (sf-CASCC) (Demoz et al., 1996; Munger et al., 1989). The sf-CASCC, as seen in Figure 1.3, is identical to the original CASCC, but has a size fractionating inlet in place of the original rain hood inlet. The size-fractionating inlet consists of four rows of 12.7 mm diameter Teflon rods that are inclined at an angle matching that of the Teflon strands. As air enters the collector, the Teflon rods collect large cloud drops through inertial impaction, removing that fraction of drops from the air stream before it reaches the smaller 0.508 μm Teflon strands. Design calculations for the sf-CASCC indicate a 50% cut diameter of 23 μm for the sf-CASCC inlet (Demoz et al., 1996). Recent numerical modeling of the sf-CASCC performance, however, suggests the cut diameter may actually be several microns smaller as a result of flow focusing. From the remaining population of drops, the Teflon strands then collect drops with a 50% cut diameter of 4 μm to provide a second, independent fraction of cloudwater. These cut diameters are obtained with a flow rate of 19 m^3/min through the sf-CASCC. Both stages use gravity and aerodynamic drag to draw the collected cloudwater down the strands or rods and into sample bottles. Unfortunately, the sampling efficiency curves for the large diameter Teflon rods are not very sharp, allowing some number of drops smaller than the 50% cut diameter to be

collected while allowing another percentage of drops larger than the 50% cut diameter to pass through to the second stage. This effect is compounded by the fact that 9% of the air passing through the first stage is never sampled by the Teflon rods, again allowing some drops larger than the 50% cut diameter to pass by. These factors combine to produce considerable overlap between the populations of drops sampled by each stage. In its favor, however, the sf-CASCC does gather large volumes of both drop fractions in short collection periods to allow extensive chemical analysis to be performed.

Conceptually simple devices used for the collection of supercooled cloud drops, called cloud sieves, are described by Hindman et al. (1992). The cloud sieves utilize a passive approach in which the ambient wind provides air flow over cylinders of various diameters to collect different size ranges of cloud drops. The concept behind this technique is similar to that used in the CASCC family of collectors. As air flows past a cylinder of a certain diameter, drops larger than a critical diameter will be collected while those smaller will not be. The larger the cylinder, the larger will be the critical diameter for the impaction of cloud drops for a fixed approach velocity. Here, cylinders ranging in diameter from 0.152 to 20 mm are employed. The 0.152 mm diameter cylinders are arranged in an interlocking woven mesh pattern and collect all drop sizes larger than 2 μm. The 20 mm diameter cylinders are arranged in a vertical series and collect all drop sizes larger than 23 μm. Similar arrangements of cylinders having diameters between these extremes possess 50% cut diameters of 3, 6, 7, 10, and 14 μm. These 50% cut diameters are valid for cloud sieve use at Storm Peak Lab (SPL) in Steamboat Springs, CO, where average wintertime conditions of –10° C, 700 mb, and 9.5 m/s wind speed are assumed. See Figure 1.4 for design and collection details for the range of cloud sieves. Because these cloud sieves are deployed in parallel, rather than in series as with a cascade inertial impactor, each sieve collects drops larger than its 50% cut diameter, requiring the use of subtraction techniques to obtain information regarding individual ranges of drop sizes. Another disadvantage to this approach is the reliance on the ambient wind to provide air flow past the sieves. Wind speed variations over

the collection period result in variations in the size of drops collected. A redesign of the sieves may be necessary if operation in ambient conditions other than those for which they were designed is desired.

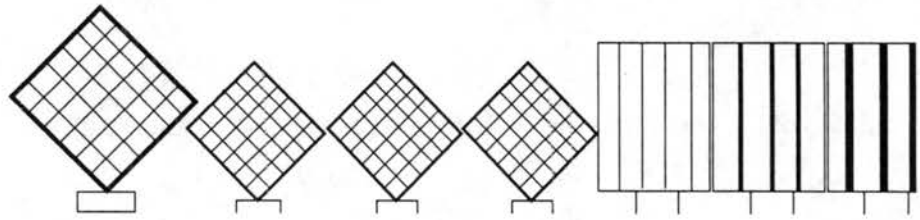

Cloud Sieve (CS)	#0	#1	#2	#3	#4	#5	#6
$d_{c\,(mm)}$	0.152	0.36	1.32	1.91	3.835	7.887	20
$d_{50\,(\mu m)}$	2	3	6	7	10	14	23
A (mm^2)	0.0244	0.01823	0.02427	0.01577	0.04096	0.1106	0.132
L (m)	160.528	50.65	18.383	8.28	10.681	14.021	6.6
Re	74	190	634	1,009	2,114	4,227	9,085
E.T. (min)	0.77	N/A	0.85	N/A	0.86	1.78	130
$M_{max\,(g)}$	2.42	4.13	20.1	19.1	98.9	550	1,669

Figure 1.4 Parameters describing cloud sieves for passively collecting cloudwater with 50% cut diameters from 2 to 23 μm (from Hindman et al., 1992).

The Counterflow Virtual Impactor (CVI) has been used by a number of researchers for ground based and airborne collection of cloudwater in various size ranges for the investigation of size-dependent chemical variations (Noone, 1987; Noone et al, 1988; Ogren et al., 1989; and others). A numerical analysis of CVI performance is provided by Laucks and Twohy (1998). The CVI consists of two concentric tubes as illustrated in Figure 1.5. The inner tube has a porous section through which a supply of dry, heated air (F_1) passes from the annular region between the tubes and into the inner tube. When the flow enters the inner tube, a portion (F_2) is directed toward the sampling instruments while the remainder (F_3) flows out of the CVI inlet. A stagnation plane develops at the location where these two flows diverge and the velocity of the air along the axis is zero. For drop collection, the CVI is placed in a free air stream which flows around the tip of the CVI. When drops traveling with the free air stream encounter the CVI, those

with insufficient inertia simply follow the streamlines of the free air stream around the inlet and are not collected. However, larger drops that possess enough inertia depart from the streamlines and enter the inlet. Once inside the CVI, drops again must have sufficient inertia to traverse the counter flow region and pass the stagnation plane if they are to be sampled. Those that do not have enough inertia reverse direction and are removed from the CVI by the counter flow (F_3). In this way, only drops that are large enough to possess sufficient inertia to pass the stagnation plane will be collected. With other factors held constant, the distance from the CVI inlet to the stagnation plane determines the required inertia, and therefore drop size, needed to pass through the entire inlet. The location of the stagnation plane can be changed by adjusting the flows F_1 and F_2, thereby allowing the 50% cut diameter of the instrument to be varied between 4 and 33 μm. Like the cloud sieves, the CVI can only sample populations of drops larger than the set 50% cut diameter and is therefore unable to collect multiple independent size fractions of cloud drops. In addition, when drops enter the heated and dried air flows in the CVI, evaporation may prevent a complete and accurate chemical analysis.

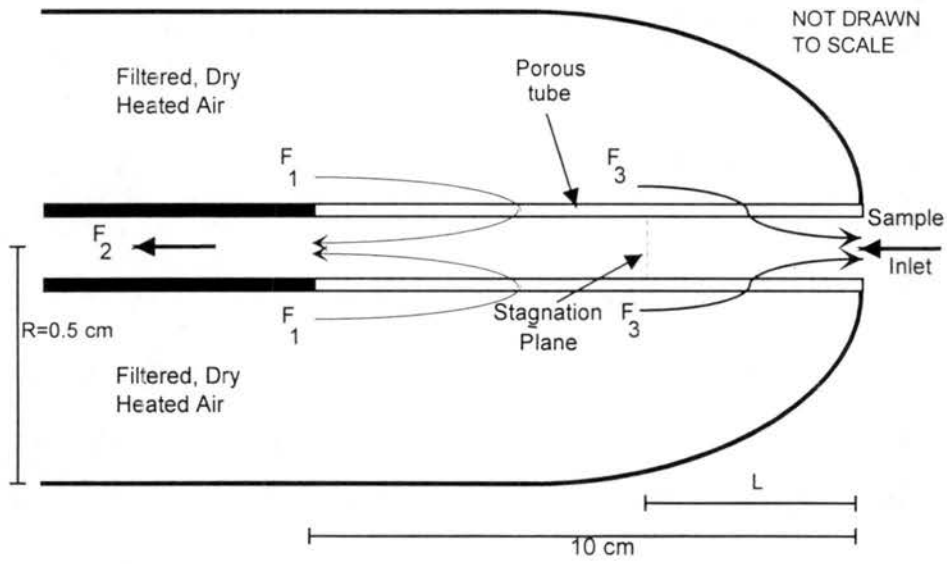

Figure 1.5 Cross-sectional view of the Counterflow Virtual Impactor (CVI). The 50% cut diameter can be varied by adjusting the location of the stagnation plane by controlling the flows F_1 and F_2 (from Iovinelli, 1994).

The Two-stage Fog Water Impactor (TFI) (Schell et al., 1997) has proven to be a useful instrument for the collection of cloud and fogwater in two independent size fractions. The TFI is an active cascade inertial impactor that uses a pump to draw air past collection surfaces. Air enters the TFI through an adjustable vertical rectangular inlet that accelerates the air and guides it toward a Teflon impaction plate. The largest fraction of drops in the air stream impacts on the collection plate while the air, along with the remaining smaller cloud drops, is deflected at right angles into two separate flows. These two flows are then further accelerated in parallel through additional vertical rectangular jets. As these jets impinge on the two second-stage impaction plates, the second fraction of cloud drops is gathered. At each of the impaction surfaces, the accumulated cloudwater is forced into channels located on the sides of the plates that direct the water to vials situated below the collector. For flow rates between 150 and 200 m^3/h, the 50% cut diameters for the TFI are between 10 and 12 μm for the first stage and between 5 and 6 μm for the second stages.

Two multi-stage inertial impactors that utilize round jets for the collection of multiple size fractions of cloudwater are the Eidgenössische Technische Hochschule (Swiss Federal Institute of Technology) (ETH) impactor (Collett et al., 1993, 1995) and the Institute for Environmental Studies Large (IESL) impactor (Iovinelli, 1994; Collett et al., 1995). The design of these devices was based on impactor guidelines presented by Marple and Willeke (1976) and Marple and Rubow (1986). The collectors are similar in appearance, with cylindrical shapes and Plexiglas construction, although the IESL is built on a much larger scale. The ETH impactor is composed of two stages arranged in series to collect two independent fractions of cloudwater. Air is drawn into the ETH impactor (Figure 1.6) through a circular inlet at a constant flow rate of 418 l/min. The air flow is directed through the first stage jet plate which consists of 15 round nozzles arranged in a ring. The nozzles accelerate the air toward a Teflon impaction surface where drops larger than 10 μm are removed from the air stream through inertial impaction. The air then enters the second stage through an opening in the center of the collection plate and is

directed through the 36 round nozzles in the second stage jet plate. The acceleration provided by the second stage nozzles allows drops larger than 3.5 μm to be collected on the second stage impaction surface. Shallow channels cut into the impaction surface contain the accumulated cloud drops until removal after a collection period. During a typical hour-long collection period, the ETH collector provides a large enough volume of cloudwater in these two size fractions to permit major ion and pH analysis. However, additional chemical measurements are generally not possible.

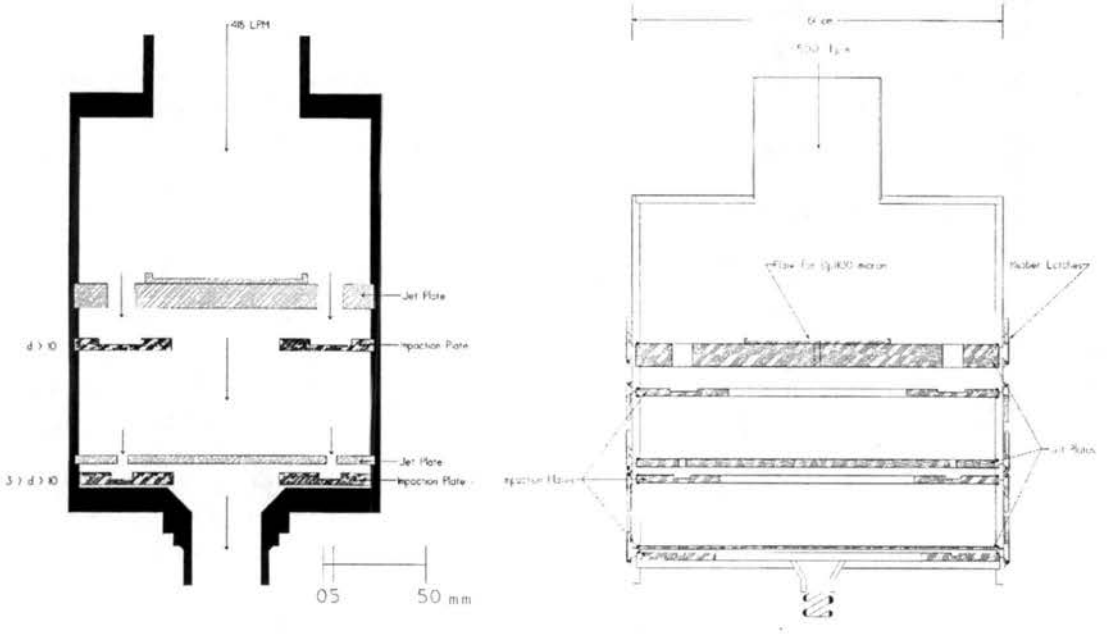

Figure 1.6 The ETH cloud impactor (left) collects two fractions of cloudwater with 50% cut diameters of 10 and 3.5 μm. The Institute for Environmental Studies Large (IESL) impactor collects three fractions of cloudwater with optional 50% cut diameters of 30, 20, 15, 12, 10, 4, and 3 μm (from Collett et al., 1993 and Iovinelli, 1994).

The desire to provide enough cloudwater sample volume in a short sampling period to allow extensive chemical analysis prompted the design and construction of the IESL collector (Figure 1.6). Similar to the ETH impactor, the IESL impactor uses multiple stages in series with round nozzles in each stage providing the progressive acceleration of the air stream. However, to obtain larger sample volumes, the IESL collector operates at a flow rate of 1500 l/min. To

accommodate this higher flow rate, the collector utilizes more nozzles per stage than the ETH impactor. To provide greater resolution of chemical variations with cloud drop size, a third stage was incorporated into the design of the IESL impactor. The three stages that form the collector can be selected from seven interchangeable jet plates with various 50% cut diameters. The final configuration of the IESL can then be adapted to match the ambient cloud drop size distribution if desired. The available jet plates have 50% cut diameters of 30, 20, 15, 12, 10, 4, and 3 μm. During field studies at Mt. Mitchell, North Carolina and La Jolla Peak, California involving the IESL impactor, sufficient cloudwater was collected on each of the stages to permit significant chemical analysis. Unfortunately, the large size (0.6 m diameter by 1 m height) and weight of the IESL impactor, which requires the use of a mobile cart for transport and an overhead crane for disassembly and sample removal, place some constraints on its use in the field.

An inertial cascade impactor developed by Berner et al. (1998) for the collection of haze and fog drops is similar in design to previous inertial cascade impactors manufactured by HAUKE, Inc. for the collection of aerosol particles. This collector, designated the LPI 80/0.5;32/2, consists of six stages that operate in series to collect independent fractions of fogwater. Like the ETH and IESL impactors, the LPI 80 impactor is cylindrical in shape and employs multiple round nozzles arranged in a ring in each stage to accelerate the air toward the impaction surfaces (see Figure 1.7). However, in this case, the outer shell and jet plates are constructed out of aluminum and the impaction surfaces are polypropylene. TEDLAR foils for ion chromatography or aluminum foils for measuring the mass of involatile species are used as substrates on each impaction surface during collection. The LPI 80 impactor is 100 mm in diameter and uses a vacuum pump to provide a flow rate of 80 l/min through the impactor. At this flow rate, the 50% cut diameters for the six stages are 16, 8, 4, 2, 1, and 0.5 μm. A circular disk inlet with a 9 mm diameter aperture prevents drops larger than 32 μm from entering the collector.

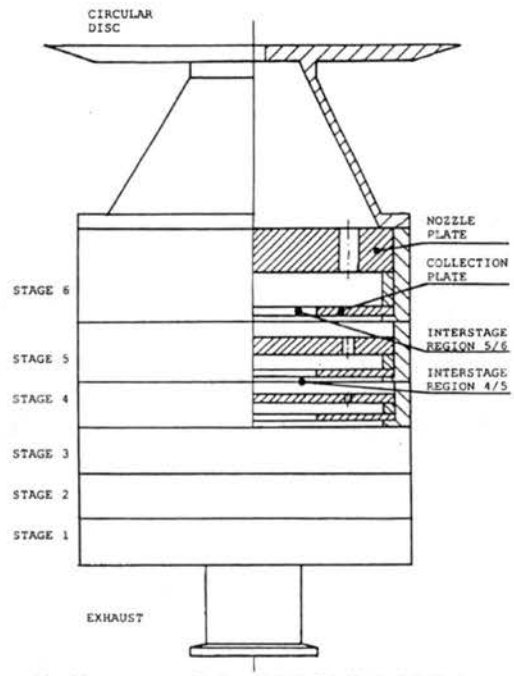

Figure 1.7 Schematic diagram of the LPI 80/0.5;32/2 impactor with 16, 8, 4, 2, 1, and 0.5 μm 50% cut diameters (from Berner et al., 1998).

A unique approach for collecting cloudwater in multiple size ranges has recently been developed at the University of Vienna (Laj et al., 1998). Rather than employing a single instrument with multiple stages in series to collect independent size fractions of water, five separate collectors are operated simultaneously to collect cloud drops in six diameter ranges. Each collector consists of two stages. The first stage removes all drops larger than a predetermined 50% cut diameter by inertial impaction, allowing the second stage to collect drops between the first stage cutoff and the second stage 50% cut diameter. The cloudwater collected on the first stage of each collector, except for the largest size fraction collector, is discarded. Only the cloudwater that accumulates on the second stages of the remaining collectors is used for analysis. The five collectors have first and second stage 50% cut diameters of 9 and 16 μm, 16 and 19.5 μm, 19.5 and 23 μm, 23 and 32μm, and 32 and 47 μm. The last collector provides a 32 to 47 μm size fraction as well as a fraction greater than 47 μm. In this way, six continuous independent size fractions can be collected with the five individual collectors. A collector flow rate of 280 m^3/h allows sampling periods of one to two hours. Use of this collection system in the

Po Valley in Italy revealed concentration and composition size dependencies in all sampled episodes.

Several other devices having the intended purpose of providing size-dependent collection of cloud or fog drops through inertial impaction are briefly mentioned in the literature. These include a collector featuring drop impaction on radially arranged cylindrical rods described by Vong et al. (1997), a collector for sampling drops between 2 and 8 μm on impaction cones (Millet et al., 1995), and a slotted rotating arm device that operates with arms of different lengths used by Schmitt (1987).

1.4 The FROSTY Supercooled Cloud Collector

As noted above, there are few cloudwater collectors designed specifically to sample supercooled cloud drops. The few that are available have significant limitations. Cloudwater collected by the CHRCC can provide only a bulk analysis, while complicated and possibly indefinite analysis techniques are necessary to obtain size-resolved information from cloud sieve samples. To fill the need for more effective supercooled cloud drop sampling necessary to better characterize the chemistry of wintertime clouds, the FROSTY supercooled cloud collector was designed and constructed at Colorado State University in 1996. The distinctive "snowman" shape of the collector when viewed from the top (see Figure 1.9) suggested the name "FROSTY". Its intended use for the collection of supercooled cloud drops in a wintertime environment made the choice of this name appropriate.

The FROSTY collector relies on cascade inertial impaction for the collection of three independent size fractions of supercooled cloud drops. This approach was selected to ensure that sufficient sample volumes could be obtained in short sample periods, while attaining sharp efficiency curves. Inertial impactor design principles presented by Marple (1970) and Marple and Rubow (1986) served as guidelines for the development of the FROSTY collector. The three stages were intended to have 50% cut diameters of 15, 10, and 4 μm. The FROSTY collector was

developed for conditions encountered during wintertime operation at an elevation of approximately 3000 meters. Figure 1.8 shows a picture of the FROSTY collector in operation at Storm Peak Lab (SPL) in Steamboat Springs, CO.

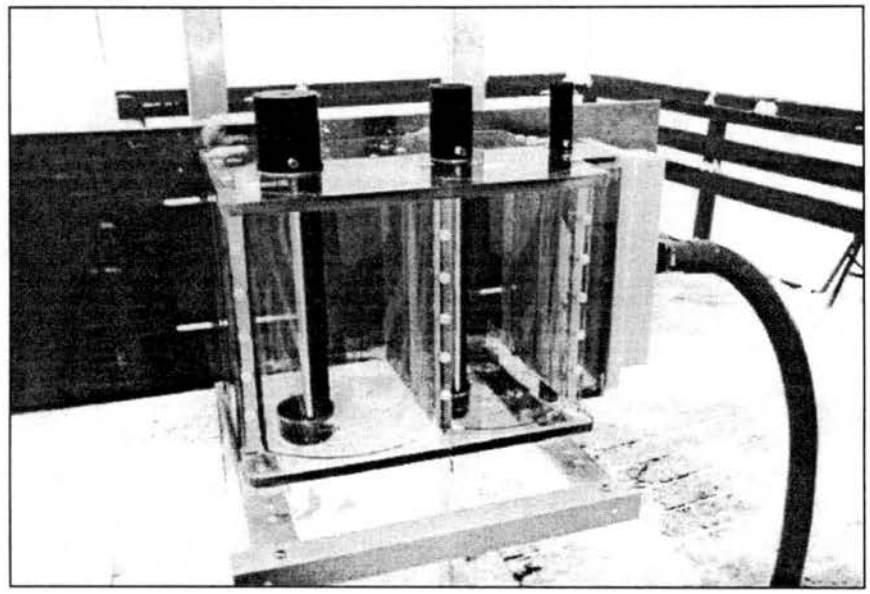

Figure 1.8 The FROSTY supercooled cloud collector in operation at SPL. Design 50% cut diameters are 15, 10, and 4 μm at a flow rate of 1500 l/min.

The FROSTY collector is an active cloudwater collector with a blower providing the necessary 1500 l/min flow rate. Air enters the collector through a rectangular jet, as illustrated in a top view of the collector in Figure 1.9. This jet accelerates the air towards the first stage collection surface where large cloud drops, which possess enough inertia, deviate from the streamlines and impact the surface. Because the drops are supercooled, they freeze immediately and adhere to the collection surface when contact is made. After the largest fraction of drops has been removed from the air stream, the air then enters the second and third stages in succession where the widths of the jets are progressively reduced. In this way, higher jet velocities are obtained and smaller cloud drops are collected in each of the remaining stages. The second stage collects a medium size fraction and the third stage collects the smallest size fraction of drops.

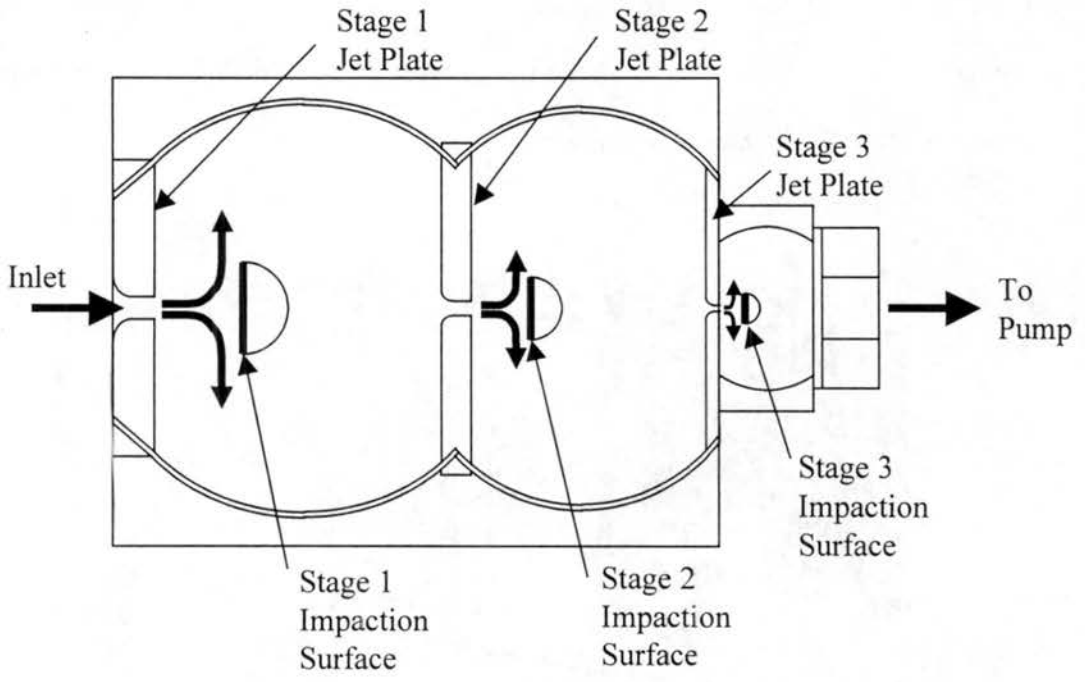

Figure 1.9 Schematic top view of the FROSTY supercooled cloud collector. Heavy black arrows indicate general air flow patterns.

The FROSTY collector is constructed entirely of plastic so that any trace metals present in the cloudwater can be detected without interference from metal collector components. The majority of the collector is fabricated from Plexiglas, including the jet plates and walls. The collection surfaces are Teflon, and the collection surface supports are Delrin. The FROSTY collector has dimensions of approximately 30 cm wide by 60 cm long by 30 cm high and weighs approximately 15 kg.

Collection periods are typically one hour in length, after which the collection surfaces are removed from the collector. The surfaces can then be taken into a heated area, where the accumulated frozen cloud drops can be melted, processed, and stored for later chemical analysis. A second set of collection surfaces can be inserted into the FROSTY collector as the first set is removed to allow uninterrupted sampling.

The FROSTY collector's high flow rate was chosen to maximize the quantity of air that can be processed through the collector and therefore maximize the amount of cloudwater that can

be collected. Relatively large volumes of sample are needed to perform a full range of chemical analysis, including pH measurement, major ion analysis by Ion Chromatography, trace metal analysis with a Graphite Furnace Atomic Absorption Spectrophotometer, peroxide and formaldehyde measurement by fluorescence spectrophotometery, and sulfur (IV) by UV/VIS spectrophotometery. Collection of large volumes of cloudwater in short time periods allows for adequate resolution of cloud or fog chemical changes in time. Another design goal for the FROSTY collector was to minimize its size in order to make transportation and field use more manageable. It was determined that the use of a single rectangular jet per stage rather than multiple circular jets would provide the minimum collector size. The desire for a high flow rate while maintaining a small collector size required a performance tradeoff, however. The high Reynolds numbers associated with higher flow rates through the jets results in additional overlap among the populations of drops collected on each of the stages (Marple and Rubow, 1986). However, it was hoped that this design would produce sharper size cuts than designs involving strand or rod collection surfaces, producing a satisfactory distinction between the populations of drops collected on the three stages.

The FROSTY collector has been used to collect supercooled cloud samples in field studies at Storm Peak Lab (Xu et al., 1999) and at Horsetooth Mountain, west of Fort Collins, CO. On both occasions, operation of the FROSTY collector was as expected. Supercooled cloud drops accumulated on all three impaction surfaces during the hour-long sampling periods. Chemical analysis of these samples revealed variations in composition among the populations of drops collected on the three stages.

1.5 The CSU 5-Stage Cloud Collector

The CSU 5-Stage cloud collector was designed and built to investigate size dependent chemical variations in clouds and fogs with higher resolution than has been possible with previous cloudwater collectors. The collector uses the cascade inertial impaction method for

cloudwater collection and has, as the name implies, five stages to collect five independent size fractions of cloud or fog water. The CSU 5-Stage collector was designed to gather drops larger than 30 μm in the largest size fraction, between 25 and 30 μm in the second size fraction, between 15 and 25 μm in the third size fraction, between 10 and 15 μm in the fourth size fraction, and between 4 and 10 μm in the smallest size fraction. The division of the ambient cloud drop population into these fractions is governed by the stage design 50% cut diameters of 30, 25, 15, 10, and 4 μm. These desired cut sizes were calculated based on operation of the collector at sea level. Unlike the FROSTY collector, the CSU 5-Stage collector has a collection and sample retrieval system that is designed to operate in warm clouds and fogs.

The five stages in the CSU 5-Stage collector are arranged in a "staircase" fashion as seen in a side view of the collector in Figure 1.10. The collector is approximately 25 cm by 50 cm by 80 cm and weighs approximately 30 kg. As with the FROSTY collector, this collector is fabricated entirely out of plastic to avoid trace metal contamination. The collector walls and collection surfaces are made out of Delrin. Each stage of the collector has a removable Plexiglas lid that allows access to the interior of the collector. A blower, attached to the last stage by a 3.8 cm diameter flexible hose, provides a flow rate of 2000 l/min through the collector. Cloud drop laden air enters the collector through the first stage inlet and is then deflected at a 90° angle by the first stage impaction surface. Here, the largest size fraction of drops which cannot follow the air flow streamlines past the first stage collection surface are collected. As the flow exits the first stage, the air is again forced to make a 90° turn and further accelerated as it enters the second stage. The second stage captures the second largest size fraction of cloud drops. The air flow continues in a similar fashion through the remaining three stages where progressively smaller fractions of cloudwater are collected.

During operation, the entire collector is positioned at a 45 degree angle relative to the ground by a specially designed stand. A picture of the collector and stand illustrating this arrangement can be seen in Figure 1.11. As the collected cloud drops coalesce into larger drops

on the collection surfaces, this orientation allows them to move downward under the influence of gravity and flow into collection vials located at the bottom of each stage. At the end of a collection period, typically one hour in length, any accumulated cloudwater that has failed to drain from the impaction surfaces is forced into the sample vials with the use of a clean rubber scraper. The vials are then removed from the collector, allowing the accumulated cloudwater to be processed and stored for subsequent chemical analysis.

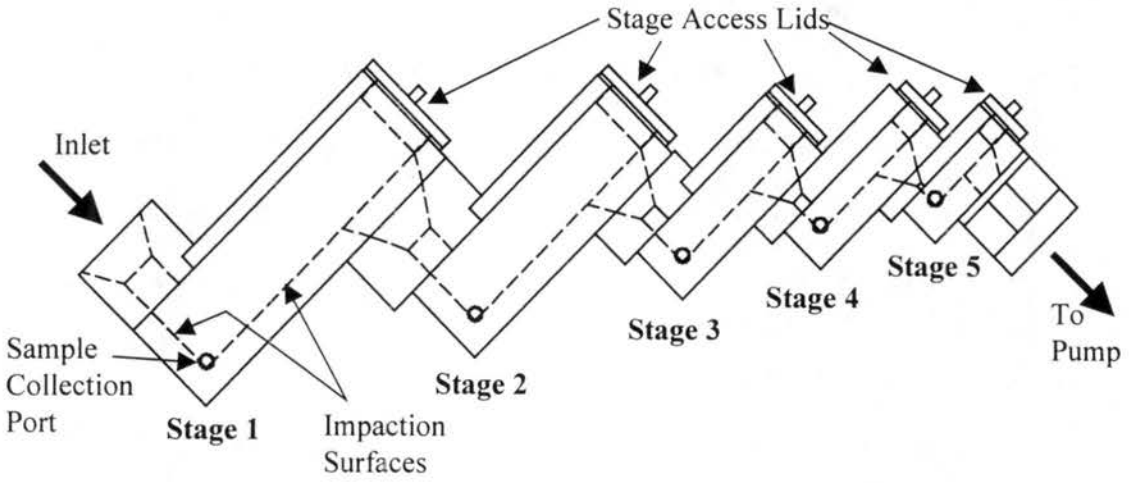

Figure 1.10 Schematic side view of the CSU 5-Stage cloud collector. Dashed lines indicate interior surfaces. 50% cut diameters are 30, 25, 15, 10, and 4 μm at a flow rate of 2000 l/min.

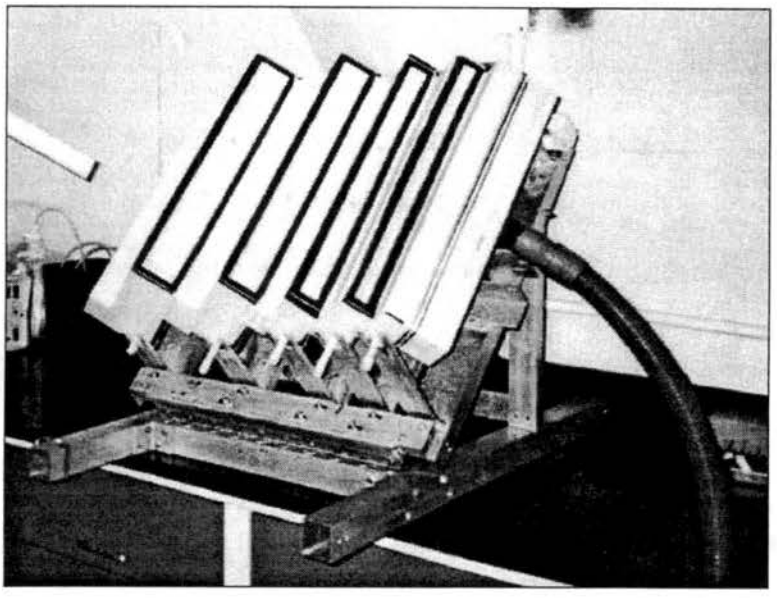

Figure 1.11 The CSU 5-Stage cloud collector and support stand oriented at a 45° angle to facilitate sample removal.

The choice of cascade inertial impaction, flow rate, and physical layout for the CSU 5-Stage collector was based on similar considerations as the FROSTY collector. These considerations include the need for large sample volumes, short collection periods, and a compact size.

Operation of the CSU 5-Stage collector during a number of field studies has provided some preliminary findings. The collector has been deployed in Davis, California, at Whiteface Mountain, New York, and for the Aerosol Characterization Experiment 2 (ACE2) in Tenerife, the Canary Islands for the purpose of collecting cloud and fogwater samples. During these field campaigns, volumes of cloudwater sufficient for chemical processing were collected on each of the five stages during various one-hour sampling periods. Subsequent chemical analysis revealed that chemical distinctions existed among the drop populations collected on the five stages.

1.6 Motivation and Objective

Many cascade inertial impactors have been designed, calibrated, and successfully operated for the purpose of collecting and characterizing aerosols. Many fewer instruments of this design have been constructed for the investigation of cloudwater chemical variations with drop size. Of those that have, fewer still have undergone a full calibration to completely describe their collection characteristics.

The design of the FROSTY and CSU 5-Stage collectors was based on established inertial impactor design guidelines developed by Marple (1970) and Marple and Rubow (1986). These guidelines, which suggest optimal impactor geometries for the collection of drops or particles in desired size ranges, have been used successfully in the past for the design of inertial cloud collectors (Collett et al., 1995; Schell et al., 1997). The use of proven design guidelines during the development of the FROSTY and CSU 5-Stage collectors provides some confidence that their actual operational collection characteristics would match the desired characteristics for which they were built. However, some aspects of collector design, such as the layout of the walls and

the geometry of the regions between stages, are not specified in these guidelines. Therefore, it was still necessary to perform calibration to definitively assess the overall performance of the collectors.

The characteristics that can be used to define collector performance include the 50% cut diameter for each stage, as well as the shape of the stage efficiency curves. These values can provide quantitative information about the populations of cloud or fog drops that will be collected on each of the stages during field operations. This information is necessary if accurate conclusions regarding the nature of chemical variations with drop size are to be made using data from the FROSTY or CSU 5-Stage collectors. Also of interest are the air flow patterns through the collector and the extent of cloud drop losses to the interior walls. These details can further define the performance of the FROSTY and CSU 5-Stage collectors and may also suggest alternatives for improved operation. Finally, it was desired to develop a design tool that could be used to reliably evaluate future cloudwater collectors during the design phase before committing considerable resources to build and evaluate them. A tool of this type could provide a savings of both time and money while permitting the development of improved collectors.

The objective of this work, therefore, is to examine the collection characteristics of the FROSTY and CSU 5-Stage collectors in actual operation. This was accomplished in two phases. A numerical analysis of the air flow patterns and cloud drop trajectories through the collectors was performed, followed by an experimental calibration of each collector. The results from the numerical modeling were compared to the experimental calibration data to assess the ability of numerical modeling to simulate the behavior of air and cloud drop flows through cloudwater collectors. The practicality of applying numerical modeling as a design tool was also examined.

2 Numerical Modeling Approach

2.1 General description of Computational Fluid Dynamics

Computational Fluid Dynamics (CFD) is a numerical technique used for the analysis of fluid flow phenomena. The application of numerical methods to fluid flow problems has lagged similar techniques for solid modeling, but it is a rapidly developing field that can offer insight into the behavior of fluid flows in a wide range of applications. The analysis procedure generally begins with the use of a modeling program to generate the flow domain geometry being considered. A meshing procedure divides the flow domain into small elements to allow a numerical solution to be obtained. Boundary and initial conditions and fluid properties specific to the individual problem are then defined. Based on these inputs, a solver provides a solution to the flow problem in terms of velocity fields, pressure fields, mass fluxes, turbulent properties, heat transfer, and other quantities that may be of interest.

There are numerous citations in the literature referring to the successful application of numerical modeling to the analysis of flow fields and particle motion. Examples include the analysis of particle deposition in pipes (Muyshondt et al., 1996; McFarland et al., 1997; Chen and Ahmadi, 1997), cyclone separators (Griffiths and Boysan, 1996), counterflow virtual impactors (Asgharian and Godo, 1997; Laucks and Twohy, 1998), and standard aerosol impactors (Marple and Liu, 1974; Radar and Marple, 1985; Jurcik and Wang, 1995; Swanson et al., 1996, and Asgharian et al, 1997).

The conservation of mass and momentum provide the basis for the equations governing fluid flow in CFD. The governing equations consist of three momentum conservation equations

(the Navier Stokes Equations) when working in three dimensions, and the mass conservation equation or continuity equation. Because these equations are a system of nonlinear, second order, partial differential equations, an analytical solution is not possible. Instead, to obtain a solution, the flow domain is discretized into a large number of subdomains through the use of a grid. The governing equations can then be applied to each subdomain, resulting in a set of simultaneous algebraic equations that can be solved numerically.

A main factor distinguishing CFD codes is the method used to approximate the differential equations when they are applied to each discrete subdomain. Approaches that are commonly used in commercial CFD codes are finite element, finite difference, and finite volume methods. Finite difference methods apply an approximation of the differential form of the governing equations to each node point as defined by the grid. The finite volume method uses approximations of the integral form of the governing equations that are applied to the center of each control volume that is defined by the grid. Finite element methods are similar to finite volume methods, except that a weighting function is applied to the governing equations before they are integrated over the control volumes. When the flow domain has been discretized into fine enough elements, these approaches will all provide an identical solution (Ferziger and Peric, 1996).

CFD codes also use various approaches to arrive at a solution to the system of transformed governing equations, for simulation of the effects of turbulence, for the discretization of the flow domain, and for the analysis of multiphase flows. Details regarding the approaches used in the CFD software selected for this work will be discussed in the following sections. In addition to the solution of fluid flow, many CFD codes also offer the capability to simulate heat transfer and chemical reactions within the flow domain. However, these features were not activated for the numerical analysis of the FROSTY and CSU 5-Stage collectors, so a description of their attributes will not be included here.

2.2 Selection of CFD software

The desire to apply CFD to the analysis of flow patterns and drop trajectories through the FROSTY and CSU 5-Stage cloudwater collectors required a decision regarding the type of CFD software that should be used. Development of a new CFD code from the ground up, or even the modification of an existing prototype code, would have taken considerably more time and resources than were available for the project. Fortunately, numerous high quality CFD codes are available commercially; many offering substantial discounts from their regular licensing fees for educational research related work. Although fluid flow analysis is the overall goal of each code, they vary in solution method, physical models provided, and special features. Unfortunately, direct comparison of the merits of individual codes is difficult, although Freitas (1995) does provide some quantitative comparative testing among a handful of codes.

Of the many codes available, several were examined in greater detail for possible purchase. These included FLUENT and FIDAP (Fluent, Inc., Lebanon, NH), STAR-CD (Computational Dynamics Ltd., London), and CFD-ACE (CFD Research Corporation, Huntsville, AL). Papers in which these codes were utilized for fluid flow analysis were reviewed and, when possible, researchers familiar with the codes were consulted to obtain advice and opinions about the codes' accuracy, ease of use, and applicability to this work.

After much deliberation, FLUENT version 4.48 (Fluent, 1996) was ultimately chosen for the numerical modeling portion of this work. A number of factors combined to make FLUENT the most attractive CFD code. First of all, FLUENT possessed the features and physical models that were needed to complete an analysis of air flow and drop trajectories through the collectors. FLUENT offered multiple options for modeling multiphase flows and for addressing turbulence in the flow field, providing more flexibility than other codes. Validation of FLUENT's capabilities for the modeling of impactor flow fields by Swansen et al. (1996) and flow field and trajectory analysis by Griffiths and Boyson (1996) was taken into account. In addition, researchers in the Civil Engineering Department at Colorado State University were already using

the FLUENT software for fluid flow analysis and had considerable experience with it. Guidance in the use of the software was therefore available if ever needed. These researchers also advocated the abundant technical support that FLUENT, Inc. provided to holders of educational licenses.

Use of the FLUENT software was made relatively easy by the voluminous documentation that accompanied the code. Helpful tutorial guides and sample problems provided sufficient instruction that basic implementation of the code was possible in a matter of weeks. An in depth understanding of the physics underlying the software took considerably longer, however.

Software for geometry construction, grid generation, problem setup, and the FLUENT solver were all run on a 200 MHz Pentium Pro PC with 64 MB of RAM running the Windows NT 4.0 operating system.

2.3 Continuous phase modeling in FLUENT

Following FLUENT's terminology, the term "continuous phase" will be used to refer to the air flow through the collector and the term "dispersed phase" will refer to cloud drops. FLUENT uses a finite volume approach to obtain a solution to the governing conservation equations of fluid motion. The mass and momentum conservation equations in the ith direction used by FLUENT are, respectively:

$$\frac{\partial \rho}{\partial t} + \frac{\partial}{\partial x_i}\left(\rho u_i\right) = S_m \tag{2.1}$$

$$\frac{\partial}{\partial t}\left(\rho u_i\right) + \frac{\partial}{\partial x_j}\left(\rho u_i u_j\right) = -\frac{\partial p}{\partial x_i} + \frac{\partial \tau_{ij}}{\partial x_j} + \rho g_i + F_i \tag{2.2}$$

where ρ is the fluid density, p is the static pressure, u_i is the fluid velocity in the ith direction, S_m is a mass source or sink, g_i is gravitational acceleration in the ith direction, and F_i refers to external body forces in the ith direction. τ_{ij} is the stress tensor which defines normal and shear stresses in the fluid in terms of fluid velocity gradients, and is given by:

$$\tau_{ij} = \left[\mu \left(\frac{\partial u_i}{\partial x_j} + \frac{\partial u_j}{\partial x_i} \right) \right] - \frac{2}{3} \mu \frac{\partial u_l}{\partial x_l} \delta_{ij} \qquad (2.3)$$

where μ is dynamic viscosity and the second term on the right hand side describes the effect of volume dilation. The volume dilation term is equal to zero for incompressible flows and is therefore not applicable in this modeling work.

To convert equations 2.1 and 2.2 to algebraic equivalents that can be solved numerically, they are integrated over the volume of each element, with the use of the divergence theorem to reduce the volume integrals to surface integrals. For an illustrative example of this transformation for a simple one-dimensional, steady state case, see Appendix A. This process results in equations in algebraic form with unknowns in terms of neighboring cell center and cell face values. The mass and momentum conservation equations in this form apply to each of the discrete control volumes that define the flow domain. A solution to the resulting system of simultaneous algebraic equations can then be obtained, as will be described in the following sections. A schematic illustration describing the procedure used by FLUENT to obtain a continuous phase solution is provided in Appendix D.

2.3.1 Iterative finite volume approach

When solving a three-dimensional problem, each control volume will have three momentum equations, the continuity equation, and up to six equations describing turbulence quantities associated with it. This set of ten coupled equations and ten unknowns for each control volume would, in the case of a large domain, three-dimensional turbulent problem, result in a system of tens of thousands or hundreds of thousands of equations. A simultaneous solution of a system of this type is computationally intensive, and may not be practical. To avoid this problem, FLUENT uses an iterative procedure to converge on a solution to the set of algebraic equations that are produced when the conservation equations are integrated over each control volume in the flow domain.

In this process, the solutions to the momentum, continuity, and turbulent transport equations are obtained sequentially, in an iterative manner, rather than simultaneously. For this sequential procedure, FLUENT uses the Semi-Implicit Method for Pressure Linked Equations (SIMPLE) (Patankar, 1980; Ferziger, 1996; Fluent, 1996), which begins with a "guessed" pressure field throughout the solution domain. The "guessed" pressure field is substituted into the momentum equations, leaving only velocities as unknowns. This allows the momentum equations to be solved for a "guessed" velocity field. Because this solution of the momentum equations is based on a "guessed" pressure field, the velocities that are calculated will not necessarily satisfy the continuity equation. A correction to the "guessed" pressure field therefore needs to be made. This is accomplished by transforming the continuity equation into a pressure correction equation.

The "guessed" velocities are then simply substituted into the newly derived pressure correction equation to generate a pressure correction term. The pressure correction term is then used to update, or correct, the "guessed" pressure and "guessed" velocities in each cell. Finally, using the updated pressure and velocities, the equations describing turbulence quantities are solved. This process constitutes one iteration. To begin the second iteration, the updated pressure field is once again substituted into the momentum equations to solve for a new velocity field, and the process is repeated until global convergence criteria (normalized residuals less than $1x10^{-3}$) are met.

When the momentum or pressure correction equations are solved in the sequential solution procedure described above, the equations are not solved simultaneously over the entire solution domain. Again, a solution over the entire domain would require extensive computational resources. Instead, each row of control volumes in the computational domain is treated separately and a solution to the equations is obtained one row at a time. The solution of the equation set for one row of cells is dependent on values of unknowns from neighboring rows, so during the solution for one row, neighboring row values from a previous iteration are used. A solution for

the entire domain, called a sweep, is obtained row by row. This technique, which uses Gaussian elimination to solve systems of simultaneous equations, is known as Line Gauss-Seidel. The direction in which the rows of control volumes are progressively solved as well as the number of sweeps performed per iteration can be controlled in order to improve the convergence of the solution. For this modeling work, the default parameters, which specify two sweeps in alternating directions per iteration, worked well and were therefore left unchanged. However, for complex problems in which convergence is difficult, these parameters can be manipulated to try to encourage the development of a solution.

2.3.2 Interpolation from cell center values

Values for pressure, velocities, and turbulence quantities are stored in the center of each control volume. However, because of the transformation of the Navier Stokes equations from partial differential equations to algebraic equations, variable values at the cell walls become necessary. These wall values must be interpolated from cell center values. FLUENT provides three interpolation schemes for this purpose. There is a Power Law Differencing Scheme, as well as two higher order schemes, a blended Second Order Upwind / Central Difference Scheme, and a Quadratic Upstream Interpolation for Convective Kinematics (QUICK) scheme (Leonard, 1979).

The Power Law Scheme (Fluent, 1996) assigns cell face values equal to those of the upstream cell center values if strong convection is present. If the flow is diffusion dominated, the assigned cell wall value is a simple linear interpolation between the upstream and downstream cell center values. Finally, for cases in which convection and diffusion are both present, a power law is used to develop a value between these two extremes. The Power Law Scheme offers stability during the solution process, but is subject to numerical or false diffusion in areas where the flow is not aligned with the grid and strong gradients exist.

The two higher order schemes both include additional upstream cell center values and a downstream cell center value to provide a more accurate description of the variation of pressures and velocities between the stored cell center values. Although computational time is increased, interpolation of values from cell centers to cell walls using the higher order schemes provides additional accuracy, and is also less susceptible to the problems of numerical diffusion (Freitas, 1995; Ferziger, 1996).

For the modeling of FROSTY and the CSU 5-Stage collectors, the flow exhibits strong velocity gradients with flow at an angle with respect to the grid in several locations, especially as the flow is being turned by the impaction surfaces. To prevent inaccuracies due to numerical diffusion in these areas, a higher order interpolation scheme was chosen. Although the QUICK and Second Order Upwind Scheme offer nearly equivalent results, the QUICK scheme was used because it offers slightly higher accuracy (Fluent, 1996) and it provided a stable solution.

A brief investigation into the effects of the different interpolation schemes was performed with the FROSTY collector model. Two flow field solutions were generated in which only the interpolation scheme was changed. All other geometry, boundary conditions, and model options were identical. During the solution process of these two test cases, it was noted that the power law scheme was more stable and provided a converged solution faster and with fewer iterations than the QUICK scheme, although this solution speed comes with some possible error as described above. This error may be evident in Figures 2.1 and 2.2, in which there is a pronounced difference in the flow field in the third stage of the FROSTY collector between the two interpolation schemes. In the region upstream of the third stage impaction surface, there is a much stronger rotational component in the velocity field when QUICK interpolation is used. This stronger recirculation upstream of the impaction surface induces a higher velocity in the jet itself. Additionally, the highest velocity region of the jet is closer to the impaction surface when the QUICK scheme is used. Also apparent is a more pronounced rotation in the interstage region behind the impaction surface.

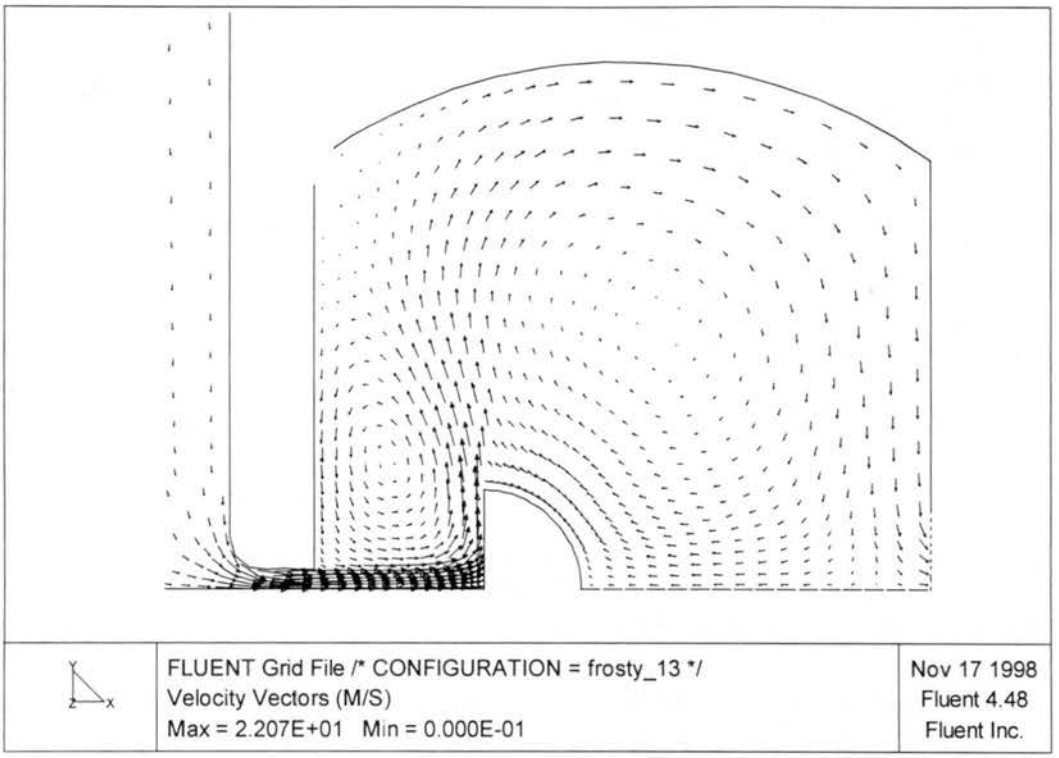

Figure 2.1 Velocity vector field in the third stage of the FROSTY collector with Power Law interpolation used in the numerical analysis.

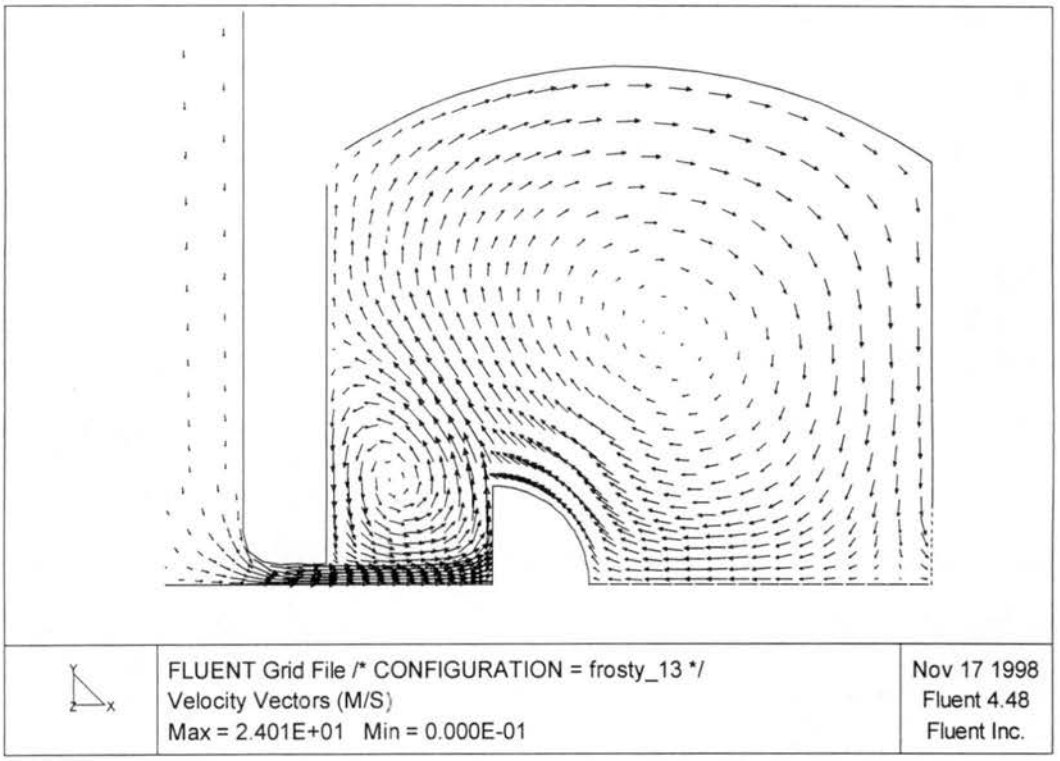

Figure 2.2 Velocity vector field in the third stage of the FROSTY collector with QUICK interpolation used in the numerical analysis.

2.3.3 Turbulence options

Turbulence is accounted for in the numerical modeling through Reynolds averaging of the governing equations (Fluent, 1996). In this process, the velocity terms in these equations are assumed to consist of an average component, denoted by an overbar, and a time varying component, denoted by a prime:

$$u_i = \overline{u_i} + u_i' \tag{2.4}$$

When these two components are substituted into the momentum equations (equation 2.2) in place of the total velocity, the following form of the momentum equation can be derived (after dropping the overbar for average velocities):

$$\frac{\partial}{\partial t}(\rho u_i) + \frac{\partial}{\partial x_j}(\rho u_i u_j) = -\frac{\partial p}{\partial x_i} + \frac{\partial \tau_{ij}}{\partial x_j} + \rho g_i + F_i + \frac{\partial}{\partial x_i}\left(-\rho \overline{u_i' u_j'}\right) \tag{2.5}$$

Equation 2.5 is identical to the original version of the momentum equation except for the last term on the right hand side of the equation. In this term, the expressions $-\rho\overline{u_i'u_j'}$ are referred to as Reynolds stress terms.

The purpose of a turbulence model, then, is to provide values for these Reynolds stress terms so that a solution to the governing equations is possible. FLUENT provides three turbulence models for the purpose of closing the turbulent equation set. They are the standard k-ε model, the Renormalized Group (RNG) k-ε model, and the Reynolds Stress Model (RSM).

For the modeling of the FROSTY and CSU 5-Stage collectors, the RSM, which solves transport equations for the individual Reynolds stresses, was used. It was selected in preference to the two equation k-ε and RNG models because it provides a more rigorous treatment of the turbulent velocity fluctuations in the complex flow through the collectors (Launder, 1989).

The default RSM coefficients are used for the modeling of the FROSTY and CSU 5-Stage collectors. The magnitude of turbulent velocity fluctuations, or turbulent intensity, is a required inlet boundary condition. For this work, the inlet turbulent intensity was set to a value of

3% of the mean velocity, although variations in this value did not have a large effect on the continuous phase solution. Similar results have been noted by others (Muyshondt et al., 1996). In their analysis of aerosol deposition in contraction fittings using FIDAP software, they found that increasing or decreasing the inlet turbulent intensity by a factor of two had no significant influence on the particle losses in the contraction fittings under investigation.

2.3.4 Wall treatment

To avoid the excessively fine mesh needed to resolve the flow features in the viscous sublayer adjacent to the collector walls, a wall function or "law of the wall" is used. The wall function determines the flow properties, including the mean velocity and turbulent quantities, in cells near the wall without explicitly solving the viscous effects that are present close to the wall. It does this by means of semi-empirical formulas as described by Launder and Spalding (1974). This approach to near wall modeling has produced satisfactory results for others investigating multiphase flow behavior including Griffiths and Boysan (1996), Gong et al. (1993), and Abuzeid et al. (1991).

FLUENT provides a non-equilibrium wall function (Fluent, 1996) in addition to the standard wall function. For this application, the non-equilibrium wall function, which extends the applicability of the standard wall function by including pressure gradient effects, was used. This modification of the wall function allows better accounting of deviations from equilibrium that are expected for impinging flow and recirculation features, both of which are present in the FROSTY and CSU 5-Stage collectors.

2.3.5 Mesh generation

To reduce computational effort, representative two-dimensional sections of the FROSTY and CSU 5-Stage collectors were selected for modeling. Although three-dimensional effects are neglected, a two dimensional representation was considered reasonable for initial modeling efforts. One of the main limitations of using a two-dimensional model for the analysis of flow

through these collectors may be that jet end effects are neglected. Both collectors use rectangular jets for the acceleration of air and cloud drops toward their respective impaction surfaces. The air flow and drop trajectories along most of the length of these jets should be fairly uniform, allowing the flow patterns to be captured by a two dimensional model domain that is normal to the jets. However, at the jet's termination points, the flow patterns may be quite different. Unfortunately, the end effects will not be captured by a two dimensional model. It was expected that the end effects would have a minimal impact on cloud drop collection when compared to the main flow through the jets.

Geometry construction for both collectors was accomplished with the preprocessing software Geomesh, provided by Fluent, Inc. Dimensional inputs for the collector geometries were taken from design sheets when possible or measured directly from the collectors when other information was unavailable. The Geomesh software was also utilized to generate the meshes for discretization of the flow domains. A structured mesh was used for both collectors. Refinement studies were performed on the structured meshes in which the grid density was increased by a factor of 1.5. Flow solutions based on both of the grid spacings were generated in FLUENT in order to determine if a grid independent solution had been obtained. For both collectors, solutions performed using the higher resolution grid spacing matched those using the lower resolution grid spacing, indicating that grid independence had been achieved. All subsequent modeling was performed with the lower resolution meshes.

2.3.6 Boundary conditions and fluid properties

Boundary conditions for inlets and walls were required to properly constrain the numerical model. At the collector inlets, the velocity was generally specified. The inlet velocities were calculated to correspond to the design volumetric flow rates of 1500 l/min through the FROSTY collector and 2000 l/min through the CSU 5-Stage collector. The walls were assigned a no slip boundary condition that sets fluid velocities at the wall surfaces to zero.

Because the collectors are immersed in the ambient environment during sampling, the collectors should be at the same temperature as air being drawn through them. For this reason, no heat transfer between the air stream and the collector walls or collection surfaces was considered in this work. For turbulence considerations, the walls and collection surfaces were assumed to be smooth and therefore given a surface roughness height of zero, the suggested value for plastic (Munson, 1990).

As described in sections 1.4 and 1.5, the FROSTY collector was designed for operation in wintertime conditions at approximately 3000 meters elevation while the CSU 5-Stage collector was designed to operate at sea level for the sampling of warm clouds. The desired size cuts for the collectors assume ground-based operation in those conditions. However, the experimental calibrations of the collector were performed in a laboratory setting at 1500 meters elevation. Thus, the air properties for the experimental work differed somewhat from the air properties experienced at design conditions. In addition, oleic acid drops, which have a density slightly lower than water, were used in place of liquid water drops in the experimental calibration work. Both of these differences tend to shift the experimental 50% cut diameters to sizes other than the design values. In order to provide numerical modeling data that could be compared to the experimental calibrations performed under laboratory conditions at 1500 m elevation and 21° C, the air and drop properties for the numerical modeling were chosen to match those at the laboratory conditions. These continuous phase properties specified in the model included a density of 1.01 kg/m^3 and a dynamic viscosity of 1.83×10^{-5} Ns/m^2. Supplemental numerical modeling was performed using air and drop properties at design conditions. This allowed a comparison of collection behavior at laboratory and design conditions.

Maximum air velocities in both of the collectors are on the order of 24 m/s, or a Mach number of 0.07. This is well below the Mach number of 0.3 at which compressibility effects becomes significant (Munson, 1990). Therefore, the air flow through the collectors was modeled as an incompressible fluid. Finally, the continuous phase flows through the FROSTY and CSU

5-Stage collectors were modeled as steady state solutions, so transient flow features were not resolved.

2.4 Dispersed phase modeling in FLUENT

Simulations of cloud drop trajectories through the FROSTY and CSU 5-Stage collectors were also generated using the FLUENT software. FLUENT provides three methods for the analysis of multiphase flows. These methods are the Volume-of-Fluid (VOF) multiphase model, the Eulerian multiphase model, and the Lagrangian multiphase model. Use of the Volume-of-Fluid multiphase model is intended for the analysis of liquid-gas interfaces, such as the study of large bubble behavior in liquids, or the motion of water after a dam break. This multiphase model was therefore not considered applicable to the gas-droplet two-phase flow encountered in a cloudwater collector. The Eulerian and Lagrangian multiphase models, on the other hand, can be used for the analysis of this type of flow. The Eulerian method treats both the gas phase and particle phase as coincident continuums and solves conservation equations as described in the previous section simultaneously for both. The conservation equations are modified in the Eulerian method to include the volume fractions of the dispersed and continuous phases. The Lagrangian multiphase method, in contrast, solves the conservation equations only for the continuous phase. The dispersed phase particles are then introduced and tracked individually as forces induced by the continuous phase act on them.

A discussion of the relative merits of the Eulerian and Lagrangian methods is provided by Durst et al. (1984). Briefly, the Eulerian approach is recommended for use when a high dispersed phase volumetric loading is present, such as a suspension flow or fluidized bed. One major disadvantage of using the Eulerian model is that only one size of dispersed phase drops can be simulated at a time. For every drop size of interest, the entire set of conservation equations for both phases requires a solution. This is a very time consuming proposition when the size dependent collection behaviors of the FROSTY and CSU 5-Stage collectors are required. The

advantage of the Lagrangian approach is that it provides more detail about individual particle trajectories, including a summary of particle interaction with walls, and only requires a single solution of the continuous phase governing equations. Because the typical droplet volume fraction in a cloud is quite low (e.g. 1×10^{-7} m^3_{H2O}/m^3_{air} to 5×10^{-7} m^3_{H2O}/m^3_{air} for cloud liquid water contents between 0.1 g/m^3 and 0.5 g/m^3), and because the collection patterns of multiple sizes of cloud drops was of interest, the Lagrangian method was the multiphase model best suited for the simulation of cloud drop motion through the collectors.

2.4.1 Lagrangian approach

The dispersed phase modeling was therefore performed in a Lagrangian frame of reference in which individual particles are tracked as they move through the fluid. The trajectories are calculated by performing a force balance on each particle as it moves through, and is influenced by, the continuous phase. The general procedure followed when performing a dispersed phase analysis is first to obtain the continuous phase flow field solution and then to introduce drops from desired locations into the continuous phase solution domain. The equation that describes the motion of a drop in the x-direction that is subject to various forces is:

$$\frac{du_p}{dt} = F_D(u-u_p) + \frac{g_x(\rho_p-\rho)}{\rho_p} + F_x \tag{2.6}$$

where u is the continuous phase velocity, u_p is the dispersed phase velocity, ρ is the continuous phase density, ρ_p is the dispersed phase density, F_X represents additional forces, such as the thermophoretic force, that can be considered, and F_D is the drag force coefficient described by the following expression:

$$F_D = \frac{18\mu}{\rho_p D_p^2}\frac{C_D\,\mathrm{Re}}{24} \tag{2.7}$$

where Re is the drop Reynolds number and C_D is the drag coefficient given by:

$$\mathrm{Re} = \frac{\rho D_p \left| u_p - u \right|}{\mu} \tag{2.8}$$

$$C_D = a_1 + \frac{a_2}{\mathrm{Re}} + \frac{a_3}{\mathrm{Re}^2} \tag{2.9}$$

The constants a_1, a_2 and a_3 in the drag coefficient relation are provided by Morsi and Alexander (1972) and are dependent on the flow regime being considered.

To calculate the path that a drop follows as it travels through the continuous phase solution, the drop equations of motion are integrated at numerous locations. The number of locations at which the equations are solved in each control volume is determined by the step length factor in FLUENT. For this work, the step length factor was set to 10 so that the equations of motion were solved at approximately ten locations in each control volume as the drop transited the continuous phase domain. This factor provided a balance of adequate resolution of the trajectories without excessive computational effort. When the effects of turbulence on drop motion are considered, as will be described in section 2.4.3, however, the time step factor may be overridden by another parameter that ensures sufficient resolution of drop motion due to short time scale turbulent fluctuations.

If a drop failed to contact a wall or exit the domain through the outlet after a specified maximum number of time steps, the trajectory calculation was terminated. This safeguard was used to avoid an infinite trajectory calculation should a drop become trapped in a recirculation loop. The maximum number of steps was generally set between 15,000 and 30,0000, which provided minimal trajectory terminations.

Finally, FLUENT provides an option that allows the continuous phase velocities used in equation 2.6 to be interpolated from the control volume center value to the drop position though a Taylor series expansion. The alternative is to simply use the cell center velocity in the equation of motion at any location within the cell. The option for velocity interpolation was activated to

provide more accurate trajectory calculations, although it was at the expense of longer processing time.

2.4.2 Assumptions and simplifications

For the CSU 5-Stage collector modeling, only the influence of the drag and gravity forces was considered in the drop equation of motion. For the FROSTY collector the drag force was included, however, the gravity force was normal to the plane of the two-dimensional model and was therefore not considered. Other forces that result from the motion of a particle in a fluid (e.g. Basset, virtual mass, and Magnus forces) can be considered negligible for dilute multiphase flows in which particle densities are much greater than continuous phase densities (Shirolkar et al., 1996), such as the type of flows encountered in a cloudwater collector.

A number of other assumptions and simplifications were included in the treatment of the dispersed phase in the numerical simulations performed in this work. The expression for the drag force, as described above, does not include the Cunningham slip correction factor, thereby ignoring non-continuum effects. However, at standard temperature and pressure, non-continuum effects only become important for sub-micron particles, while drops in the range of 4 to 60 μm were analyzed in this work. This diameter range also allowed the effects of Brownian motion to be neglected. It has been noted (Abuzeid et al., 1991; Li and Ahmadi, 1992) that the effects of turbulent fluctuations on particle motion overwhelms the effects of Brownian motion for particles greater than one micron.

Interactions between drops, such as collision and coalescence, are not accounted for in the FLUENT model. This treatment was considered acceptable because of the low volumetric water loading found in a typical cloud or fog. However, the focusing of the cloud drop stream into very narrow regions as the flow is accelerated through the jets of each collector, as will be illustrated in chapters 4 and 5, could result in more significant interaction between drops and may require further study. In addition, mass transfer between the dispersed and continuos phases due

to evaporation or condensation of the cloud drops during their transit through the collectors was also not included in the model. A detailed theoretical study investigating the effects of evaporation and condensation in a multistage fog water collector by Berner et al. (1998) provided support for this assumption. In the study, changes in water vapor saturation due to temperature and pressure changes caused by flow patterns in the orifice, stagnation, and interstage regions of the collector were calculated. The effects of the water vapor saturation variations on drop growth was then estimated. The study revealed that for stages with jet velocities and 50% cut diameters equivalent to those in the FROSTY and CSU 5-Stage collectors, changes in drop size were primarily due to evaporation in the interstage region. However, these changes can be considered minimal. At high ambient temperatures the calculated decreases in diameter ranged from 0.6% for 32 μm drops to 7.5% for 4 μm drops. Smaller evaporative losses were calculated for more typical ambient sampling conditions.

In agreement with assumptions that have previously been discussed, phoretic effects were also neglected. During the continuous phase modeling the assumption that the collector and the air being sampled were at the same temperature resulted in heat transfer being neglected. In the absence of large temperature gradients within the collector, thermophoresis could be neglected (Seinfeld and Pandis, 1998). Also, because mass transfer between phases was neglected, gradients of water vapor concentration do not exist in the numerical collector flow fields, so diffusiophoresis could be neglected (Seinfeld and Pandis, 1998). Finally, electrostatic forces have not been considered in the dispersed phase modeling.

2.4.3 Turbulence options

The effects of the continuous phase turbulent fluctuations, as calculated by the turbulence model, may or may not be included in the calculation of drop trajectories. For this reason, there are two options for the treatment of the continuous phase velocity term, u, in the equation

describing drop motion (equation 2.6). The choice of which to use depends on whether or not the continuous phase instantaneous velocity fluctuations should affect drop motion.

As described previously, in order for turbulent quantities to be accounted for in the solution of the continuous phase, the fluid velocities are assumed to have an average component, $\overline{u_i}$, and an instantaneous fluctuating component, u_i' (equation 2.4). The first option, then, for the continuous phase velocity in the equation of drop motion (equation 2.6) is to use only the average component of the continuous phase velocity. Otherwise, the continuous phase velocity that affects drop motion can be a summation of the average velocity component plus the instantaneous fluctuation component. Because the turbulent velocity fluctuations are not explicitly solved for in the continuous phase solution, the velocity fluctuation components must be statistically derived from the Reynolds stresses ($-\rho\overline{u_i'u_j'}$) computed by the turbulence closure model. An excellent review of the fundamentals of particle dispersion in turbulent flows, including a description of the relevant physical processes and options available for numerical modeling is provided by Shirolkar (1996).

2.4.3.1 Approach of past researchers

Both options for the treatment of the continuous phase velocity term in the equation of particle motion have been used in previous work in the area of numerical simulation of gas-particle flows. Authors who have used only the average component of the continuous phase velocity in their trajectory calculations and have obtained good agreement with experimental results include Griffiths and Boysan (1996), Laucks and Twohy (1998), Jurcik and Wang (1995), and others. However, many other researchers have included the effects of continuous phase turbulent fluctuations on particle motion in their work with successful results, including Abuseid et al. (1991), Gong et al. (1993), Frank and Schulze (1994), and others. These latter studies indicate that the inclusion of turbulent fluctuations in trajectory calculations is necessary for the accurate description of particle behavior and dispersion in fluid flow.

The necessity of including the effects of turbulence on particle motion is not well defined, but may be determined by the level of continuous phase turbulence in the system of interest. The air flow in both of the collectors is expected to be fairly turbulent, with a jet inlet Reynolds numbers of 10,000, considered an upper limit for impactor design (Marple and Rubow, 1986). Also present in the collectors is impinging flow on the collector surfaces, which could generate additional turbulence. Without any specific guidelines for the determination of when the inclusion of turbulent fluctuations in trajectory calculations is necessary, calculations of drop motion through the FROSTY and CSU 5-Stage collectors were performed using both options, with and without the inclusion of instantaneous velocity fluctuations. The solutions obtained were then compared with experimental calibration data in order to evaluate the necessity of including continuous phase velocity fluctuations to provide an accurate representation of drop motion in the numerical modeling.

2.4.3.2 Turbulence models

FLUENT provides two models that can be used to incorporate the effects of turbulent fluctuations on particle motion. These are the Discrete Random Walk (DRW) and the Continuous Random Walk (CRW) models. Both models are stochastic in nature and require the simulation of a large number of drop trajectories to provide a description of their turbulent dispersion in the flow field. The models differ in their statistical derivation of the instantaneous velocity terms from the Reynolds stresses.

There are many turbulent dispersion models in the literature (Gong et al., 1993; Fan et al., 1997; McFarland et al., 1997; etc) that use eddy lifetime approaches that are very similar in nature to the DRW model in FLUENT. The DRW is an eddy lifetime model in which particles are assumed to interact with a series of successive turbulent eddies which have velocity fluctuations associated with them. The magnitude of the velocity fluctuation (u') for a given

eddy is calculated by multiplying the square root of the continuous phase Reynolds stress by a Gaussian distributed random number (ξ). In the x-direction, this would be represented by:

$$u' = \xi\sqrt{\overline{u'u'}} \tag{2.10}$$

This provides a random velocity fluctuation that is based on the continuous phase Reynolds stress component as calculated by the turbulence closure model. The particle interacts with this velocity fluctuation for a given period of time, defined by the particle Lagrangian integral time scale, before coming under the influence of a new velocity fluctuation. The particle Lagrangian integral time scale is approximated in the DRW model as a portion of the life of the turbulent eddy with which the particle is interacting. Particle interaction is for only a fraction of the eddy lifetime because a particle may exit an eddy before the eddy lifetime is complete. The interaction time in the DRW model is therefore calculated as a random fraction of the lifetime of the eddy.

The eddy lifetime is defined by the fluid Lagrangian integral time scale, and is calculated from local continuous phase fluid turbulence quantities with the following equation:

$$T_L = \alpha\frac{k}{\varepsilon} \tag{2.11}$$

where k is the continuous phase turbulent kinetic energy, ε is the continuous phase turbulent dissipation rate, and α is a constant with default values of 0.15 for the k-ε turbulence model and 0.30 for the RSM. After a particle is influenced by a given velocity fluctuation for the calculated interaction time, a new velocity fluctuation and interaction time are calculated by equations 2.10 and 2.11.

The CRW model (Fluent, 1996) is another approach for defining the velocity fluctuations affecting the dispersed phase. Fluent, Inc. recommends the use of the CRW model over the DRW model because it provides a more realistic description of turbulent fluctuations. Because of that recommendation, the CRW model for particle dispersion was used for all simulations in which the effects of turbulence on drop motion were studied, although we found both models produced

comparable results. The CRW model uses a solution to the Langevin equation (Thomson, 1987) as the basis for the instantaneous velocity fluctuations:

$$du_i = \frac{1}{T} u_i dt + \left(\frac{2\overline{u_i' u_i'}}{T} \right)^{\frac{1}{2}} dw \qquad (2.12)$$

where w is a Gaussian distributed random number and T is the particle integral time, again estimated as the fluid Lagrangian integral time scale (T_L) using equation 2.11.

Trajectory calculations which included the effects of velocity fluctuations on drop motion through the use of the CRW model revealed that the collection of smaller drops in certain flow regimes was over predicted when compared to experimental data. In an effort to correct this modeling discrepancy, variations in the fluid Lagrangian integral time scale (T_L) were explored. The magnitude of T_L was modified by adjusting the value of α in equation 2.11. Values of α lower than those set as the default provided slightly better agreement with experimental results. During this study, it was determined that α=0.09 allowed the best, although still not perfect, agreement between numerical predictions and experimental observations. For this reason, all of the trajectory simulations which include the effects of continuous phase velocity fluctuations presented in the remainder of this work assume α=0.09. A detailed discussion regarding the over prediction of drop collection at small drop sizes, the effects of variations in α, and the selection of α for this work, will be presented in section 4.3.2.

2.4.4 Fluid properties, initial conditions, and boundary conditions

The drops used in the trajectory simulations were assigned a density of 0.90 g/cm^3. This value was selected to match the density of oleic acid, which was used in the laboratory portion of this study to experimentally calibrate the collectors. The choice of oleic acid drops for the experimental calibration will be detailed in section 3.2.2. It was desired to produce drop trajectory simulations using the model that could eventually be compared to data that were obtained during the experimental calibrations.

Boundary conditions were assigned to each of the collector surfaces so that the fates of the drops could be established and recorded. The "escape" boundary condition was used for the walls and impaction surfaces of the collectors. This boundary condition terminates a drop's trajectory calculation when the drop comes into contact with a surface. It was used to simulate the removal of drops from the air flow due to adhesion of the cloud drops to the collector surfaces upon contact. In the case of the FROSTY collector, in which the symmetry of the design allowed for the modeling of only half of the collector, the "reflect" boundary condition was used along the line of symmetry. The "reflect" boundary condition is used to simulate the motion of drops between the calculated continuous phase domain and an identical but opposite domain that is assumed to exist when using the symmetry boundary condition.

2.4.5 Dispersed phase modeling procedure

An analysis of dispersed phase trajectories through the collectors was initiated by first obtaining a continuous phase solution throughout the flow domain. Drops of a single diameter were then introduced into the continuous phase domain at 100 locations evenly distributed across the collectors' inlets. The drops were given an initial velocity equivalent to the velocity of the air entering the inlet. For trajectory calculations based on the mean continuous phase flow field, a single drop was injected at each of the input locations. Because the inclusion of continuous phase velocity fluctuations is a statistically based process as described above, for the simulations that included these effects, ten drops were introduced at each of the input locations. This resulted in the calculation of a total of 1000 trajectories, enough to provide a representative sample of turbulent drop dispersion through the collectors. Groups of drops were injected in this fashion for drop sizes ranging from 4 to 30 μm in 2 μm increments for the FROSTY collector and from 4 to 60 μm in 2 μm increments for the CSU 5-Stage collector.

The model records the locations where drop trajectories intersect walls and surfaces so that deposition patterns for each drop size could be quantified and collection efficiencies could be calculated. The collection efficiency for a given drop size can be evaluated for each stage by:

$$efficiency = \frac{number\ of\ drops\ collected\ on\ impaction\ surface}{number\ of\ drops\ entering\ the\ stage} \qquad (2.13)$$

By calculating trajectories for each drop diameter in the range of interest, and computing the collection efficiencies via equation 2.13, collection efficiency curves could be constructed for each stage, effectively defining the collection characteristics for the FROSTY and CSU 5-Stage collectors.

2.4.6 Continuous phase / dispersed phase coupling

The introduction of a dispersed phase into the continuous phase flow domain can result in modification of the continuous phase flow field. Source or sink terms for the transfer of particle momentum generated during the trajectory calculations can be included in subsequent recalculations of the continuous phase solution. Iterations between continuous phase solutions and drop trajectory calculations in this manner can account for the effects of momentum exchange or phase coupling.

The significance of this phase coupling was investigated for the FROSTY collector in order to determine if its inclusion in the solution procedure was necessary. A carrier phase solution was first obtained for the FROSTY collector's first stage. The dispersed phase was then introduced into the continuous phase flow domain at the collector inlet. The dispersed phase consisted of 10 μm drops at a flow rate of 36 g/hr, which corresponds to the sampling at 1500 l/min of a cloud having a liquid water content of 0.4 g/m^3. Momentum source terms calculated during these trajectory simulations were then incorporated into a new continuous phase solution. This procedure was repeated until a converged solution was obtained. An examination of the continuous phase velocity field for the coupled solution revealed that it changed negligibly from

the uncoupled velocity field. This is attributable to the very low volume fraction of cloud drops experienced in a typical cloud or fog. Because the coupled and uncoupled solutions produced nearly identical results, the extra computational effort necessary for a coupled solution was not justified. The analyses in this study, therefore, did not include coupling between the dispersed and continuous phases.

The topic of phase coupling is not addressed very often in the multiphase numerical modeling literature reviewed for this study, which was generally limited to investigations involving the analysis of low volumetric loadings of the dispersed phase in a Lagrangian framework. However, it is not hard to imagine that in cases where high dispersed phase loadings are considered, momentum transfer between phases may play an important role in the overall fluid behavior. In one example of this type (Frank and Schulze, 1994), phase coupling was performed and deemed necessary for the accurate representation of their problem. The system under study consisted of a downward facing nozzle emitting a spray of liquid drops into a moving airstream. In this case, however, the mass flow rate of the dispersed phase was more than seven orders of magnitude larger than the flow rate considered in this study.

3 Experimental Approach

3.1 Overview of technique

In addition to the numerical analysis of the FROSTY and CSU 5-Stage collectors, experimental calibrations were also performed. The experimental work provided a method of validating the results of the numerical modeling by establishing the true collection characteristics of the FROSTY and the CSU 5-Stage collectors. Collection characteristics were determined in the experimental method by introducing monodisperse drops into the collector in a range of diameters corresponding to the diameter range that would be experienced during actual operation. The drops were tagged with a fluorescent tracer so that their collection patterns could be quantified. This information was then used to generate the efficiency curves that define the performance of the collectors.

This technique has been used successfully in the past to validate the numerical modeling of particle deposition in gas-particle flows (McFarland et al., 1997; Muyshondt et al., 1996) as well as calibrate aerosol impactors (Marple et al., 1995; Marple et al., 1987; and Hillamo and Kauppinen, 1991).

3.2 Equipment Setup

The experimental calibration of the FROSTY and CSU 5-Stage collectors required the use of a number of individual components. A method for the production of drops in a monodisperse distribution was necessary. In order to assure correct operation of the drop generation system, procedures to monitor the size and quality of the drops were established. For calibration with the smallest drop size, a charge neutralization system was employed to eliminate

electrostatic effects. Finally, after introducing the drops into the collectors, a method for the measurement of drop collection patterns was needed.

3.2.1 Generation of monodisperse drops

Monodisperse drops were produced with a Vibrating Orifice Aerosol Generator (VOAG) Model 3450 from TSI, Incorporated (Berglund and Liu, 1973). The VOAG operates by forcing a solution containing volatile and non-volatile components through a small orifice at a constant flow rate to form a liquid jet. The orifice is vibrated at a known frequency, breaking the liquid jet up into drops of known volume (see Figure 3.1).

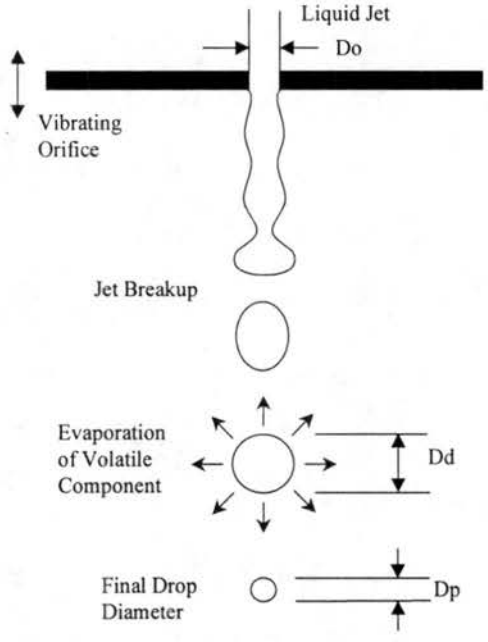

Figure 3.1 Generation of monodisperse drops through mechanical breakup of a liquid jet and subsequent evaporation.

The initial diameter of the drops that are produced can be determined using the following equation:

$$D_d = \left(\frac{6Q}{\pi f}\right)^{\frac{1}{3}} \tag{3.1}$$

where Q is the solution flow rate, and f is the frequency of vibration.

After the drops are produced, they pass through a drying column where the volatile component is evaporated, leaving drops composed entirely of the non-volatile fraction. The final diameter, after evaporation, is a function of the original diameter and the volumetric concentration of the non-volatile component in the solution. The following equation is used to calculate the final diameter of the drop:

$$D_p = (C + I)^{\frac{1}{3}} D_d \tag{3.2}$$

where D_d is the initial drop diameter, C is the volumetric concentration of the nonvolatile component in solution, and I is the volumetric concentration of nonvolatile impurities in the volatile component. Impurities present in the volatile component that do not evaporate will contribute to the final drop size and therefore need to be taken into account when calculating D_p.

During the calibration of the FROSTY collector, the generation of a range of final drop sizes from 4 to 30 μm was accomplished by varying only the volumetric concentration of non-volatile components in the drop solution. The VOAG operational parameters were held constant in order to produce drops with an initial diameter of 42 μm at all times. Subsequent evaporation of the variable volatile component fraction reduced the drops to the desired final diameter. To generate the initial 42 μm diameter drops, a syringe pump provided the flow of solution through the orifice to produce the liquid jet. For this work, a 20 μm orifice and a 20 ml syringe were used. The syringe pump speed was set to 7.6×10^{-4} cm/s to produce a flow rate of 0.139 cm^3/min. A voltage was applied to a piezoelectric ceramic ring holding the orifice assembly causing it to vibrate at 60 kHz.

The generation of drops for calibration of the CSU 5-Stage collector was performed with VOAG operational parameters and solution concentrations identical to those used for the FROSTY collector calibration for drop sizes from 4 to 24 μm. When an attempt to produce drops larger than 30 μm was made, however, a problem was encountered. The non-volatile concentration needed to form drops of that size was quite high, resulting in a very viscous drop

solution. The solution was so viscous, in fact, that formation of the liquid jet for the duration needed for the calibration efforts became impossible. To alleviate this problem, the liquid flow rate was increased to 0.170 cm^3/min by increasing the syringe pump speed to 1.0×10^{-3} cm/s. The higher flow rate had several benefits. First of all, at a constant vibrational frequency, the higher flow rate increased the size of the initial drop diameter that was generated. To arrive at final drop diameters then, a lower concentration of the non-volatile component could be used, effectively reducing the viscosity of the drop solution. Secondly, the higher liquid flow rate elevated the equilibrium pressure reached in the VOAG liquid feed system, producing a much stronger and more stable liquid jet. For these reasons, the higher syringe pump speed was used for the generation of 32 and 34 μm drops. Because of the added robustness provided by the increased pump speed, it was also used during the calibration of the CSU 5-Stage collector for the generation of 26 through 30 μm drops to help ensure successful drop generation. For future work involving the generation of monodisperse drops using the VOAG, use of the higher syringe pump speed would be recommended for all drop sizes.

Dispersion and dilution of the drops after production was necessary to prevent drop coalescence and allow for drying. Filtered compressed air was supplied to the VOAG to provide air for the dispersion and dilution of the droplet stream. The dispersion and dilution air flow rates were set to approximately 22 cc/min and 55 l/min, respectively. These flow rates were found to provide the optimal dispersion of the droplets to prevent the formation of doublets and triplets through excessive coagulation, and optimal transport of the droplets to allow enough residence time in the drying column for complete evaporation of the volatile component.

For the transportation of the calibration drops from the VOAG to the collector inlets, a rigid 3.8 cm inner diameter PVC tube was attached to the top of the VOAG's drying column and used to direct the flow of drops. In order to maintain VOAG outlet velocities capable of transporting calibration drops to the collector inlets while minimizing disruption of the inlet flow fields, a different outlet was used for each collector. For the FROSTY collector, with a first stage

inlet jet velocity of 5.8 m/s, a transition from the 3.8 cm ID PVC tube to a 0.8 by 2.5 cm rectangular outlet was used to provide a VOAG outlet velocity of 4.5 m/s. The unaltered 3.8 cm ID PVC tube provided a velocity of 0.8 m/s that was appropriate for the lower inlet velocity of the CSU 5-Stage collector (1.3 m/s). A three-way valve incorporated into this line allowed the flow of drops to be directed to the outlet or to be exhausted from the system through a filter. The blower that provided the necessary flow rates through the FROSTY and CSU 5-Stage collectors was attached to the collectors with 3.8 cm ID flexible lines. A schematic layout of the FROSTY collector experimental setup can be seen in Figure 3.2 and a photo of the setup can be seen in Figure 3.3. A schematic layout of the CSU 5-Stage collector experimental setup can be seen in Figure 3.4 and a photo of the setup can be seen in Figure 3.5.

3.2.2 Droplet solution components

The non-volatile drop solution component used for the calibration of the FROSTY and CSU 5-Stage collectors was oleic acid with an addition of a small amount of fluorescein. Isopropanol was used as the volatile component. Oleic acid, possessing an oily consistency, was chosen as the non-volatile component for the experimental calibration work because it has a density close to that of water, it is non-toxic and safe to work with, and it resists evaporation. Isopropanol was chosen as the volatile component due to its high evaporation rate and low viscosity and because it provided sufficient solubility of oleic acid. The addition of the powdered fluorescent tracer, fluorescein (EM Science, EM Industries, Inc.), to the calibration drops allowed the presence of drops on the collector impaction and wall surfaces to be detected and quantified. The addition of a fluorescent tracer to the drop solution required a modification to the calculation of the final drop diameter, as presented earlier, to account for the additional non-volatile fluorescein mass. The modified equation (Olan-Figueroa et al., 1982) can be expressed as:

$$D_p = \left[C + C\frac{C_f}{\rho_f} + I \right]^{\frac{1}{3}} D_d \qquad (3.3)$$

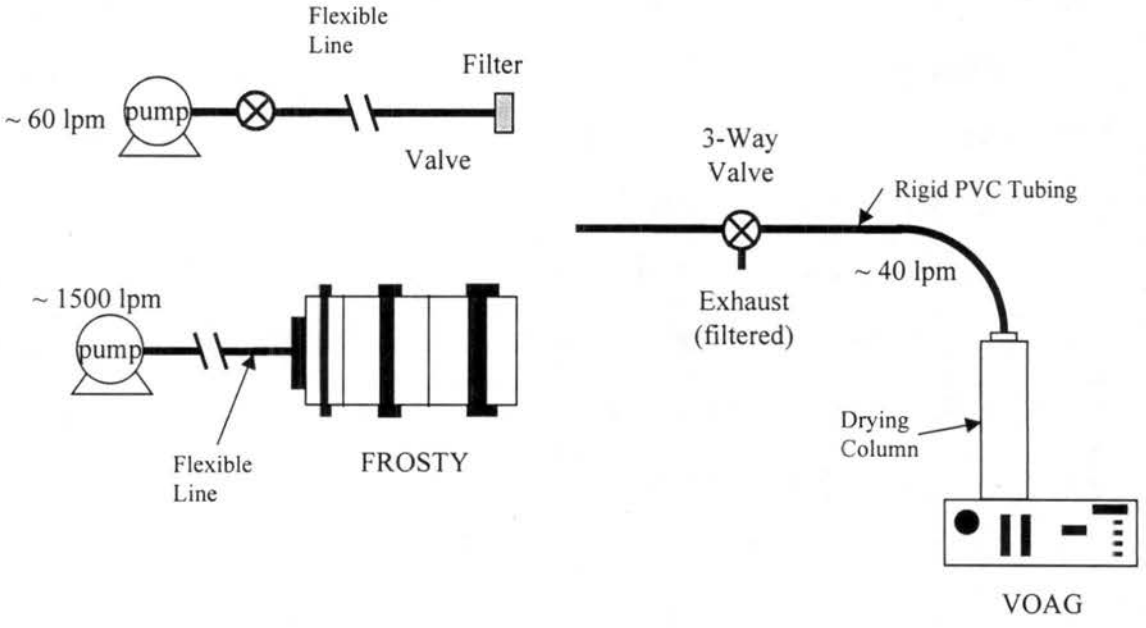

Figure 3.2 Schematic layout of the experimental setup used for the calibration of the FROSTY supercooled cloudwater collector.

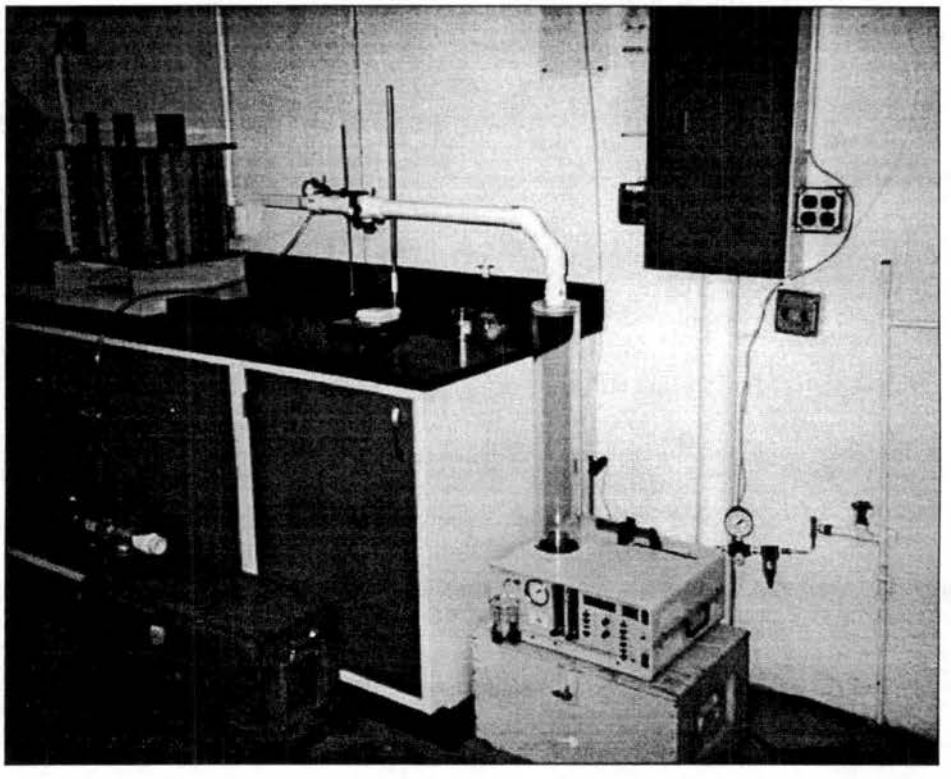

Figure 3.3 Photo of the experimental setup used for the calibration of the FROSTY supercooled cloudwater collector.

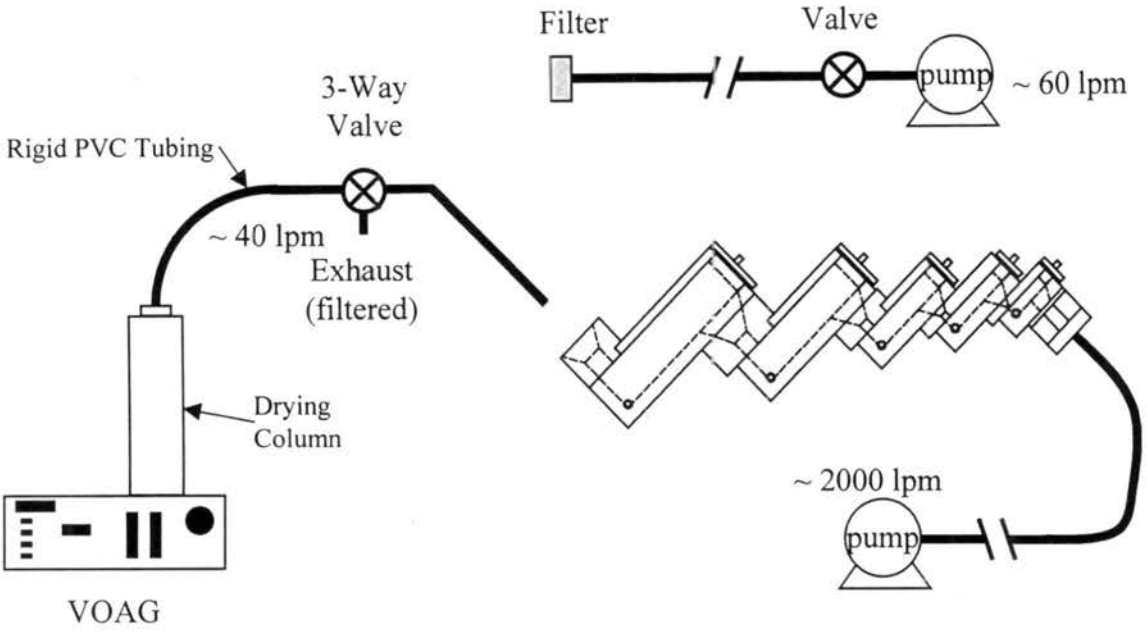

Figure 3.4 Schematic layout of the experimental setup used for the calibration of the CSU 5-Stage cloudwater collector.

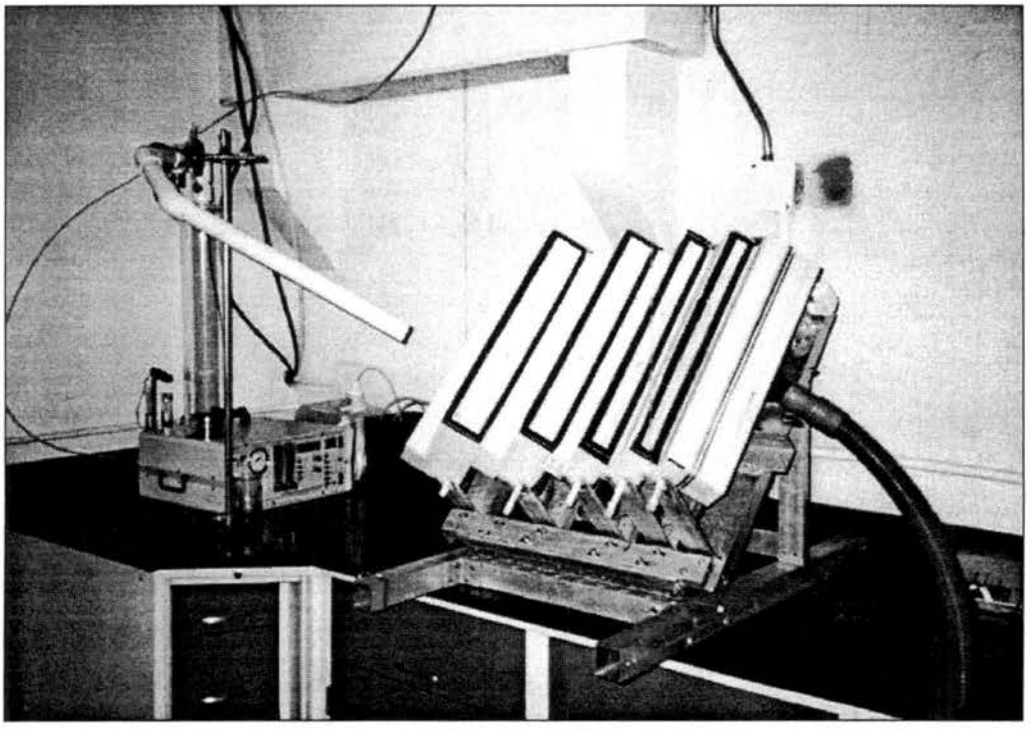

Figure 3.5 Photo of the experimental setup used for the calibration of the CSU 5-Stage cloudwater collector.

where D_d is the initial drop diameter, C is the volumetric concentration of oleic acid in solution, C_f is the concentration of fluorescein in oleic acid (on a mass of fluorescein per milliliter of oleic acid basis), ρ_f if the density of fluorescein, and I is the volumetric concentration of nonvolatile impurities in the volatile component. The reagent grade isopropanol that was used in this work had a nonvolatile impurity fraction of 0.4 to 1 ppm, negligibly affecting drop size.

A concern regarding this experimental calibration approach was contamination of the FROSTY and CSU 5-Stage collectors with fluorescein. The fluorescing properties of fluorescein are very similar to those of diacetyldihycholutidine, a fluorescing compound produced in the analysis of cloudwater formaldehyde, a constituent that is routinely measured. If the surfaces of the collectors retained any of the fluorescein used during the calibration procedure, subsequent formaldehyde measurements would be compromised. This issue was addressed by performing a number of extraction tests involving samples of the types of materials that would be exposed to fluorescein. Known quantities of an oleic acid / fluorescein solution were placed on samples of Plexiglas, Teflon, and Delrin. After five to ten minutes, the samples were extracted by washing with or soaking in deionized water. The extracts were measured with a fluorimeter, as will be described in section 3.2.5, to determine if all of the fluorescein had been recovered. These tests revealed that 100% of the fluorescein placed on the sample surfaces could be recovered in the extraction process, indicating that no future interference with formaldehyde measurement would occur.

Solutions were prepared by adding the correct mass of fluorescein, measured on a analytical balance, and the necessary volume of oleic acid, measured by pipette, to enough isopropanol to make 100 ml total volume, measured in a volumetric flask. Table 3.1 shows the proportions of oleic acid and fluorescein used to produce drops of a desired diameter for the lower syringe pump speed while Table 3.2 shows these values for the higher syringe pump speed used in this study. The concentration of fluorescein in oleic acid (C_f) was decreased for increasing drop size so that all drop sizes would contain approximately the same mass of

fluorescein. Based on the selected values of C_f, the mass of fluorescein added to 100 ml of the oleic acid / isopropanol solution was in the range of 0.05 to 0.09 g. Once made, the drop solution was allowed to sit for several days to allow the fluorescein to dissolve completely.

Final Drop Diameter µm	Fluorescein Cf g/ml	Non-volatile Concentration vol %	Volume of Oleic Acid ml	Mass of Fluorescein g
4	1	0.0005	0.052	0.0524
6	0.2	0.0026	0.259	0.0518
8	0.1	0.0065	0.652	0.0652
10	0.05	0.0131	1.313	0.0657
12	0.03	0.0230	2.298	0.0689
14	0.02	0.0367	3.673	0.0735
16	0.01	0.0552	5.518	0.0552
18	0.009	0.0786	7.862	0.0708
20	0.007	0.1080	10.799	0.0756
22	0.005	0.1439	14.392	0.0720
24	0.003	0.1871	18.710	0.0561
26	0.003	0.2379	23.788	0.0714
28	0.002	0.2973	29.730	0.0595
30	0.002	0.3657	36.566	0.0731

Table 3.1 Volume of oleic acid and mass of fluorescein needed to produce 100 mL of droplet solution. Generation of the indicated final drop diameter requires a VOAG syringe pump speed of 7.6×10^{-4} cm/s.

Drop Diameter µm	Fluorescein Cf g/ml	Non-volatile Concentration vol %	Volume of Oleic Acid ml	Mass of Fluorescein g
20	0.007	0.0885	8.853	0.0620
22	0.005	0.1180	11.798	0.0590
24	0.004	0.1533	15.328	0.0613
26	0.003	0.1950	19.501	0.0585
28	0.003	0.2436	24.356	0.0731
30	0.002	0.2998	29.976	0.0600
32	0.002	0.3638	36.380	0.0728
34	0.002	0.4364	43.636	0.0873
36	0.0015	0.5182	51.816	0.0777
38	0.001	0.6096	60.960	0.0610
40	0.001	0.7110	71.101	0.0711

Table 3.2 Volume of oleic acid and mass of fluorescein needed to produce 100 mL of droplet solution. Generation of the indicated final drop diameter requires a VOAG syringe pump speed of 1.0×10^{-3} cm/s.

3.2.3 Size verification and imaging system

For each of the drop sizes produced, the diameters of drops collected on glass slides were confirmed with the use of an optical microscope imaging system. Drops that are collected on an untreated glass slide undergo considerable spreading which results in difficulty in relating the drop's measured flattened diameter to the original spherical diameter. In order to minimize the drop spreading effects, the drops were collected on glass slides treated with an oleophobic fluorochemical coating. Although some spreading still occurs on the treated surface, the drops better retain their spherical shape making more precise measurements possible. Fluorad FC-722 (3M Industrial Chemical Products Division) was used as the coating during this work because the spreading behavior of oleic acid drops on glass slides treated with this coating has been thoroughly investigated. The ratio of the flattened diameter to the original spherical diameter was taken to be 1.33, as suggested by previous work (Olan-Figueroa et al., 1982). Figure 3.6 shows a typical image obtained with the imaging system at 30× magnification for 34 μm drops, showing a majority of singlets and a smaller fraction of doublets.

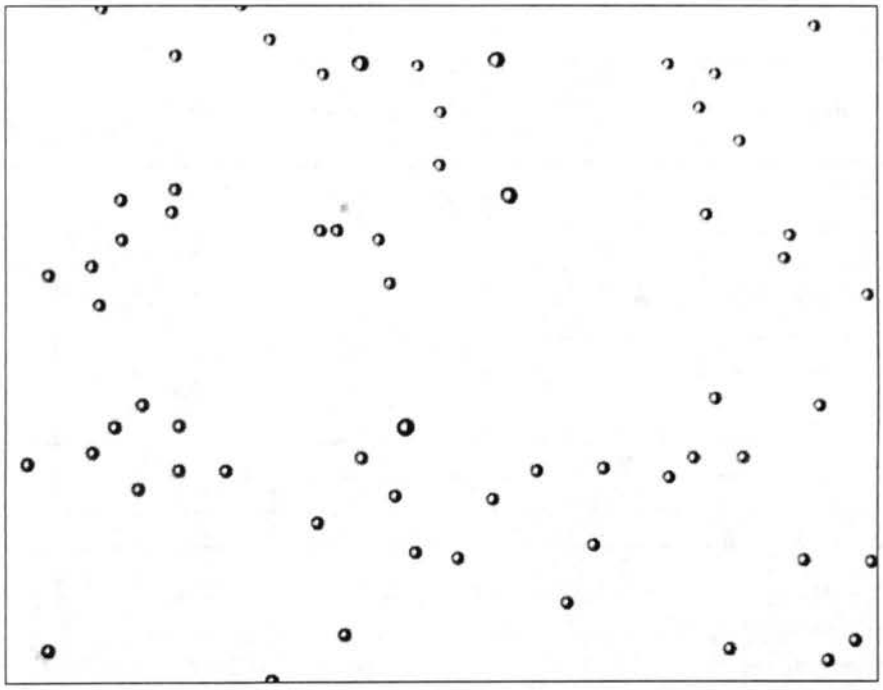

Figure 3.6 Image taken at 30× magnification of 34 μm drops collected on an oleophobic coated glass slide.

The consequences of doublets and triplets in the drop stream will be discussed in detail in section 3.4.1. Drops 34 μm in diameter viewed at a higher magnification of 150× in Figure 3.7 provide a comparison between singlets, a doublet in the lower part of the frame, and a triplet in the upper right hand corner.

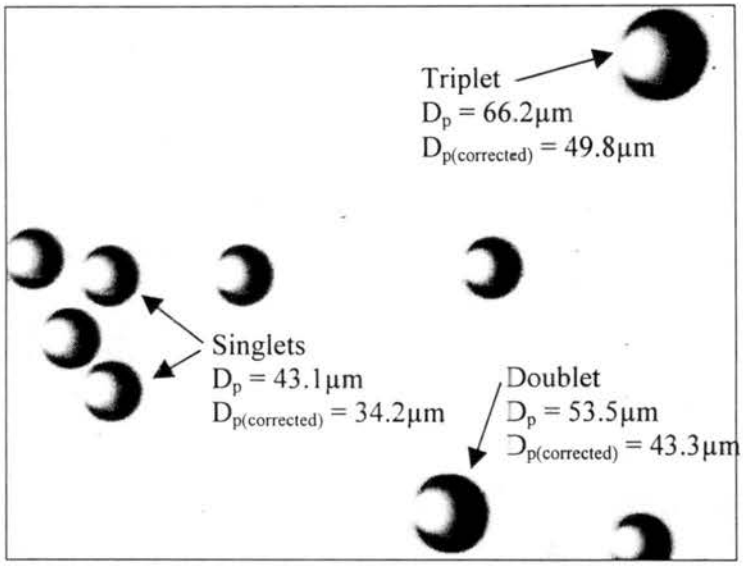

Figure 3.7 Image taken at 150× magnification of 34 μm drops collected on an oleophobic coated glass slide. Multiplets are included for comparison.

The imaging system used to view the drops consisted of a Nikon SMZ-U stereo zoom microscope, a Javelin Ultrachip CCTV video camera to capture, digitize, and transfer images to a PC, and image processing software. Resolution to approximately one micron was possible with this system. Image calibration and drop diameter measurements on the digitized images were made with the image processing software, Image Pro Plus, V1.2. The VOAG is capable of producing drops with extremely uniform diameters. Berglund and Liu (1973) reported a standard deviation of 1% of the mean drop diameter. This variation was smaller than could be assessed by the imaging system used for drop size verification, which was limited by the resolution of the screen images. Due to this limitation, drops could only be measured with an accuracy of ± 0.6 μm for all drop sizes. Taking this into account, measured drop diameters agreed very well with the desired drop diameters that were based on non-volatile solution concentrations, VOAG

operating parameters, and the appropriate spreading factor. Table 3.3 shows the measured drop diameters (corrected for spreading) for each of the desired drop sizes produced during the calibration.

			Measured Diameters (corrected for drop spreading)					
Desired	Doublet	Triplet	FROSTY			CSU 5-Stage		
Drop Dia.	Diameter	Diameter	Singlet	Doublet	Triplet	Singlet	Doublet	Triplet
μm	μm	μm	μm	μm	μm	μm	μm	μm
34	42.8	49.0	N/A	N/A	N/A	34.2	43.3	49.8
32	40.3	46.2	N/A	N/A	N/A	32.4	40.2	47.3
30	37.8	43.3	29.8	35.7	43.4	30.3	39.9	45.1
28	35.3	40.4	27.9	37.6	42.8	28.4	37.5	43.3
26	32.8	37.5	25.9	34.4	41.5	25.9	32.3	36.8
24	30.2	34.6	23.3	29.4	33.3	23.8	30.9	38.0
22	27.7	31.7	21.4	28.5	32.4	21.3	28.4	31.7
20	25.2	28.8	20.2	24.8	30.6	20.1	29.2	36.3
18	22.7	26.0	18.1	22.6	28.4	18.1	24.6	28.4
16	20.2	23.1	16.3	20.2	22.8	16.1	20.6	23.2
14	17.6	20.2	13.7	17.6	20.8	13.6	16.8	20.0
12	15.1	17.3	12.3	14.6	17.5	11.6	14.9	18.1
10	12.6	14.4	9.7	12.3	14.2	9.7	11.7	14.3
8	10.1	11.5	7.8	10.4	11.0	7.8	9.7	11.6
6	7.6	8.7	5.8	7.7	9.7	5.8	7.1	9.1
4	5.0	5.8	4.5	5.8	6.5	3.9	5.2	5.8

Table 3.3 Comparison of desired drop diameters and measured drop diameters for the FROSTY and CSU 5-Stage collectors. Measured diameters are corrected for drop spreading with a factor of 1.33 and have an accuracy of ± 0.6 μm imposed by the imaging system.

3.2.4 Charge neutralization

Neutralization of the drops produced by the VOAG was initially considered unnecessary due to the large size of the drops involved in the experimental calibration. However, during calibration of the FROSTY collector with 4 μm drops, a high percentage of drops of that size were collected on the first stage. This behavior was contrary to the first stage collection pattern that had been developing. As smaller drops were introduced into the collector, first stage collection efficiency was steadily decreasing, as would be expected. Collection efficiencies for the three drop sizes immediately larger than the 4 μm size (10, 8, and 6 μm) were measured as 6%, 2.5% and 1.5%, respectively. However, this first stage collection efficiency pattern was disrupted when a collection efficiency of 36% was recorded for the 4μm drop size. Subsequent trials with 4 μm drops revealed highly variable collection rates on the first stage.

After some consideration, electrostatic effects due to drop charge were considered as a possible cause for the observed erratic drop collection. A TSI, Incorporated Model 3054 Aerosol Neutralizer with a Krypton-85 source was placed in line directly after the VOAG's drying chamber to reduce the charge on the drops to equilibrium levels. With the neutralization system in place, calibration efforts with the 4 μm drops were much more repeatable and consistent with the first stage collection efficiency trend that had been developing. The charge neutralizer was used during the 4 μm drop calibration procedure for the CSU 5-Stage collector as well.

3.2.5 Quantification of droplet collection

The quantification of droplet collection on the impaction surfaces and collector walls was accomplished by soaking these surfaces in a known volume of an extract solution or washing them with a known volume of extract solution. The fluorescein present in the drops adhering to a given surface dissolved into the extract solution, which was then measured with a Shimadzu RF-1501 Spectrofluorophotometer. A calibration of the fluorimeter was performed before every measurement session using five standards having fluorescein concentrations of 0.0025, 0.005, 0.01, 0.02, and 0.04 μg/ml.

Problems obtaining consistent extract measurements were encountered when using pure deionized water as the extract solution. It was found that an extract solution made basic by an addition of sodium hydroxide (NaOH) provided for more efficient dissolution of the fluorescein and oleic acid and more reliable extract measurements. An extract solution of 0.001 N NaOH, as used by others (Marple et al., 1987), eliminated the problem of inconsistent measurements. Three measurements were made for each fluorimeter calibration standard and each extract solution. The extract concentrations, as determined from the fluorimeter measurements, were multiplied by the extract volumes in order to ascertain the mass of fluorescein, and therefore the number of drops, that had been deposited on each specific surface during the collector calibration procedure.

In addition to the fluorimetric analysis of drop collection patterns throughout the collectors, measurements of the total number of drops entering the collectors were also made. This was necessary in order to calculate drop collection on any given surface as a percentage of the total number entering the collector. The total number measurement was accomplished by collecting drops on filters at the VOAG outlet immediately before and after drops were directed into a collector. Drops were collected for an identical duration on the pre-filter, in the collector, and on the post-filter during a calibration. The filters were soaked in the 0.001 N NaOH extract solution to remove the collected fluorescein and measured with the fluorimeter as described above. It was assumed that if the numbers of drops collected on the pre and post-filters for a given time period were the same, then that would also represent the total number of drops entering the collector in the intervening equal time period.

For the filter collection, a 47 mm diameter, 1 μm diameter pore size, Nylasorb nylon membrane filter mounted in an interchangeable Plexiglas filter pack was placed directly in front of the VOAG outlet. A pump was used to draw air through the filter at approximately 80 to 100 l/min to ensure that the entire drop laden flow of 55 l/min from the VOAG was captured. The air flow rate through the filter was controlled by a ball valve and monitored by an Alicat Scientific, Inc. gas flowmeter. A 0.95 cm ID flexible line was used to connect the pump to the filter pack. The use of flexible lines allowed for the placement of either the collector or the filter in front of the VOAG outlet, as necessary.

Replicate measurements were performed to assess the reproducibility of fluorescein collection and measurement using the nylon membrane filters. The VOAG was used to generate 8 μm fluorescein tagged drops which were collected on four filters consecutively for a duration of one minute each. The filters were soaked in extract solution which was then measured by fluorimetry to determine the fluorescein content. After multiplying the extract concentration by the extract volume, values of fluorescein mass on the four filters were 66.9 μg, 64.6 μg, 65.7 μg, and 66.2 μg, for a mean value of 65.9 μg. These measurements have a 95% confidence interval

of ±1.6 μg, or ±2.4% of the mean, suggesting that the filters provide a precise method for quantifying the number of drops produced by the VOAG. During the FROSTY and CSU 5-Stage collector calibration procedures, differences between the pre and post-filters were generally 3% or less. If the filters differed by more than 5%, the calibration data were disregarded.

To determine the overall reproducibility of the calibration procedure, measurements of collection efficiencies of the FROSTY collector were repeated five times for 18 μm drops. A fraction of 18 μm drops are collected on each of the three stages of the FROSTY collector, so replicates for 18 μm drops were performed in order to obtain information about all three stages simultaneously. It was expected that the reproducibility of calibration with 18 μm drops would be representative of other drop sizes. Two replicates were completed for 4 μm and 28 μm drops as a check of this assumption. Table 3.4 shows the collection efficiency results for each 18 μm drop size replicate along with the calculated averages, standard deviations, and 95% confidence limits for each stage. The efficiencies listed in Table 3.4 are adjusted to account for the presence of multiplets. The 95% confidence limits, as a percentage of the mean values, are ±14.1% for the first stage, ±5.7% for the second stage, and ±7.7% for the third stage. These confidence limits are based on average efficiencies obtained from five measurements. There is greater uncertainty in the collection efficiency values for other drop sizes in which only one measurement was made. In this case, the appropriate 95% confidence limits (based on the standard deviation of the 18 μm drop replicates) are ±31.4%, ±12.8%, ±20.4% of the mean for the first, second, and third stages, respectively. Two replicates were performed for the 4 and 28 μm drop sizes; the means provide a slightly better estimate of the true collection efficiency than a single measurement. For these drop sizes, the 95% confidence limits are, again based on the standard deviation measured for the 18 μm drops, ±22.2% for the first stage, ±9.2% for the second stage, and ±14.4% for the third stage. Error bars on the FROSTY collector experimental efficiency curves presented in the following chapter reflect these values. Although replicates at additional drop sizes would better define the confidence limits, time limitations prevented additional measurements.

	Stage 1 %	Stage 2 %	Stage 3 %
18 µm drops			
repetition 1	42.0	20.4	2.9
repetition 2	49.9	22.3	2.5
repetition 3	36.7	23.2	2.6
repetition 4	43.2	21.4	2.7
repetition 5	40.3	21.6	2.4
average	42.4	21.8	2.6
standard dev.	4.8	1.0	0.2
95% CL	6.0	1.2	0.2
95% CL (% of avg.)	14.1	5.7	7.7
28 µm drops			
repetition 1	79.5	1.1	0.3
repetition 2	81.6	1.5	0.3
average	80.6	1.3	0.3
4 µm drops			
repetition 1	1.1	0.9	20.6
repetition 2	0.0	0.1	17.6
average	0.6	0.5	19.1

Table 3.4 Collection efficiencies, averages, and 95% confidence limits for replicate calibrations of the FROSTY supercooled cloud collector.

Calibration of the CSU 5-Stage collector with a single drop size required approximately an eight hour day for setup, drop generation, drop size and multiplet measurement, extraction, fluorimetric measurement, and cleanup. Due to this lengthy process, no replicates were performed for the CSU 5-Stage collector. To provide estimates of the 95% confidence limits for the CSU 5-Stage collector, data from the FROSTY collector's five replicates at the 18 µm drop size were applied. It was assumed that the higher variability observed in efficiency measurements for the first stage of the FROSTY collector would also characterize the first stage of the CSU 5-Stage collector. Therefore, the first stage 95% confidence limits appropriate for single measurements of collection efficiency were assumed to be ±31.4% of the mean. The lower variability observed for the second and third stage FROSTY collector measurements suggested that confidence limits based on pooled statistical data from both stages would be most applicable to the second, third, fourth, and fifth stages of the CSU 5-Stage collector. When this approach is taken, the calculated 95% confidence limits for single measurements of collection efficiency are

±13.9% of the mean. These 95% confidence limits for the CSU 5-Stage collector are presented as error bars in the experimental collection efficiency curves provided in chapter 5.

3.3 Experimental Procedure

A typical calibration began by mounting a syringe filled with a solution for producing a desired drop size in the VOAG and starting the syringe pump. The VOAG required five to ten minutes for the liquid feed system pressure produced by the syringe pump to come into equilibrium, a requirement necessary for a constant flow rate for the production of consistently sized drops. While the liquid pressure was stabilizing, usually reaching a final value in the range of 14 to 16 psi at the lower syringe pump speed and 20 to 26 psi for the higher syringe pump speed, the valves controlling the VOAG dispersion and dilution air flows were opened. During this transient period, the flow of drops was exhausted from the system through the three-way valve.

A filter pack containing a Nylasorb filter was attached to the pump and positioned in front of the VOAG outlet. When the liquid pressure in the VOAG reached equilibrium, the pump was started and drops were collected on a pre-filter for one minute. Collection on the filter was initiated by changing the position of the three-way valve to direct the droplet stream to the VOAG outlet. After the one-minute collection period, the three-way valve was again used to return the flow to the exhaust port. The collector was then moved into position in front of the VOAG outlet, the blower was turned on and drops were allowed to flow into the collector for one minute, again with the flow of drops being controlled by the three-way valve. Finally, a new filter pack was attached to the pump and drops were again collected for one minute following the same procedure as for the first filter.

Following the collection process, each filter was placed in a separate 200 ml beaker to which 100 ml of the 0.001 N NaOH solution was added for the extraction process. When working with the FROSTY collector, the impaction surfaces could be removed from the collector.

The first stage impaction surface was removed from its support and placed into a two liter graduated cylinder and submerged in 1400 ml of the extraction solution. The second two stages were each placed into one liter graduated cylinders and submerged in 1000 ml of extract solution. The filters and the impaction surfaces were allowed to soak for approximately one hour to ensure that all of the fluorescein was transferred from the drops to the extract solution. For selected drop sizes, the walls of the collector were washed with the 0.001 N NaOH solution to determine wall losses in the collector.

Unlike the FROSTY collector, the impaction surfaces of the CSU 5-Stage collector can not be removed, so that soaking them was not an option for extraction. In this case, the removal of the fluorescein tagged calibration drops from the impaction surfaces was accomplished by washing the impaction surfaces with a known volume of extract solution. Typically, 250 ml of the extract solution was sprayed onto each impaction surfaces through the use of a spray bottle. The extract solution washed over the surface and flowed down to the sample collection ports, where it accumulated in Nalgene bottles. A second washing with an additional 150 ml of extract solution was performed to ensure that all of the fluorescein was removed from the surfaces. For measurements of the collector walls needed to quantify interstage losses, washing was not an option due to the orientation of the collector. For these surfaces, 5 mil UV stabilized plastic sheets (manufactured by W.J. Dennis & Co.) available at a local hardware store were used as liners that could be removed after the collection period. These liners were placed in 700 to 900 ml of extract solution along with the stage access lids. This procedure resulted in a number of surfaces with potentially small amounts of fluorescein being soaked in relatively large volumes of extract solution. Any small bias in the fluorimetic measurement of these low concentrations could result in errors that would be amplified when multiplied by large extract volumes to determine the total fluorescein mass. Due to this possibility, blank corrections were performed for all of the CSU 5-Stage collector extracts. These corrections had negligible effects, however, and were probably unnecessary.

All of the extracts were then measured with the fluorimeter to determine fluorescein concentrations. The filter extracts were diluted by a factor of ten prior to measurement in order to reduce their concentration to within the range of fluorimeter calibration.

This procedure was repeated for drop diameters from 4 to 30 μm for the FROSTY collector and from 4 to 34 μm for the CSU 5-Stage collector, in two micron increments. The extract concentrations were multiplied by the extract volumes to determine the mass of fluorescein collected on the filters and on the collectors' surfaces. Because monodisperse drops were used for the experimental calibration, each drop of a given size should contain an identical mass of fluorescein. Therefore, the mass of fluorescein that is measured on a surface can be used as a measure of the number of drops that were collected on that surface. For this relationship to hold true, however, the mass of fluorescein on the surface associated with multiplets must be accounted for. The necessity for this correction will be discussed in the following section. The stage collection efficiency equation for a given drop diameter used in the numerical modeling (equation 2.13) can be expressed in terms of mass of fluorescein instead of number of drops:

$$efficiency = \frac{mass\ of\ fluorescein\ on\ impaction\ surface}{mass\ of\ fluorescein\ entering\ the\ stage} \tag{3.4}$$

3.4 Efficiency curve considerations

For the collection efficiency to be calculated based on experimental data using equation 3.4, two factors needed to be taken into consideration and possibly corrected for. Corrections for doublets and triplets in the calibration drop stream and corrections for wall losses and drop removal by previous stages had to be made in order to generate the collection efficiency curves for each stage.

3.4.1 Correction for doublets and triplets

During the dispersion of drops after their initial formation, some amount of coagulation inevitably occurs. Doublets are formed when two individual drops collide and coalesce. Because

the volumes are additive, doublets have twice the volume of individual drops of the desired diameter. Similarly, triplets, with three times the volume of the desired diameter drops, are formed when three drops coalesce. The dispersion air flow in the VOAG can be adjusted, as mentioned previously, to minimize the formation of doublets and triplets. However, their presence can not be entirely eliminated.

Because collection characteristics vary for different size drops, the presence of doublets and triplets in the calibration drop stream must be accounted for (Marple et al, 1987). During the experimental calibration of the FROSTY and CSU 5-Stage collectors, it was assumed that each singlet contained an identical mass of fluorescein, and therefore the mass of fluorescein measured in a surface extract would be proportional to the number of drops collected on that surface. A doublet with twice the volume of a singlet contains twice the mass of fluorescein, and consequently will simply appear as two singlets in the fluorimetric analysis. Likewise, a triplet will appear as three singlets in the analysis. Doublets and triplets also possess more inertia than a singlet, and so are more likely to be collected on an impaction surface. In the case where multiplets are collected on a surface when singlets would not be, the entire mass of fluorescein on that surface would be attributed to singlets if the presence of the doublet and triplets were not accounted for. In this case, the presence of multiplets would have resulted in the calculation of erroneously high efficiencies. Fortunately, the diameters of the doublets and triplets of a given drop size can be precisely calculated, and by knowing their collection characteristics, their effects can be corrected for.

In the first stage of the FROSTY and CSU 5-Stage collectors, multiplets in the calibration drop stream were always collected with a higher efficiency than singlets, resulting in a downward correction of the collection efficiencies. However, it must be noted that multiplets are formed in the calibration air stream at the expense of singlets. So if multiplets are removed with a higher efficiency than singlets in the first stage of the collector, fewer drops are available for collection in the remaining stages than if all the drops originally existed as singlets. In this case, when

multiplets are removed from the air stream in previous stages when singlets would not have been, there will be fewer singlets available for collection on a given surface. This case results in the calculation of erroneously low efficiencies. It was generally observed in the later stages of both collectors that this case existed for drops with large enough diameters that multiplets were previously removed with a fairly high efficiency. For these drop sizes, the efficiencies were corrected upward. However, at smaller drop sizes, when multiplets are collected with a fairly low efficiency in the previous stages, numerous multiplets will remain in the air stream. When these multiplets reach the ensuing impaction surface and have a higher collection efficiency than singlets, the former case reverts and once again the singlet collection efficiency must be adjusted downward.

The magnitude of the correction for multiplets was dependent on the number of doublets and triplets in the drop stream. The imaging system described in section 3.2.3 was used to visually determine the fraction of doublets and triplets being produced by the VOAG for each drop size. The digitized drop images taken for the purpose of confirming the diameter of drops being produced were also used to count the number of doublets and triplets. For each drop size, a population of 500 to 1000 drops was used for this analysis. The number of doublets was typically found to be about 10% of the total number of drops, while triplets averaged about 1% of the total when the FROSTY collector experimental setup was used. Slightly lower fractions of doublets and triplets were observed with the CSU 5-Stage collector experimental setup, possibly due to the higher removal rate of larger drops in the longer and more circuitous tube needed to transport and introduce the calibration drops into the collector inlet at the correct angle. Table 3.5 displays the fraction of singlets, doublets, and triplets that were measured for each drop diameter produced. Based on these measurements, collection efficiencies that take the multiplets into account could be calculated as will be described in section 3.4.3. The magnitude of the adjustments to collection efficiency percentages due to doublets and triplets is presented in Figure 3.8 for the FROSTY collector and Figure 3.9 for the CSU 5-Stage collector.

Desired Drop Dia. µm	FROSTY			CSU 5-Stage		
	Singlet %	Doublet %	Triplet %	Singlet %	Doublet %	Triplet %
34	N/A	N/A	N/A	97.3	2.5	0.2
32	N/A	N/A	N/A	97.2	2.2	0.6
30	89.0	9.3	1.6	95.2	4.2	0.6
28	89.0	9.2	1.8	93.0	6.1	0.9
26	85.6	11.6	2.8	93.4	5.6	0.9
24	93.6	5.7	0.7	96.1	3.3	0.6
22	84.6	13.5	1.8	93.4	5.8	0.8
20	87.9	9.7	2.5	82.9	13.9	3.2
18	88.1	10.1	1.8	94.3	4.7	1.0
16	86.8	11.2	1.9	93.7	5.3	1.0
14	89.9	9.2	0.9	91.6	7.5	0.9
12	85.5	12.6	1.9	91.7	6.9	1.3
10	86.6	11.7	1.8	92.4	6.1	1.5
8	87.9	10.1	2.0	91.5	7.5	1.0
6	89.3	9.0	1.7	92.1	6.4	1.5
4	89.2	9.3	1.5	94.8	4.3	0.9

Table 3.5 Percentage of singlets, doublets, and triplets present in the calibration drop stream for the FROSTY and CSU 5-Stage collector calibrations.

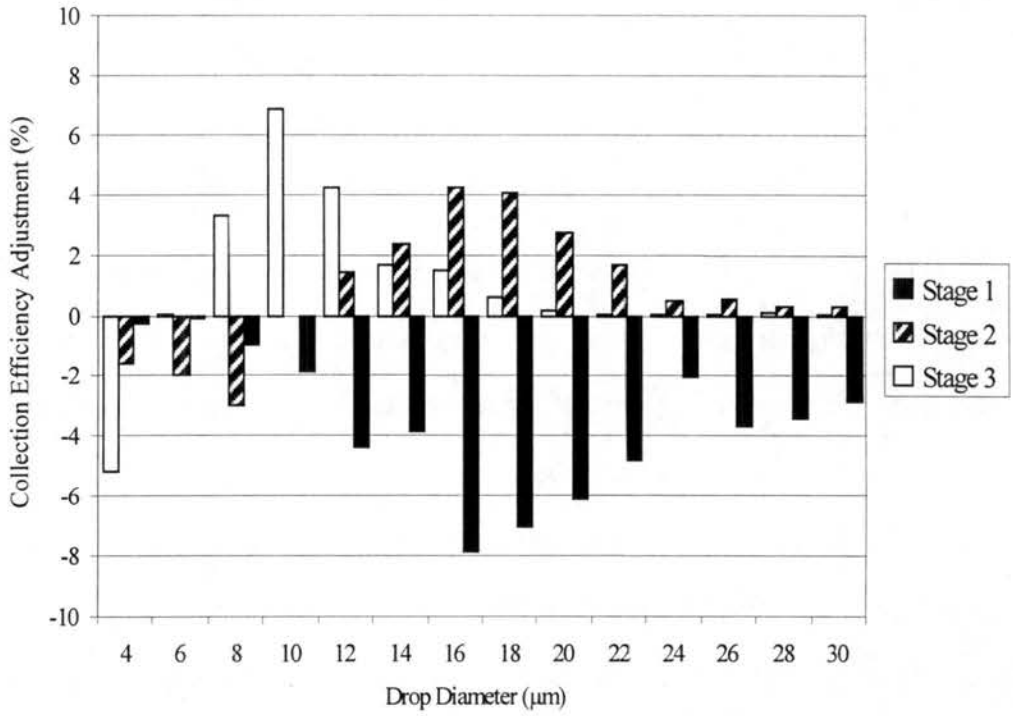

Figure 3.8 Adjustments to the FROSTY collector efficiency curves due to the presence of multiplets in the calibration drop stream.

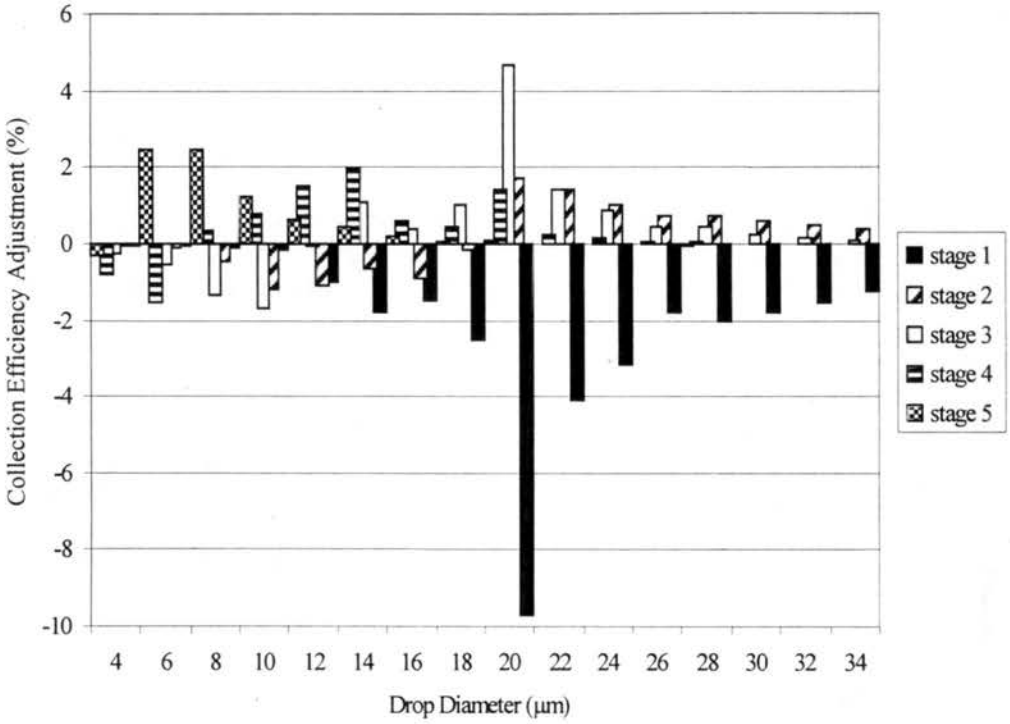

Figure 3.9 Adjustments to CSU 5-Stage collector efficiency curves due to the presence of multiplets in the calibration drop stream.

3.4.2 Correction for previous stage collection and wall losses

The second factor that needed to be accounted for in the efficiency calculation using equation 3.4 was collection by previous stages and wall losses. As noted by Swanson et al. (1996), most multi-stage impactor calibrations, both numerical and experimental, in the literature treat each stage independently and perform stage calibrations separately (Jurcik and Wang, 1995; Hillamo and Kauppinen, 1991). This produces a traditional S-shaped calibration curve for each stage in which collection efficiency rises from 0% to 100% as drop size increases. However, this procedure neglects the effects of overall flow patterns, interstage wall losses, and particle collection by previous stages that occur when the multiple stages are used together in series. When the stages are used in series, drops that are collected by earlier stages, or are lost to the walls, will not be available for collection by later stages. Instead of using equation 3.4, the true collection efficiency of a stage in actual use is calculated by dividing the mass of fluorescein (or

number of drops) on an impaction surface by the total mass of fluorescein (or total number of drops) entering the collector for a given drop diameter. Except for the first stage, the resulting efficiency curves do not have an S-shape, but rather have a peak after which efficiency decreases with increasing drop diameter. This decrease in collection efficiency with increasing drop diameter is a result of the larger drops not being available for collection due to their removal upstream. This type of curve more accurately reflects the actual percentage of the total number of drops entering the collector that will be collected on each impaction surface during operation.

In order to report the efficiency curves in the more traditional S-shape, single stage format, the mass of fluorescein collected on an impaction surface is divided only by the mass of fluorescein entering the stage to calculate efficiencies, as in equation 3.4. For the experimental calibration, however, the mass of fluorescein entering a stage was not directly measured. This value had to be derived for each stage by subtracting the mass of fluorescein lost to the upstream walls and the mass of fluorescein collected by previous stages from the measurement of the total mass of fluorescein entering the collector.

When dealing with very low collection rates, however, use of equation 3.4 to produce a traditional S-shaped efficiency curve may not yield meaningful results. For example, when calibrating the CSU 5-Stage collector with 30 μm drops, nearly all of those drops are collected in the first two stages, leaving a minimal fraction to be collected in the remaining three stages. Although these last three stages should have collection efficiencies of nearly 100% for 30 μm drops, arriving at that value by comparing the tiny mass of fluorescein measured on the stage by the indirectly derived tiny mass of fluorescein reaching the stage was not always practical. Small amounts of error in either of those numbers could result in large errors in the efficiency calculation. This was observed as extreme variability in the collection efficiency curves for larger drop sizes during the analysis of the second and third stages of the FROSTY collector and the third, fourth, and fifth stages of the CSU 5-Stage collector. The traditional S-shaped experimental efficiency curves for those stages, as will be presented in the next two chapters, are

truncated to remove efficiency calculations based on low confidence data. In actuality, the truncated portions of the collection efficiency curves do not hold much meaning anyway. Because the majority of large drops are removed from the air stream early in the collector, the few that remain in the later stages contribute negligibly to the total mass there. A description of their collection patterns is therefore not particularly beneficial.

Efficiency curves reflecting the actual collection efficiencies for each stage as well as efficiency curves transformed into the traditional S-shaped format by correcting for wall losses and previous stage collection will be presented for each collector in the following two chapters.

3.4.3 Efficiency curve correction spreadsheet

The corrections for the presence of multiplets, wall losses, and previous stage collection needed to produce the traditional S-shaped collection efficiency curves were performed in an EXCEL spreadsheet. Efficiency calculations for the first stage of both collectors were the most straightforward. No wall losses and no collection by previous stages had to be taken into account. However, the presence of doublets and triplets was corrected for. The mass of fluorescein associated with drops entering the first stage was assumed to be equal to the average mass of fluorescein collected on the pre- and post-filters. Because this mass of fluorescein was distributed among singlets, doublets, and triplets, it was allocated to singlets, doublets, and triplets according to the volumetric fraction of each that had been determined by visual analysis:

$$M_i^{inlet} = V_i \cdot M_{total}^{filter} \tag{3.5}$$

where M_i^{inlet} is the mass of fluorescein entering the collector, V_i is the volumetric fraction, M_{total}^{filter} is the total mass of fluorescein collected on the filters, and the subscript i refers to singlets, doublets, and triplets.

The mass of fluorescein collected on the first stage impaction surface was also allocated among singlets, doublets, and triplets. This allocation was possible only if the doublet and triplet

collection efficiencies were known, however. If they were known, the mass of fluorescein on the first stage collection surface due to singlets could be calculated by:

$$M_s^{sfc} = M_{total}^{sfc} - \left(M_d^{inlet} \cdot E_d^1\right) - \left(M_t^{inlet} \cdot E_t^1\right) \tag{3.6}$$

where M_{total}^{sfc} is the total mass of fluorescein collected on the impaction surface, M_d^{inlet} and M_t^{inlet} are the masses of fluorescein entering the collector associated with doublets and triplets (as calculated in equation 3.5), and E_d^1 and E_t^1 refer to the first stage doublet and triplet collection efficiencies, respectively.

Finally, equation 3.7 can be used to calculate the first stage singlet collection efficiency:

$$E_s^1 = \frac{M_s^{sfc}}{M_s^{inlet}} \tag{3.7}$$

After determining the fractions of singlets, doublets, and triplets removed from the air stream by the first stage impaction surface, the mass of fluorescein entering the interstage region associated with each drop type can be calculated by:

$$M_i^{interstage} = M_i^{inlet} - \left(M_i^{inlet} \cdot E_i^1\right) \tag{3.8}$$

The interstage regions of the FROSTY and CSU 5-Stage collectors behave in a manner similar to the stage collection surfaces in that drops will be collected by the wall surfaces. These wall losses are size dependent and wall loss "efficiency" curves can be constructed to describe them. If the interstage doublet and triplet collection efficiencies are known, the mass of fluorescein due to singlets on the interstage walls can be determined from the measured wall losses with the following equation:

$$M_s^{walls} = M_{total}^{walls} - \left(M_d^{interstage} \cdot E_d^{int.1}\right) - \left(M_t^{interstage} \cdot E_t^{int.1}\right) \tag{3.9}$$

where M_{total}^{walls} is the total mass of fluorescein collected on the first interstage wall surfaces, $M_d^{interstage}$ and $M_t^{interstage}$ refer to the mass of fluorescein entering the first interstage region

associated with doublets and triplets, and $E_d^{int.1}$ and $E_t^{int.1}$ refer to the first interstage doublet and triplet collection efficiencies.

The interstage collection efficiency is then calculated with the following equation:

$$E_s = \frac{M_s^{walls}}{M_s^{interstage}} \tag{3.10}$$

By using equations such as 3.5 – 3.10, adapted for each successive stage and interstage region, this process can be repeated in order to track the mass of fluorescein partitioned between singlets, doublets and triplets through the collector. When this is done for all drop sizes, traditional collection efficiency curves can be created.

For the collection efficiency calculation at a given drop size, this procedure assumes that the collection efficiencies of the doublets and triplets are known in advance. This can be accomplished by beginning the calibration with drop sizes that have 100% collection efficiency. Doublets and triplets will then also have 100% efficiency. Subsequent efficiency calculations for smaller drop sizes can then use the previously calculated larger drop size efficiencies that correspond to doublets and triplets. Due to time and equipment constraints, however, experimental calibrations for drop sizes up to those that had 100% collection were not performed. For drop sizes in which collection efficiencies of doublets and triplets were not explicitly measured, these values were estimated from extrapolations from smaller sizes. Because of the relatively low volumetric fraction of doublets and triplets at these larger sizes, variations in the estimates of doublet and triplet collection efficiencies did not significantly affect the singlet collection efficiency calculations.

The wall loss measurements needed for this analysis were obtained in slightly different manners for each of the collectors. For the FROSTY collector, wall losses were only measured for a number of drop sizes spanning the calibration range, including 30, 28, 26, 18, 14, 8, 6, and 4 μm drops. It was noted that for the 30 through 8 μm drop sizes, when wall losses were measured,

that 95% to 99% of the fluorescein associated with the calibration drops could be recovered from the impaction surfaces and interstage walls, and very little was passing entirely through the collector. Based on those data, it was assumed that the total interstage wall losses for all drop sizes in that range could be calculated by subtracting the total mass of fluorescein collected on the three impaction surfaces from the total mass of fluorescein entering the collector. The total wall losses were then allocated to the three interstage regions based on the actual wall loss measurements. For constancy, this process was used even when actual wall loss measurements were available. The actual wall loss measurements indicated that for this size range, nearly all of the wall losses occurred in the first and second interstage regions. Therefore, for drops from 30 to 10 μm, the wall losses were partitioned between the first and second interstage regions only. The measured fraction of the wall losses that occurred in the first interstage region is plotted versus drop diameter in Figure 3.10. A second order polynomial fit through these data was then used to interpolate the losses in the first interstage region for drop diameters for which losses were not explicitly measured. Losses not allocated to the first interstage region were allotted to the second interstage region.

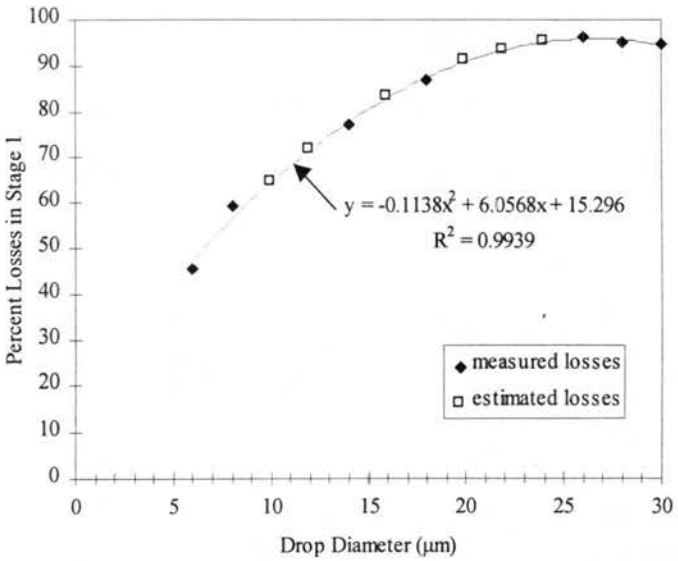

Figure 3.10 Percentage of total wall losses occurring in the first interstage region of the FROSTY collector. Solid diamonds represent values obtained from actual wall loss measurements. Open squares represent estimated values from the polynomial curve fit through the measured values.

For 8μm and smaller drop sizes, in which some fraction of drops would be expected to pass through the collector entirely and therefore not be measured, the above method for the calculation of total interstage losses was not applicable. The actual wall losses were therefore measured for the 8, 6, and 4 μm drop sizes and these measurements were used directly in the spreadsheet used to adjust the collection efficiency curves.

Wall loss measurements were made for all drop sizes during the calibration of the CSU 5-Stage collector. However, unlike the FROSTY collector, the total mass of fluorescein that was drawn into the CSU 5-Stage collector could never be entirely recovered from the impaction surfaces and interstage walls. As illustrated in Figure 3.11, a deficit of about 10% was usually experienced for drop sizes larger than 8 μm. This deficit was attributed to two factors. First of all, the removal of fluorescein from the impaction surfaces by washing with extract solution was not 100% efficient. Subsequent washing of the impaction surfaces with additional extract solution revealed that some fraction of fluorescein remained on the impaction surfaces, leading to a slight underestimation of mass on those surfaces. In addition, due to the design and orientation of the CSU 5-Stage collector, some of the interstage walls, such as the walls opposite the impaction surfaces, could not be routinely extracted. A limited number of extractions of these walls indicated that although the losses to these walls were minimal, they did exist. In addition, losses to the end walls of each of the stages were a possibility, but never directly measured. These factors also lead to a slight underestimation of fluorescein on the interstage wall surfaces. These underestimations of impaction surface measurements and wall loss measurements were assumed to account for the discrepancy. Because measurements of both the impaction surfaces and the interstage wall surfaces were considered to have a negative bias, as a first approximation, the unrecovered fraction of fluorescein was distributed proportionally to all surfaces. The reapportioned masses were then used in the spreadsheet used to correct the efficiency curves.

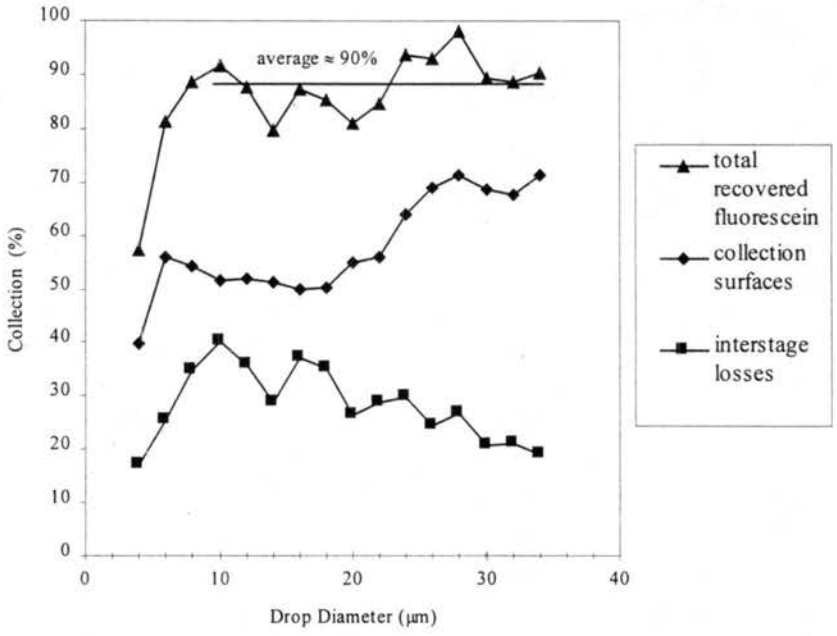

Figure 3.11 Percentage of fluorescein mass recovered from impaction surfaces and interstage wall surfaces in the CSU 5-Stage collector at each drop size. The sum of the impaction surface mass and interstage wall mass yields the total recovered fluorescein.

As with the FROSTY collector, at smaller drop sizes some fraction of drops will not be collected on any surface in the collector and will pass through the collector instead. When examining Figure 3.11, this would appear to be the case for 8, 6, and 4μm drops in which the percentage of total fluorescein recovered in the collector begins to drop rapidly. For these drop sizes, apportioning the entire unrecovered mass to collector surfaces was not appropriate. To correct for the measuring bias described above for these drop sizes, it was assumed that the magnitude of underestimation of fluorescein on the impaction and wall surfaces as observed at the larger drop sizes was also valid at smaller drop sizes. The average underestimation for 10 μm and larger drops was calculated to be 10%. Therefore, the values of measured fluorescein mass on all collector surfaces for 8, 6, and 4 μm drops were increased by 10%. Again, these reapportioned masses were used as input to the efficiency correction spreadsheet.

4 FROSTY Supercooled Cloud Collector Calibration

4.1 Numerical Results

As previously discussed, a representative two-dimensional layer of the FROSTY collector was selected for modeling. This horizontal layer is symmetric about the centerline of the collector, so only one half of the layer was modeled. This was accomplished by employing a symmetry boundary condition at the centerline. The hatched area seen in the top view of the collector in Figure 4.1 represents the portion of the flow domain modeled. This flow domain was discretized into control volumes with the structured mesh depicted in Figure 4.2.

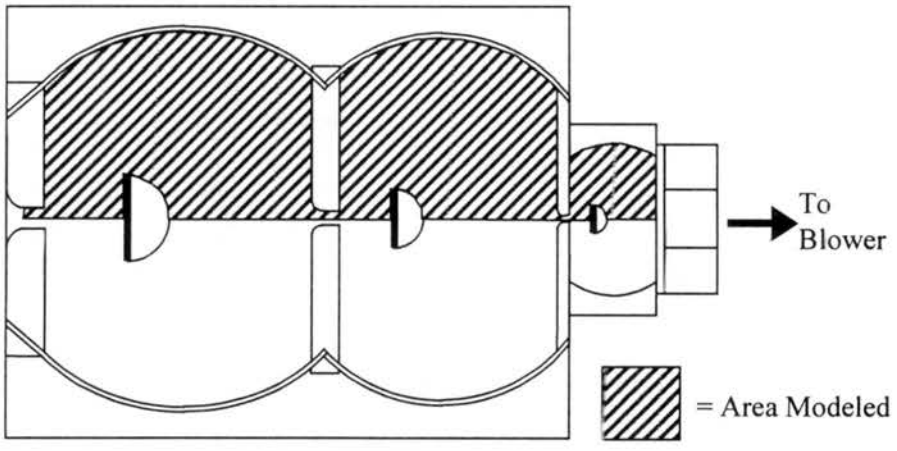

Figure 4.1 Two-dimensional, symmetric region of the FROSTY supercooled cloud collector selected for numerical analysis.

The first stage jet inlet boundary condition has an imposed velocity of 5.75 m/s in the positive x-direction, which corresponds to a flow rate of 1500 l/min through the collector. An outlet boundary condition is specified for the collector exit region located downstream of the third stage collection surface. A listing of the FLUENT files generated during the modeling of the FROSTY supercooled cloud collector can be found in Appendix E.

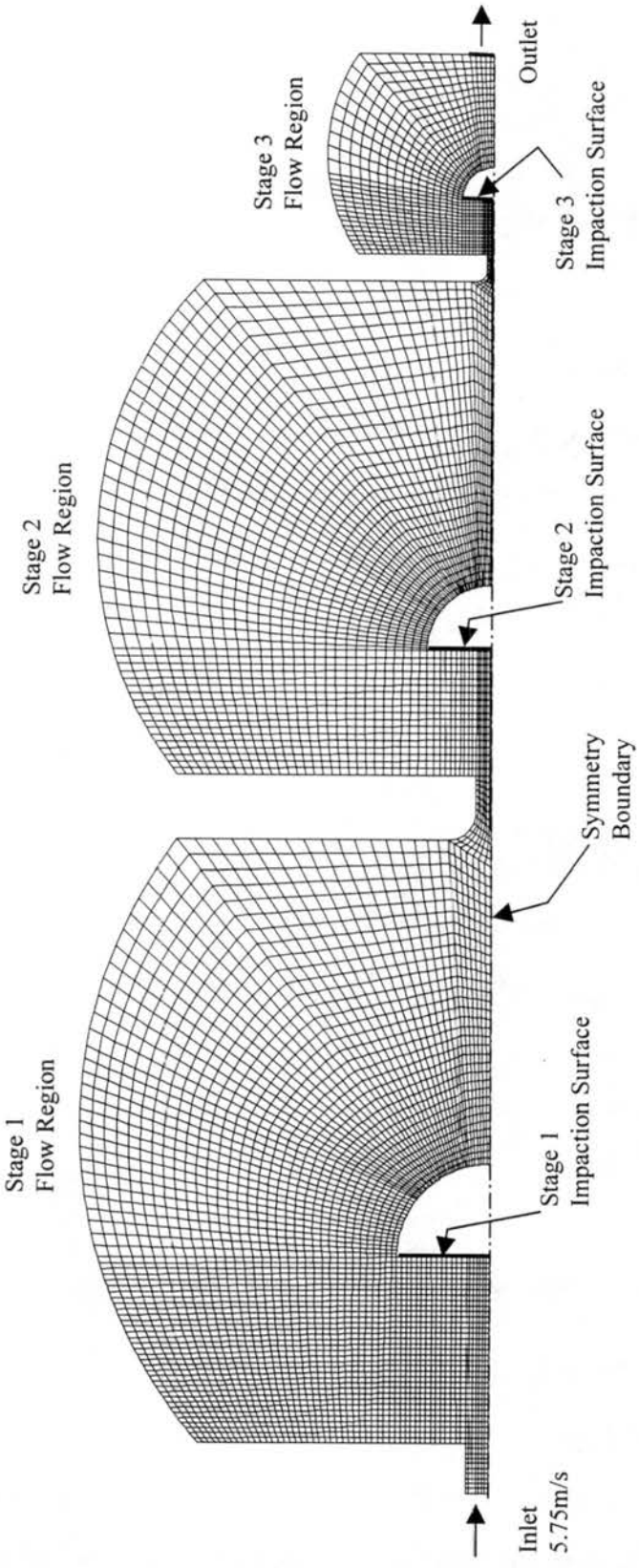

Figure 4.2 Numerical structured grid used to discretize the flow domain of the FROSTY supercooled cloud collector.

4.1.2 Description of air flow patterns

Steady state air flow patterns through the FROSTY collector generated by way of numerical simulation at laboratory conditions can be seen in Figures 4.3-4.5. The arrows in these figures represent velocities at the control volume centers as vectors, indicating both the direction and speed of the air flow. To improve clarity, velocity vectors are displayed at every other control volume for the first stage and every control volume in the second and third stages. Velocities in the first stage are in the range of 0 to 6.5 m/s. The air enters the collector at the inlet in the positive x-direction with the prescribed boundary condition velocity of 5.75 m/s. As the flow nears the first stage impaction surface, it is deflected 90 degrees to the left. The flow then travels toward the curved wall of the first stage. When the flow reaches the wall, it divides, with the main flow moving along the wall toward the second stage and through the second stage jet plate. A fraction of the flow is deflected in the negative x-direction, creating a weak cyclonic recirculation pattern in front of the impaction surface. Similarly, near the entrance to the second stage, a fraction of the flow is diverted along the line of symmetry in the negative x-direction. This creates a large anti-cyclonic circulation, with an area of near stagnation at its center, behind the impaction surface.

The second and third stages have similar air flow patterns. The second stage velocities range from 0 to 9.4 m/s. The jet velocities in the second stage are higher than the first stage by design in order to provide collection of smaller drops. Recirculation zones with areas of near stagnation develop upstream and downstream of the impaction surface, as in the first stage. Third stage velocities are higher yet, in order to collect the smallest drop fraction. The velocity range is from 0 to 24.2 m/s, with the highest velocity in the jet region. Due to these considerably higher velocities, the recirculation zones apparent in the first two stages are again present, and are much more pronounced. After the jet impinges on the third stage impaction surface, it is deflected with a component in the negative x-direction, creating a strong circulation immediately upstream of the impaction surface. Finally, the air exits the collector through the outlet in the third stage.

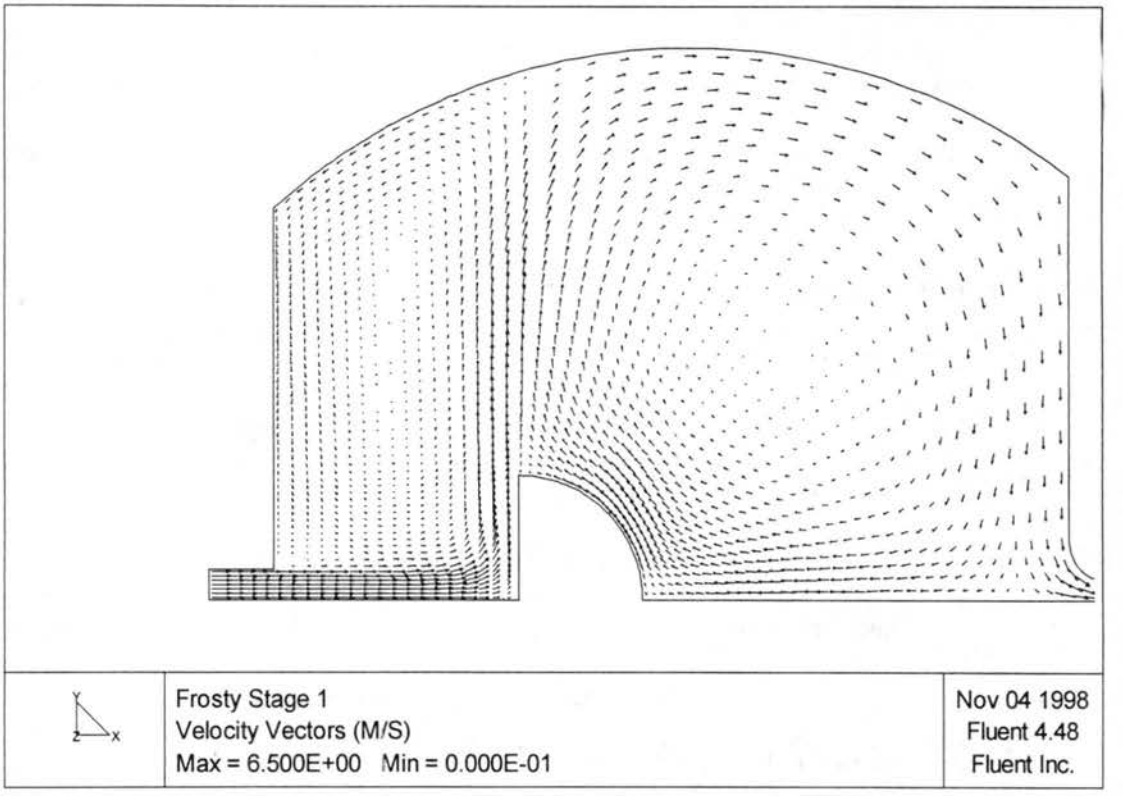

Figure 4.3 **The FROSTY collector stage 1 continuous phase flow field.**

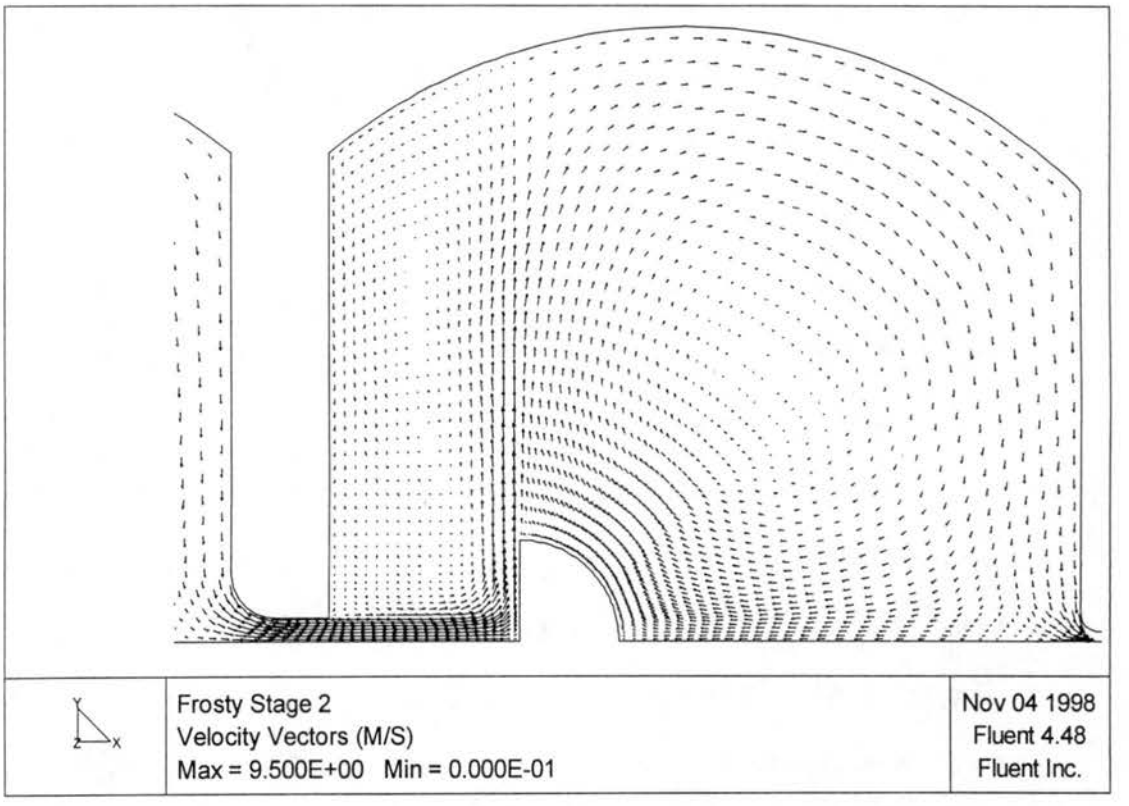

Figure 4.4 **The FROSTY collector stage 2 continuous phase flow field.**

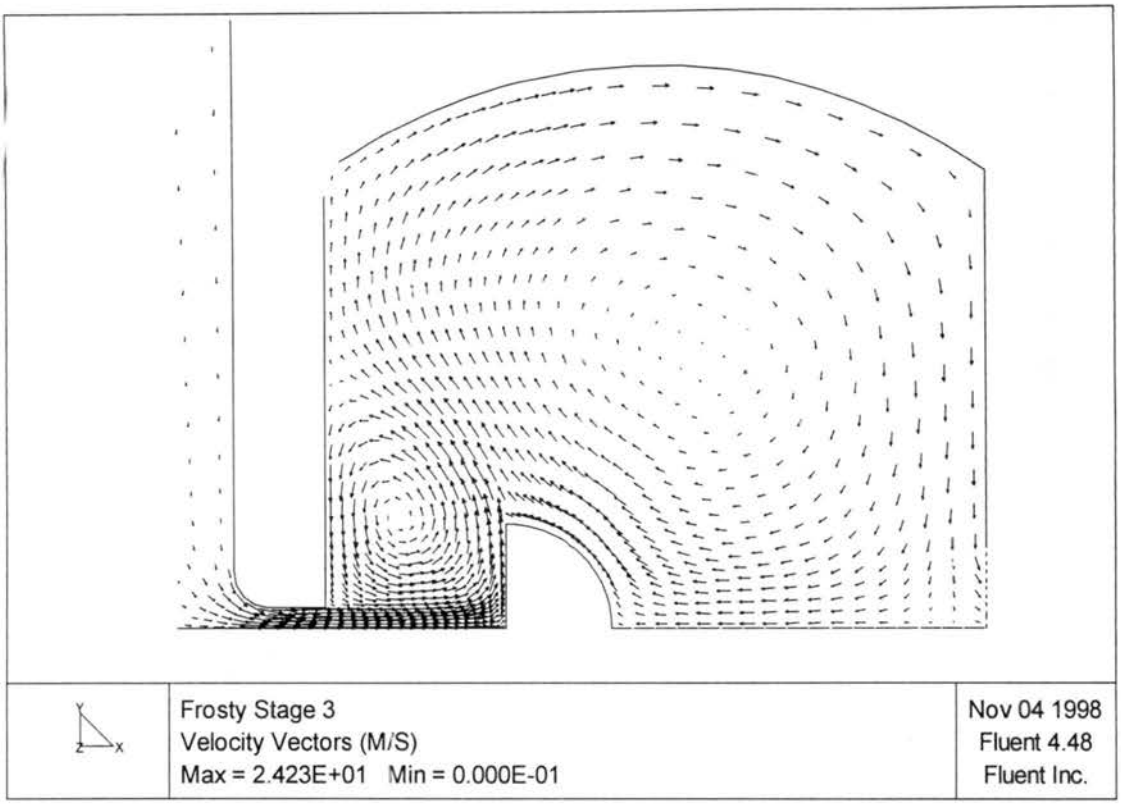

Figure 4.5 The FROSTY collector stage 3 continuous phase flow field.

4.1.3 Drop trajectories

This continuous phase flow solution was then used as the basis for the calculation of drop trajectories. Drops injected with an initial velocity of 5.75 m/s from 100 discrete locations distributed along the first stage inlet entered the continuous phase flow solution and interacted with the flow as dictated by the solution to the drop's equation of motion. As previously described, two options were available for the calculation of drop trajectories. Trajectories could be based on the average continuous phase velocity field, or could optionally include the effects of instantaneous velocity fluctuations on drop motion.

Figure 4.6 shows sample drop trajectories through the FROSTY collector for the case in which only the average continuous phase velocities were included in the drop equation of motion. In this figure, ten representative mean trajectories for 10 μm drops are shown. The drop paths are quite smooth as the 10 μm drops travel with the air flow past the first stage impaction surface,

along the first interstage wall surfaces and into the second stage. When passing through the second stage jet, the drops are focused into a narrow range near the jet centerline. The drops again remain with the air flow past the second stage impaction surface and through the second stage without any collection. The drops are then further focused toward the jet centerline as they pass through the third stage jet. Finally, all of the 10 μm trajectories are terminated when they intersect the third stage impaction surface.

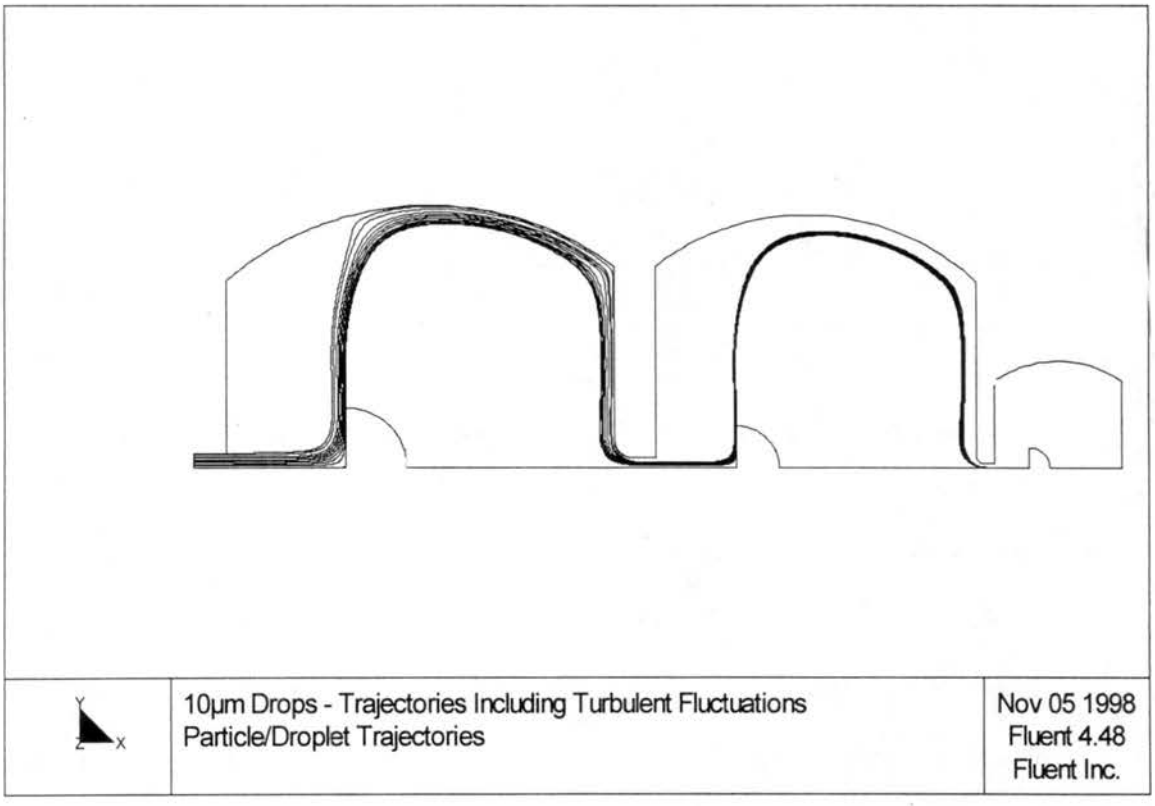

Figure 4.6 10 μm drop sample trajectories based on the mean continuous phase flow field of the FROSTY collector.

In contrast to the uniform trajectories generated when only the average continuous phase velocities are considered, Figure 4.7 shows sample trajectories which include instantaneous velocity fluctuations in the drop equation of motion. These ten sample trajectories are for 10 μm drops. The influence of the instantaneous velocity component is apparent as drop paths that are noticeably more erratic, with individual drops abruptly changing directions at times. The forcing

of drops from their mean trajectories by instantaneous fluctuations results in a tendency for drops to become influenced by the continuous phase recirculation zones upstream or downstream of the impaction surfaces. Once a drop enters an area of recirculation, it may remain there for a number of revolutions before escaping. Another of the effects of the instantaneous velocity fluctuations on drop motion is a change in the droplet collection patterns through the collector. The inclusion of turbulent fluctuations causes some large drops to miss the impaction surfaces and causes small drops to hit the surface. In addition, as can be seen in Figure 4.7, wall losses are dramatically increased when trajectories include instantaneous velocity fluctuations.

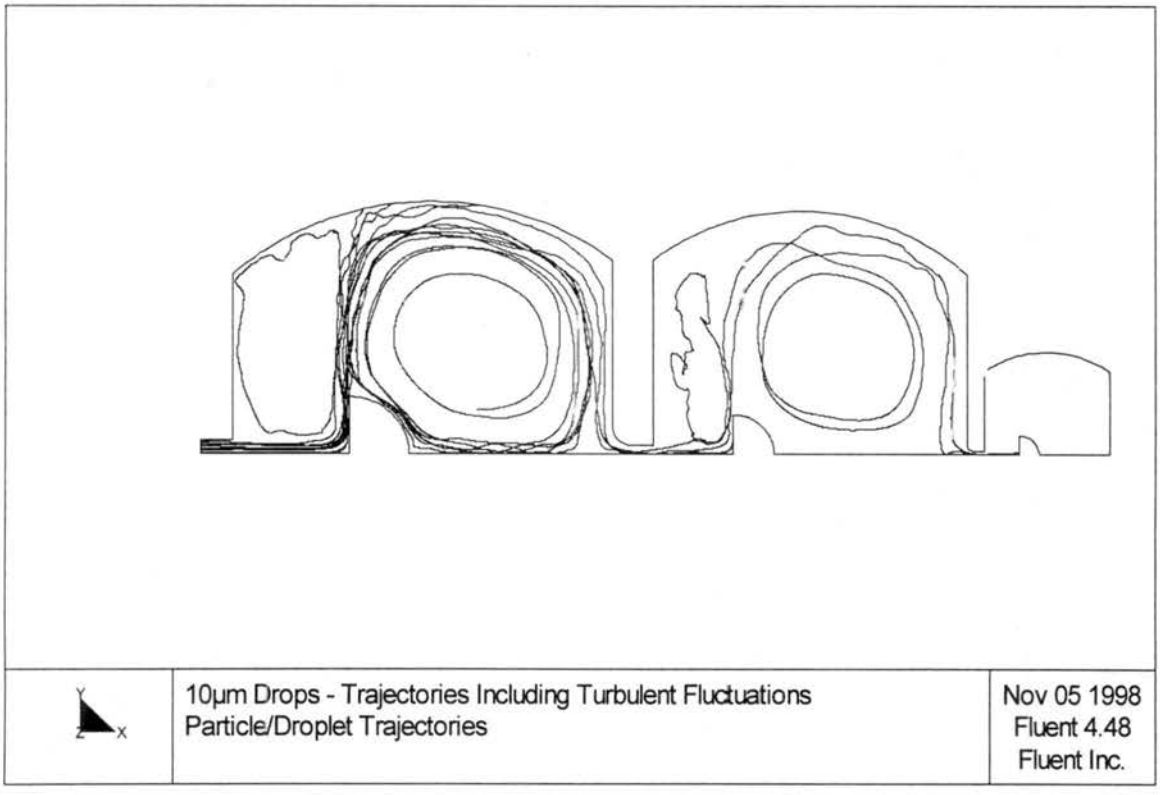

Figure 4.7 10 µm drop sample trajectories that include the effects of continuous phase velocity fluctuations.

4.1.4 Efficiency curves

Figure 4.8 shows efficiency curves for trajectories based on mean continuous phase velocities. Curves for all three stages of the FROSTY collector are included in this figure. For

this case, the efficiency curves are fairly steep, nearing the step function shape of an ideal efficiency curve. This indicates that a good distinction is made in each stage between drops that are collected and those that are not collected. The 50% cut diameters are 21.5 μm for the first stage, approximately 12 μm for the second stage, and approximately 4.5 μm for the third stage. Again, these 50% cut diameters are for numerical modeling at laboratory conditions, and are therefore slightly higher than the design 50% cut diameters for the collection of water drops at 3000 meters.

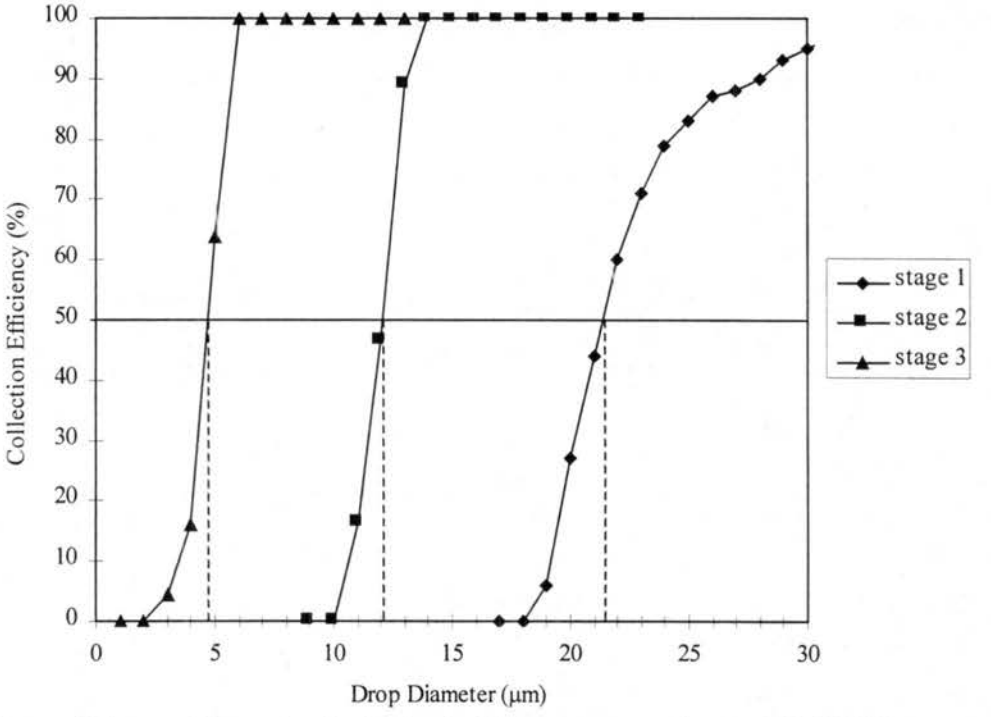

Figure 4.8 Numerically derived efficiency curves for the FROSTY collector assuming trajectories that are based on the mean continuous phase velocity field. Stage 50% cut diameters are approximately 21.5, 12, and 4.5 μm.

The efficiency curves for drop trajectories that include the effects of turbulent velocity fluctuations on drop motion can be seen in Figure 4.9. The most notable difference between this set of efficiency curves and the curves based on trajectories that do not include turbulent fluctuations, is the slope of the curves. In this case, the efficiency curves are much less steep, further removed from the ideal efficiency curve shape. Some drops larger than the 50% cut diameter, which would ideally be collected with 100% efficiency are not collected, while some

drops smaller than the 50% cut diameter are collected when they would ideally not be. This leads to more overlap in the populations of drops collected on each of the stages. Despite the change in the slope of the efficiency curves that occurs when velocity fluctuations are included, the 50% cut diameters remain nearly the same. The 50% cut diameters for this case are 20.5 μm for the first stage, 13.5 μm for the second stage, and 5 μm for the third stage. Therefore, the consequence of including the instantaneous velocity fluctuations in the trajectory calculations is to decrease the slope of the efficiency curves while keeping the 50% cut diameters essentially unchanged.

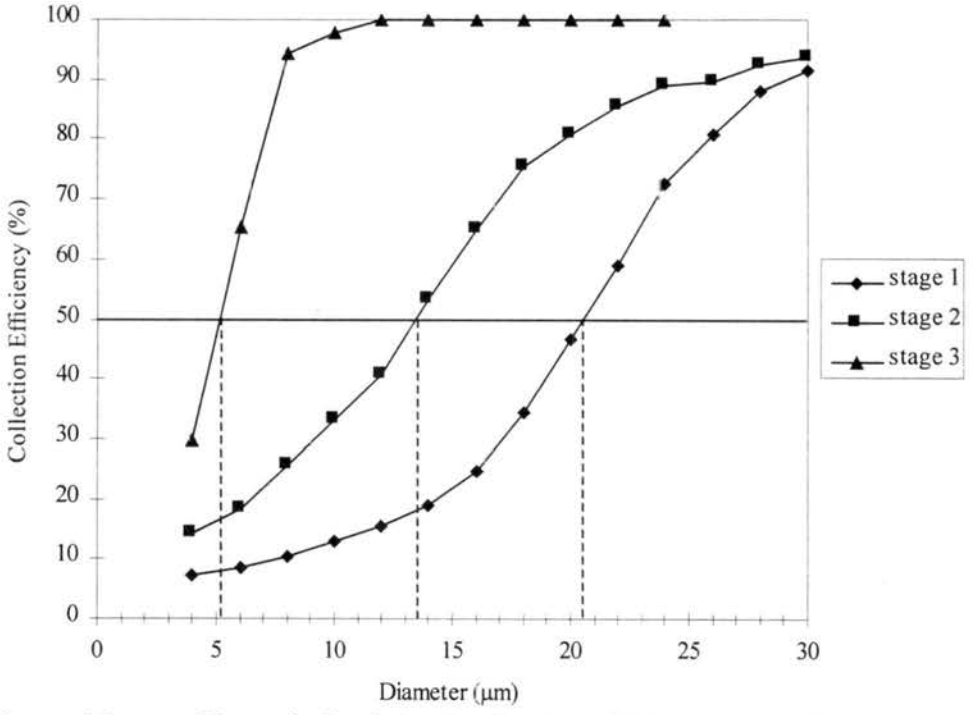

Figure 4.9 Numerically derived collection efficiency curves for the FROSTY collector assuming trajectories that include turbulent velocity fluctuations. Stage 50% cut diameters are approximately 20.5, 13.5, and 5 μm.

4.2 Experimental Results

Experimental collection efficiency curves for the three stages of the FROSTY collector, corrected only for the presence of multiplets, can be seen in Figure 4.10. The 95% confidence limits discussed in section 3.2.5 are presented as error bars at each point. These curves represent the actual percentage of oleic acid drops of each diameter that were collected on each of the three

stages during operation at laboratory conditions. The first stage curve has the typical S-shape, in which collection efficiency increases with drop diameter. The second and third stages are not S-shaped, but instead have efficiencies that increase with drop diameter to a peak collection efficiency, and then decrease. The decrease in collection efficiency is due to the presence of previous stages and wall losses. Large drops that are collected by the first stage or lost to the first stage walls are unavailable for collection by the second and third stages, resulting in an apparent decrease in efficiency. Although there is overlap between each of the stages, these curves reveal that the FROSTY collector does collect three distinct populations of drop sizes on the three collection surfaces. For a listing of data obtained during the experimental calibration of the FROSTY collector, see Appendix B.

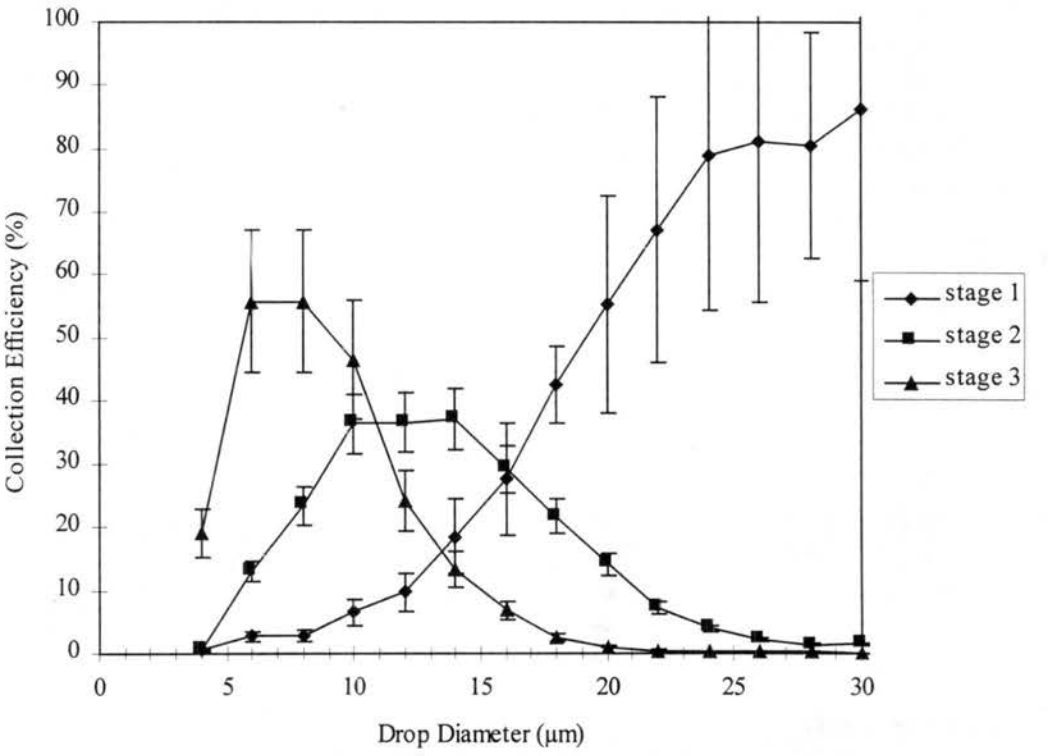

Figure 4.10 Experimentally derived collection efficiency curves for the FROSTY collector corrected to account for the presence of multiplets. Error bars reprsent 95% confidence limits.

In order to present the efficiency curves in a more traditional manner, which allows the 50% cut diameters to be reported, corrections for wall losses and previous stage collection were

made. Efficiency curves for the experimental calibration, after correction for wall losses, previous stage collection, and multiplets, can be seen in Figure 4.11. Error bars at each point represent 95% confidence limits. While the first stage 95% confidence limits in Figure 4.11 are identical to those in Figure 4.10, the second and third stage 95% confidence limits account for uncertainty in all of the measurements required to calculate the corrected efficiency curves. The 50% cut diameter for the first stage is slightly greater than 19 μm, nearly 11.5 μm for the second stage, and just over 5 μm for the third stage. Truncation of the second and third stage curves at larger drop sizes is explained in section 3.4.2.

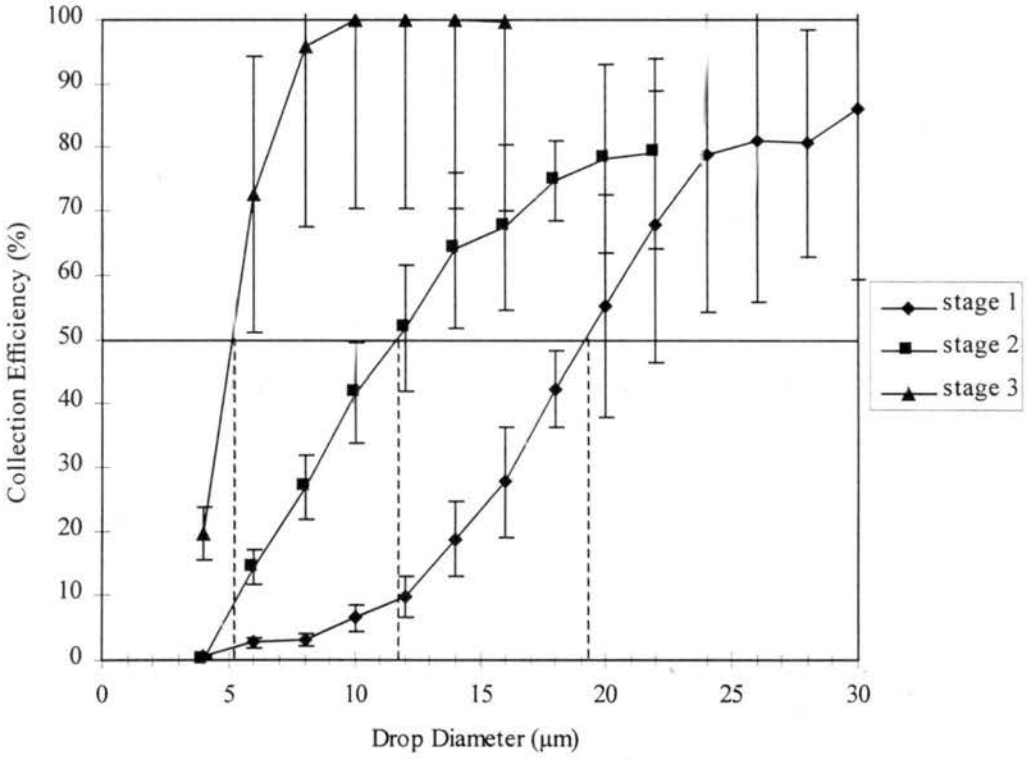

Figure 4.11 Experimentally derived collection efficiency curves for the FROSTY collector corrected for the presence of multiplets, previous stage collection, and wall losses. Stage 50% cut diameters are approximately 19, 11.5, and 5 μm. Error bars reprsent 95% confidence limits.

Interstage losses in the collector were calculated by subtracting the total mass of fluorescein collected on all of the impaction surfaces from the total mass of fluorescein entering the collector for drops larger than 10μm and apportioning these total losses based on actual wall

losses measured at selected sizes. Actual loss measurements were used for drops 4, 6, and 8 μm in diameter. These interstage wall losses, adjusted to account for the presence of multiplets, are illustrated in Figure 4.12. The bulk of the interstage wall losses occur in the first interstage region. Total interstage losses peak at about 16 μm with nearly 40% of incoming drops lost to the wall surfaces.

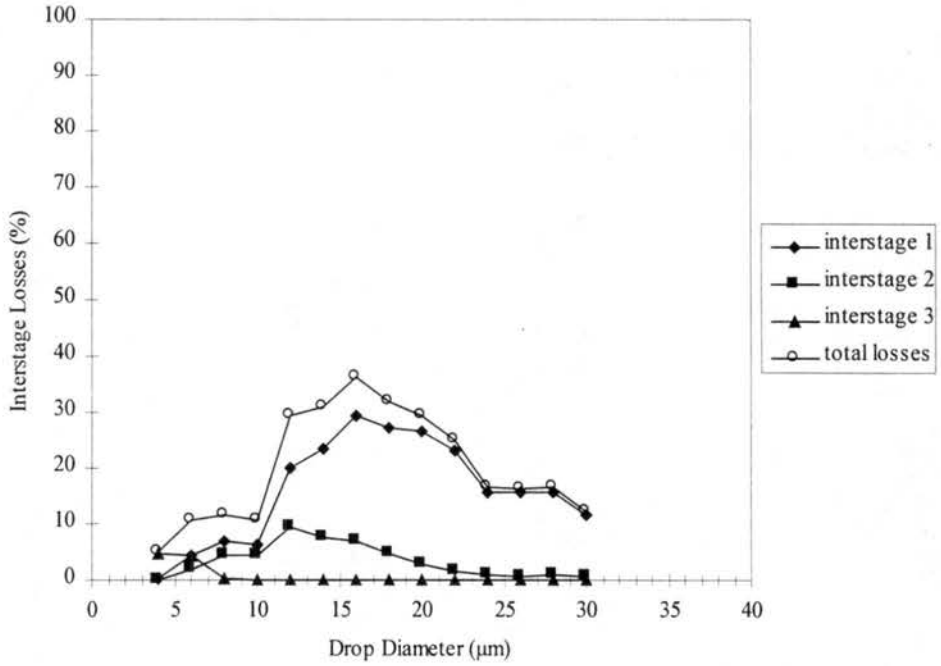

Figure 4.12 Experimentally determined interstage wall losses for the FROSTY collector.

4.3 Discussion

4.3.1 Comparison of numerical and experimental results

Comparisons between the numerically and experimentally derived efficiency curves are shown in Figures 4.13 - 4.15. These plots were generated by overlaying the curves expressed in Figures 4.8, 4.9, and 4.11. Included in these figures are the numerically derived curves for trajectories including and not including the effects of instantaneous velocity fluctuations. Figure 4.13 shows these curves for the first stage. Both numerical curves simulate quite well the efficiency curve for larger size drops and fairly accurately predict the 50% cut diameter.

However, it is apparent that the numerical curve based on average velocities is too steep and agrees poorly with experimental observations at smaller sizes. The numerical curve that includes dispersed phase turbulence more accurately reflects the actual shape of the efficiency curve, as derived experimentally. However, collection at smaller drop sizes is over predicted, a trend that will be apparent in all of the numerical modeling.

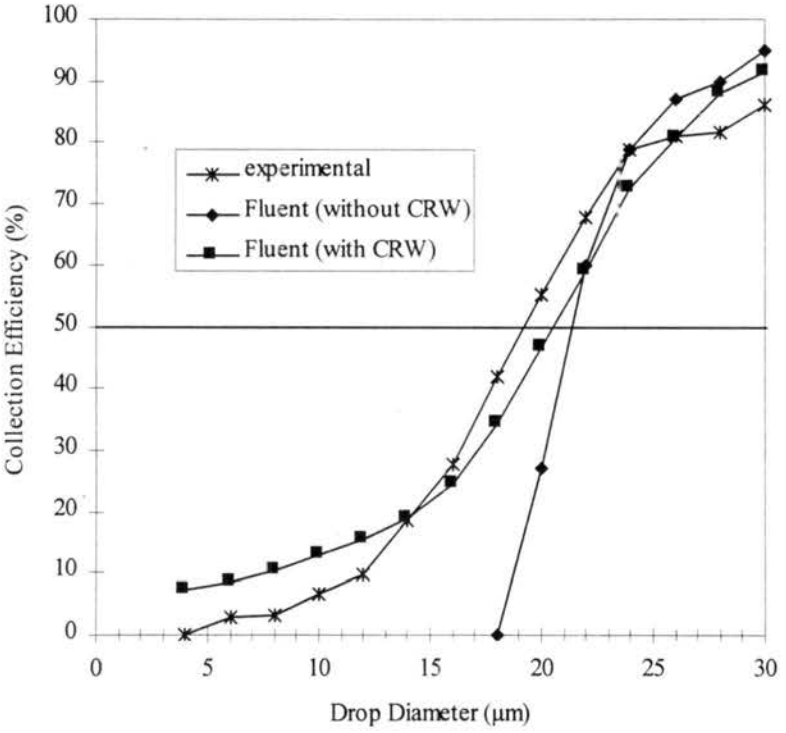

Figure 4.13 Stage 1 comparison between numerical and experimental efficiency curves for the FROSTY collector. The two numerical efficiency curves are based on drop trajectories that include (solid squares) and do not include (solid diamonds) the effects of turbulent velocity fluctuations.

The second and third stage comparisons in Figures 4.14 and 4.15 are quite similar to the first stage, with both numerical curves showing fairly good agreement with the 50% cut diameter. However, the numerical curves including dispersed phase turbulence again provide a better representation of the overall shape of the efficiency curves, indicating that turbulent fluctuations must be considered explicitly in the dispersed phase trajectory simulations for the accurate description of drop trajectories through the FROSTY collector.

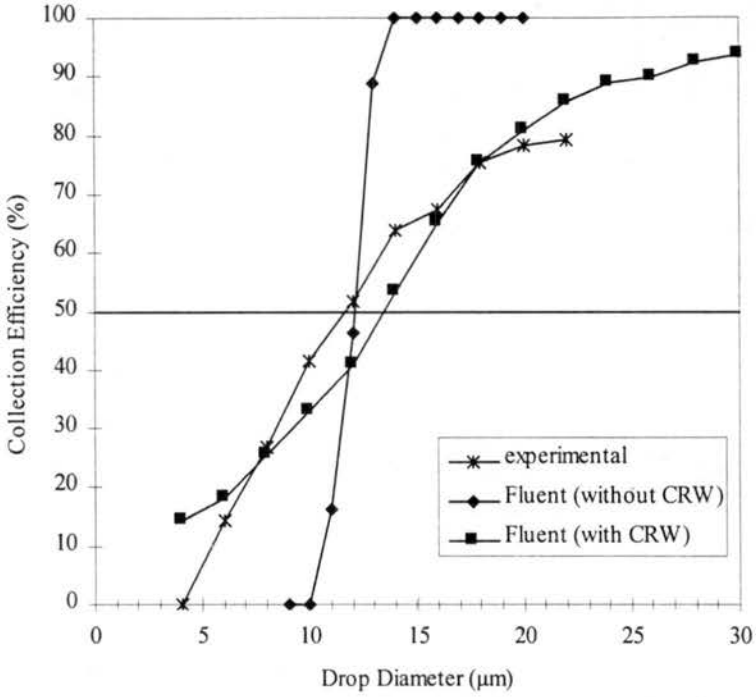

Figure 4.14 Stage 2 comparison between numerical and experimental efficiency curves for the FROSTY collector. The two numerical efficiency curves are based on drop trajectories that include (solid squares) and do not include (solid diamonds) the effects of turbulent velocity fluctuations.

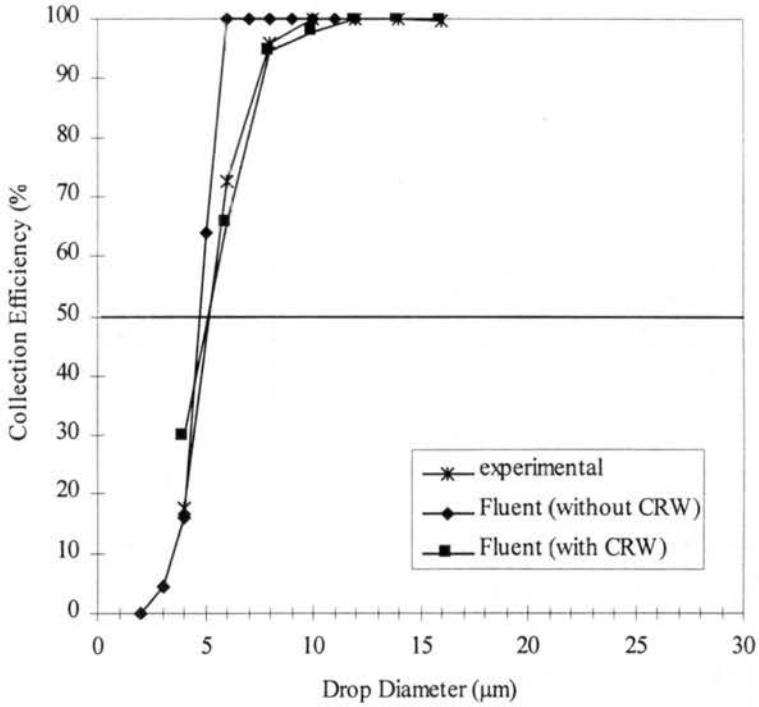

Figure 4.15 Stage 3 comparison between numerical and experimental efficiency curves for the FROSTY collector. The two numerical efficiency curves are based on drop trajectories that include (solid squares) and do not include (solid diamonds) the effects of continuous phase turbulent velocity fluctuations.

One area in which comparison of the numerical and experimental data is not as favorable is the percentage of drops lost to the interstage walls of the collector. Figure 4.16 illustrates this point by contrasting the numerically and experimentally derived total wall loss curves. The experimentally determined wall losses increase with increasing drop size, peak at about 16 μm, and then decrease. Wall losses in the numerical simulations when drop trajectories are based on the mean continuous phase agree with experimental values at larger drop sizes, but then drop to nearly zero for drop sizes between 10 and 16 μm before slightly increasing again at small drop sizes. Losses in the numerical simulations in which trajectories include turbulent fluctuations are in relatively good agreement with the experimental losses for drop sizes larger than about 16 μm. However, the losses for these numerical simulations steadily increase with decreasing drop size, resulting in a large discrepancy at small drop sizes.

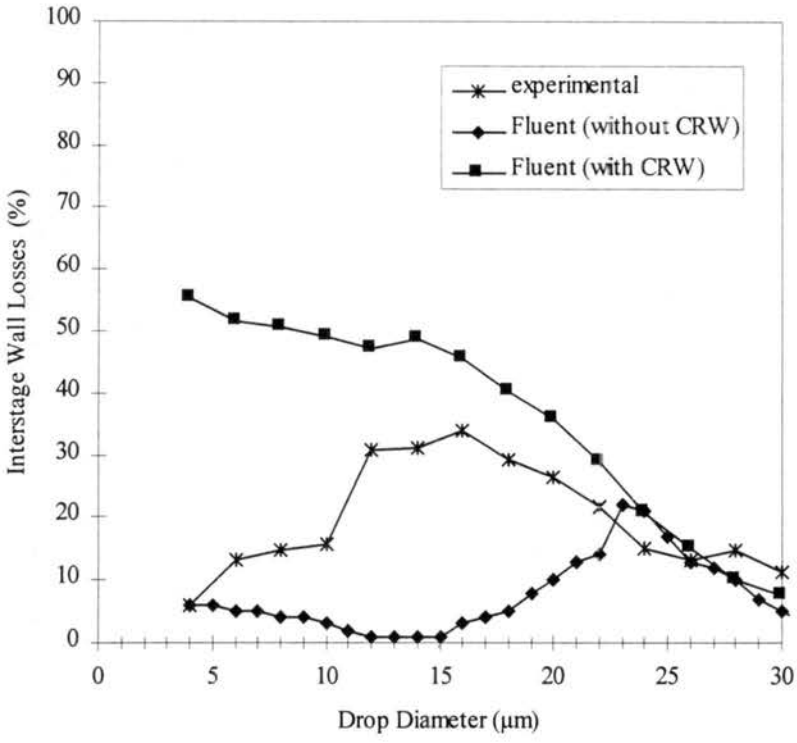

Figure 4.16 Comparison between numerical and experimental interstage wall losses for the FROSTY collector. Losses are expressed as a percentage of drops intoduced into the collector. The two numerical loss curves are based on drop trajectories that include (solid squares) and do not include (solid diamonds) the effects of continuous phase turbulent velocity fluctuations.

4.3.2 The integral time scale

The experimental calibrations of the FROSTY collector revealed that preliminary numerical drop trajectory simulations that included the effects of continuous phase velocity fluctuations using default parameters produced somewhat "flat" collection efficiency curves, as well as excessive losses of drops to the interstage walls. However, these results were in better agreement with experimental data than the numerical trajectory simulations that did not include turbulent fluctuations. These trajectories produced overly steep efficiency curves and too few drop losses to the interstage walls. The experimentally determined wall and impaction surface drop collection behavior fell between these two modeling extremes. It appeared that the inclusion of some degree of turbulent fluctuation in the trajectory calculations is necessary to accurately define drop trajectories, but that these turbulence effects may be overemphasized in the model.

Although the magnitude of the turbulent velocity fluctuations derived from the Reynolds stresses could not be modified, the duration of drop interaction with those velocity fluctuations could be altered. To determine if better agreement between the numerical and experimental results was possible, the effects of adjustments made to the fluid Lagrangian integral time scale were investigated. The Lagrangian integral time scale, T_L, defines the lifetimes of turbulent eddies in the continuous phase solution domain and is given by the following equation:

$$T_L = \alpha \frac{k}{\varepsilon} \tag{4.1}$$

where k is the continuous phase turbulent kinetic energy, ε is the continuous phase turbulent dissipation rate, and α is a constant with default values of 0.15 for the k-ε turbulence model and 0.30 for the RSM.

If the lifetime of a turbulent eddy is reduced, a drop will interact with the velocity fluctuation that defines that eddy for a shorter duration before progressing to the next eddy. Therefore, a drop will not be subject to a velocity fluctuation in any one given direction long enough to significantly alter its trajectory before undergoing a fluctuation in another direction.

This results in trajectories that deviate less from the paths defined by the mean continuous phase flow field. In the extreme, if T_L is set to zero, drops do not interact with velocity fluctuations for any time, and trajectories are identical to mean-velocity based trajectories. As the trajectories approach those based on mean continuous phase velocities as T_L is decreased, the resulting collection efficiency curves become steeper and wall losses decrease.

A reduction in T_L was accomplished by reducing α in equation 4.1 from the default value of 0.3. After investigating several values, $\alpha = 0.09$ offered the best fit to experimental data by providing a compromise between trajectories that include no velocity fluctuations and those that do include velocity fluctuations subject to the default integral time scale. All of the efficiency curves from numerical trajectory simulations that included velocity fluctuations displayed previously in this chapter assume $\alpha = 0.09$. As was noted in section 4.3.1, the wall losses are still over predicted with the decreased α, especially at smaller drop sizes. However, decreasing the wall losses by further reductions in the integral time scale resulted in excessively steep efficiency curves that no longer matched the experimental curves. Figure 4.17 illustrates the difference

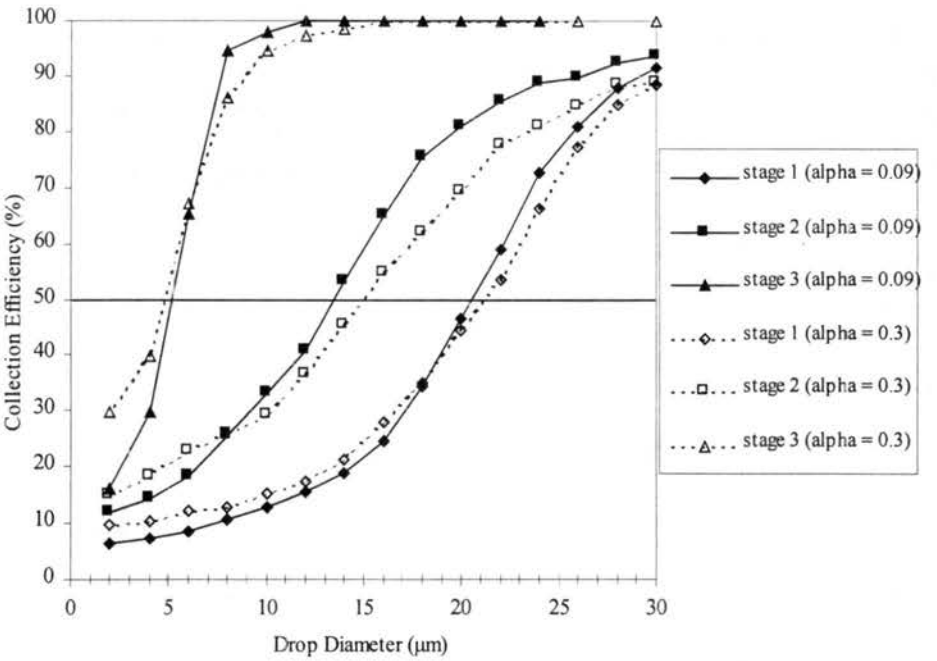

Figure 4.17 Efficiency curves for the FROSTY collector with numerical trajectory simulations that assume $\alpha = 0.09$ and $\alpha = 0.3$.

between efficiency curves with $\alpha = 0.09$ and $\alpha = 0.3$ for the FROSTY collector. Although the changes are not drastic, the effect of lowering α to 0.09 is to sharpen the efficiency curves while lowering wall losses to better reflect the experimental observations. It was hoped that this reduced value of α would be appropriate for numerical trajectory simulations of the CSU 5-Stage collector as well.

4.3.3 Calibration at design conditions

The experimental calibration of the FROSTY collector was conducted in laboratory conditions at the Department of Atmospheric Science Cloud Simulation and Aerosol Laboratory (Simlab) located at approximately 1500 m elevation on the campus of Colorado State University. Although the experimental calibration was performed under these conditions, the FROSTY collector was designed to operate in winter conditions at 3000 m elevation. In addition, the density of the calibration drops ($\rho = 0.9$ g/cm^3) was slightly lower than the density of water. To estimate the effects these changes would have on the FROSTY collector's collection characteristics, model simulations at design conditions were performed. The numerical simulations included the effects of turbulent fluctuations on dispersed phase trajectories with $\alpha = 0.09$. The design conditions (3000 m, -4° C) were represented by a continuous phase density of 0.91 kg/m^3 and viscosity of 1.69×10^{-5} Ns/m^2, and a dispersed phase density of 1 g/cm^3. A comparison between the collection efficiency curves at design conditions and those displayed previously at Simlab condition is provided in Figure 4.18. The decrease in the continuous phase density and viscosity from Simlab to design conditions both tend to shift the collection efficiency curves to smaller drop diameters. This effect was amplified by the increase in dispersed phase density from the calibration value ($\rho = 0.9$ g/cm^3) to the density of water, which also tends to shift the efficiency curves to lower drop sizes. The first, second, and third stage 50% cut diameters decreased by 2, 1, and 0.5 μm, respectively.

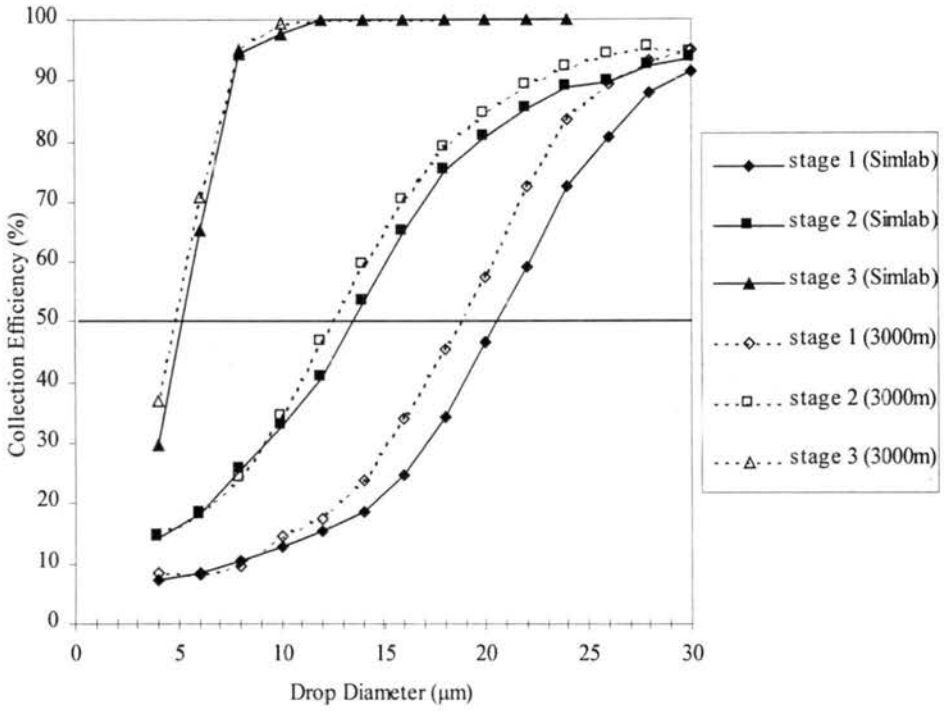

Figure 4.18 Comparison of collection efficiency curves based on numerical trajectory simulations at laboratry conditions and design conditions for the FROSTY collector. Trajectory simulations included the effects of continuous phase turbulent velocity fluctuations with $\alpha = 0.09$ for both cases.

4.3.4 Populations of drops expected on each surface for typical ambient cloud drop size distributions

The objective for the calibration of the FROSTY supercooled cloudwater collector described in the preceding chapters was to provide information that can be used to characterize the populations of cloud drops that are collected on each of the three impaction surfaces during operation. The experimentally derived collection efficiency curves presented in Figure 4.10, which were adjusted to account for the influence of multiplets, can be used in conjunction with ambient cloud drop distributions to provide size distributions that describe the populations of drops collected on each stage of the collector. Because the calibration procedure involved the use of oleic acid drops, the experimental efficiency curves in Figure 4.10 must be modified to make

them applicable to the collection of liquid water drops. This is accomplished by transforming the calibration drop diameters into aerodynamic diameters using the following relation:

$$\sqrt{\rho_A C_{D_A} D_A} = \sqrt{\rho_p C_{D_p} D_p} \tag{4.2}$$

where ρ is density, C_D is the Cunningham slip correction factor (neglected in this work due to the large diameters involved), D is diameter, and the subscripts A and p refer to the aerodynamic equivalent and actual drop, respectively. Because oleic acid is less dense than water, the resulting aerodynamic diameters are smaller than the original diameters by about 2 μm at larger drop sizes and 0.2 μm at smaller drop sizes. This transformation shifts the collection efficiency curves slightly toward smaller diameters.

Two representative cloud drop distributions were selected to simulate two different ambient sampling environments. These ambient distributions, depicted as volume distributions in the top panels in Figure 4.19, feature 12.6 and 17.7 μm volume mean diameters to represent sampling periods in which drop distributions are weighted toward smaller or larger sizes. The ambient distributions report the number of cloud drops per cubic centimeter of air in 13 discrete bins spanning the range of drop sizes. The midpoint diameters of these bins did not exactly match the diameters at which calibrations were performed, however. To derive collection efficiencies at the bin midpoints, linear interpolation between adjacent known calibration points was performed. The ambient number concentration at each bin midpoint diameter was then multiplied by the interpolated experimental collection efficiencies for each stage to calculate the number of cloud drops in each bin that are collected on each stage.

The resulting number distributions of collected drops were multiplied by the bin average drop volume to generate volume distributions. The volume distributions of cloud drops collected by each stage are provided in the panels directly below the associated ambient distribution in Figure 4.19. The panels in the left column correspond to the 12.6 μm volume average mean diameter ambient distribution while the panels in the right column correspond to the 17.7 μm

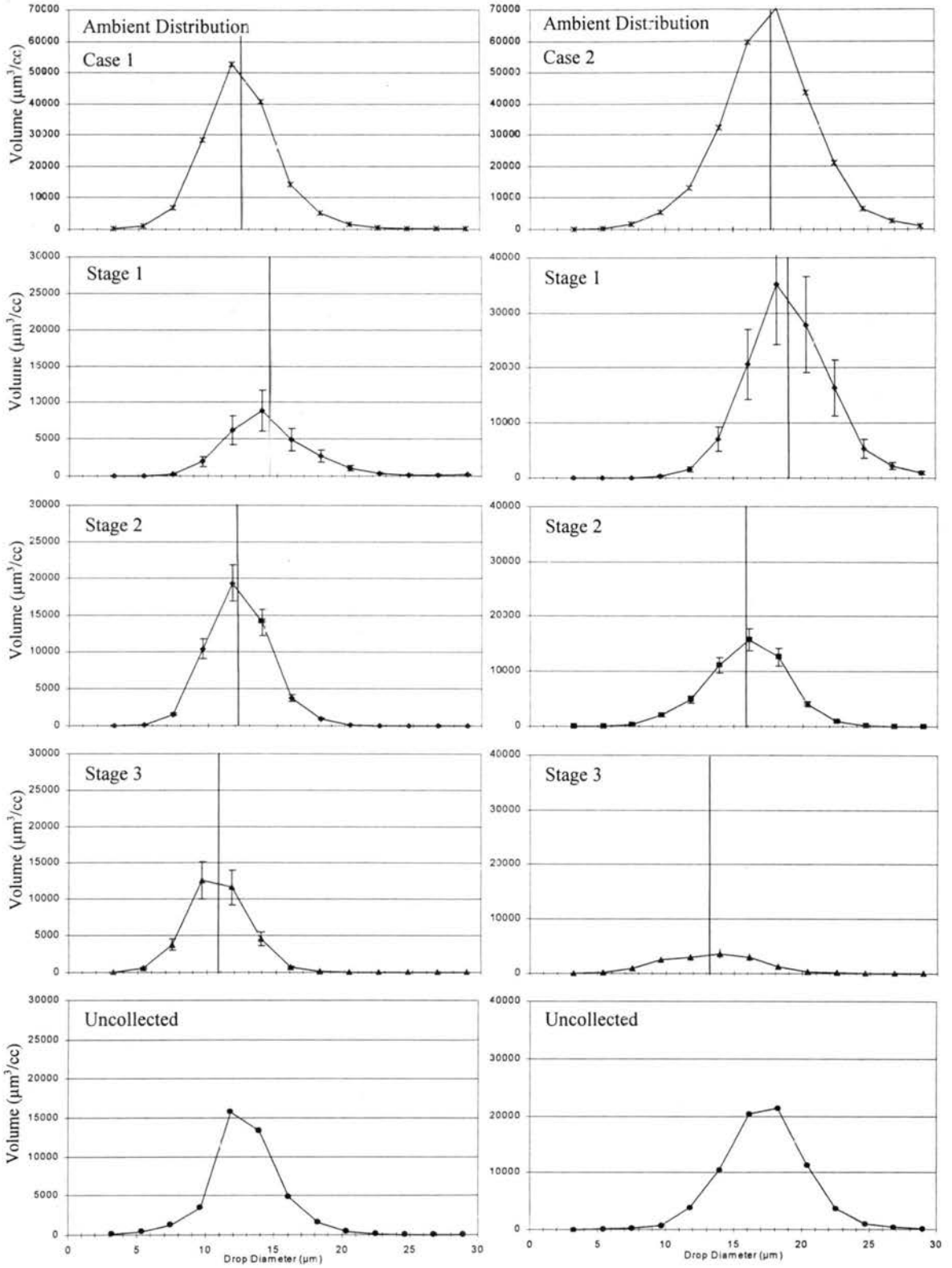

Figure 4.19 Volume distributions showing the ambient, collected, and uncollected drop populations for two cases for the FROSTY supercooled cloud collector. Volume weighted mean diameters indicated by the vertical lines for the first, second, and third stages are 14.4, 12.3, and 10.8 µm for case 1 and 19.1, 15.9, and 13.3 µm for case 2. Note the change in the y-axis scale between panels.

mean volume diameter ambient distribution. Note the change in scale of the y-axis between panels. The vertical lines in each panel indicate the volume weighted average diameter for each distribution of collected drops. If the FROSTY collector were used to sample a cloud with the 12.6 μm volume mean diameter ambient distribution, the volume weighted mean diameters of the collected drops would be 14.5 μm, 12.3 μm, and 10.8 μm for the first, second, and third stages, respectively. Sampling of the 17.7 μm volume mean diameter ambient distribution would produce populations of collected drops with volume weighted mean diameters of 19.1, 15.9, and 13.3 μm for the first, second, and third stages respectively. The last row of panels depicts the population of cloud drops that would be lost to the interstage wall regions and therefore remain unsampled. These results indicate that the FROSTY collector is capable of providing three distinct size fractions of cloudwater samples for chemical analysis.

5 CSU 5-Stage Cloud Collector Calibration

5.1 Numerical Results

The two-dimensional cross sectional area of the CSU 5-Stage cloud collector was discretized with the structured mesh seen in Figure 5.1. Because the CSU 5-Stage collector is oriented at a 45° angle with respect to the ground during operation, gravity can influence the motion of drops in the two dimensional plane under consideration. Therefore, gravity terms were included in the positive x-direction and the negative y-direction in the equations describing drop motion. Figure 5.1 also shows the locations of the inlet and outlet boundary conditions used to constrain the CSU 5-Stage collector flow field. The inlet velocity was set to 1.25 m/s to simulate the design flow rate of 2000 l/min through the collector. The outlet is located at the end of the fifth stage. A listing of the FLUENT files generated during the modeling of the CSU 5-Stage cloud collector can be found in Appendix E.

5.1.1 Description of air flow patterns

The steady state continuous phase flow field through the CSU 5-Stage collector is illustrated in Figures 5.2 - 5.6. The velocity field is represented by velocity vector arrows which indicate the magnitude and direction of the air flow at each control volume center. Velocity vectors are displayed for every other control volume in the first through fourth stages and for every control volume in the fifth stage. As air is drawn into the first stage inlet, it is accelerated by the converging first stage jet. The accelerated air stream is deflected by the first stage impaction surface, with the bulk of the air flowing along the impaction surface until reaching the second stage inlet. Two areas of weak recirculation accompany this main flow pattern. The first,

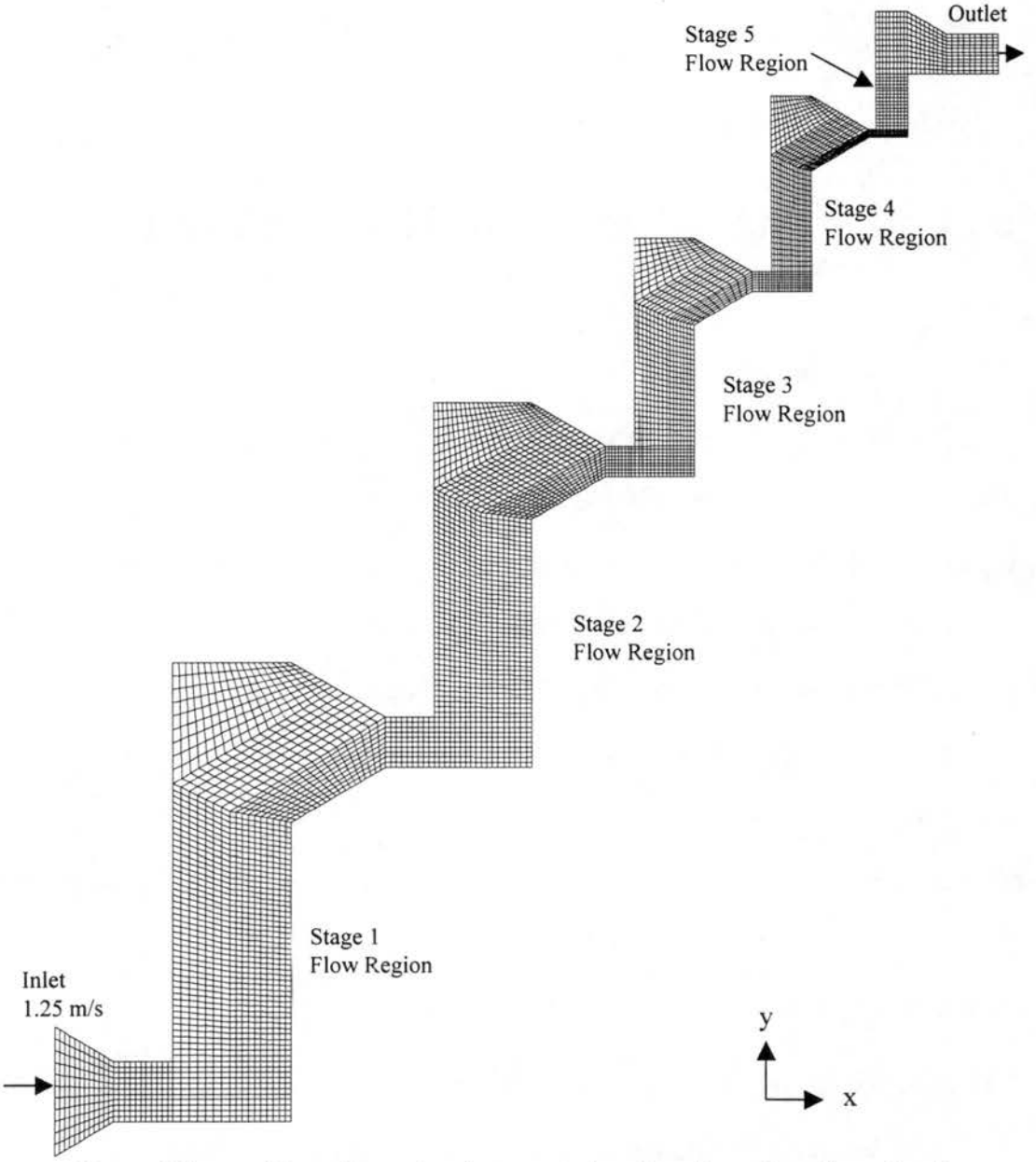

Figure 5.1 Two-dimensional computational mesh used to discretize the CSU 5-Stage collector flow domain.

and possibly most significant, is in the stagnation region created by the jet impingement on the impaction surface. The extent of this stagnation region may affect drop collection patterns in the first stage. The second recirculation zone develops along the wall opposite to the impaction surface. This larger recirculation directs a portion of the flow back toward the first stage jet. As the flow is diverted into the second stage inlet, another area of recirculation forms along the lower inlet surface. This pattern develops because the bulk air stream entering the second stage inlet is

unable to adhere to the wall as it transitions from the first stage impaction surface to the second stage inlet. The flow is further accelerated and straightened as it passes through the throat of the second stage inlet, although a velocity gradient persists across the width of the throat. As in the first stage, an area of recirculation develops along the wall opposite the impaction surface, forcing some flow back toward the second stage jet. In addition, an area of stagnation similar to that in the first stage results from the air stream impingement on the impaction surface. Unlike the first stage, however, this stagnation region has no recirculation associated with it.

Although higher velocities are progressively obtained in each of the remaining stages, the structure of the flow fields in the third, fourth and fifth stages are very similar to the flow field described for the second stage. Each stage inlet maintains a small recirculation region, and each stage possesses a large scale recirculation region. Due to the higher velocities encountered in each stage, the strengths of these recirculation zones progressively increase. As with the second stage, the remaining stages have jet impingement stagnation regions with no recirculation.

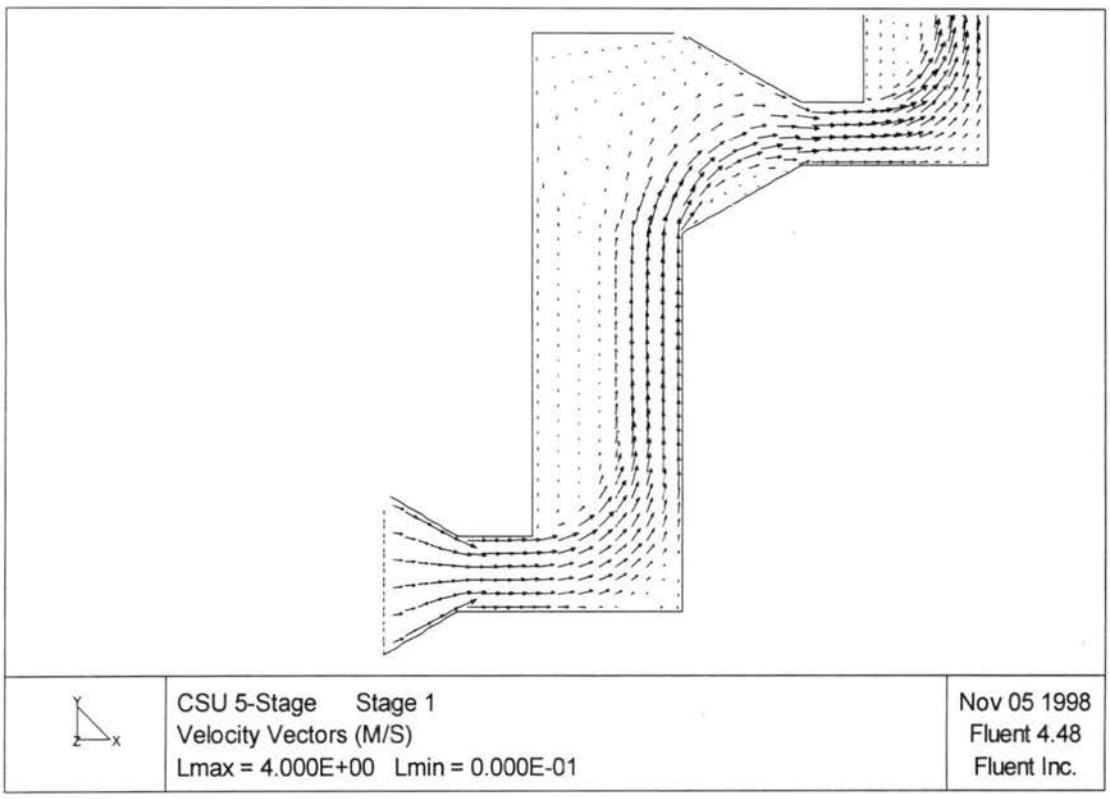

Figure 5.2 CSU 5-Stage collector stage 1 continuous phase flow field.

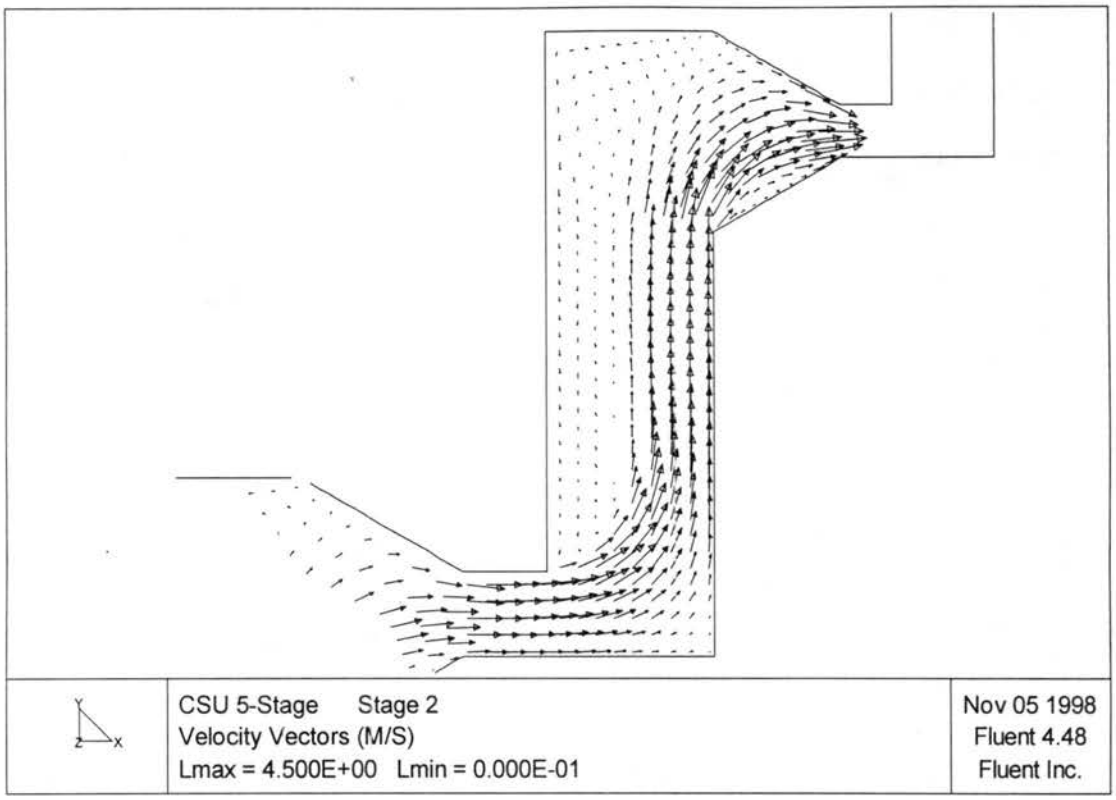

Figure 5.3 **CSU 5-Stage collector stage 2 continuous phase flow field.**

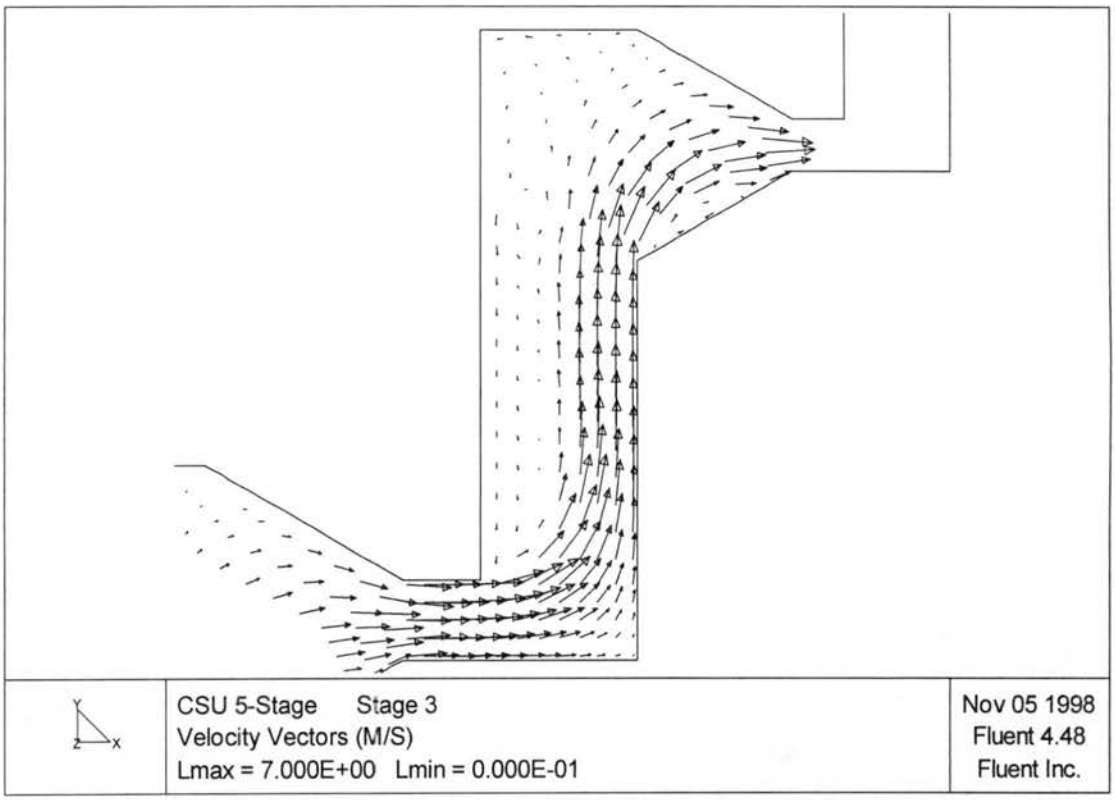

Figure 5.4 **CSU 5-Stage collector stage 3 continuous phase flow field.**

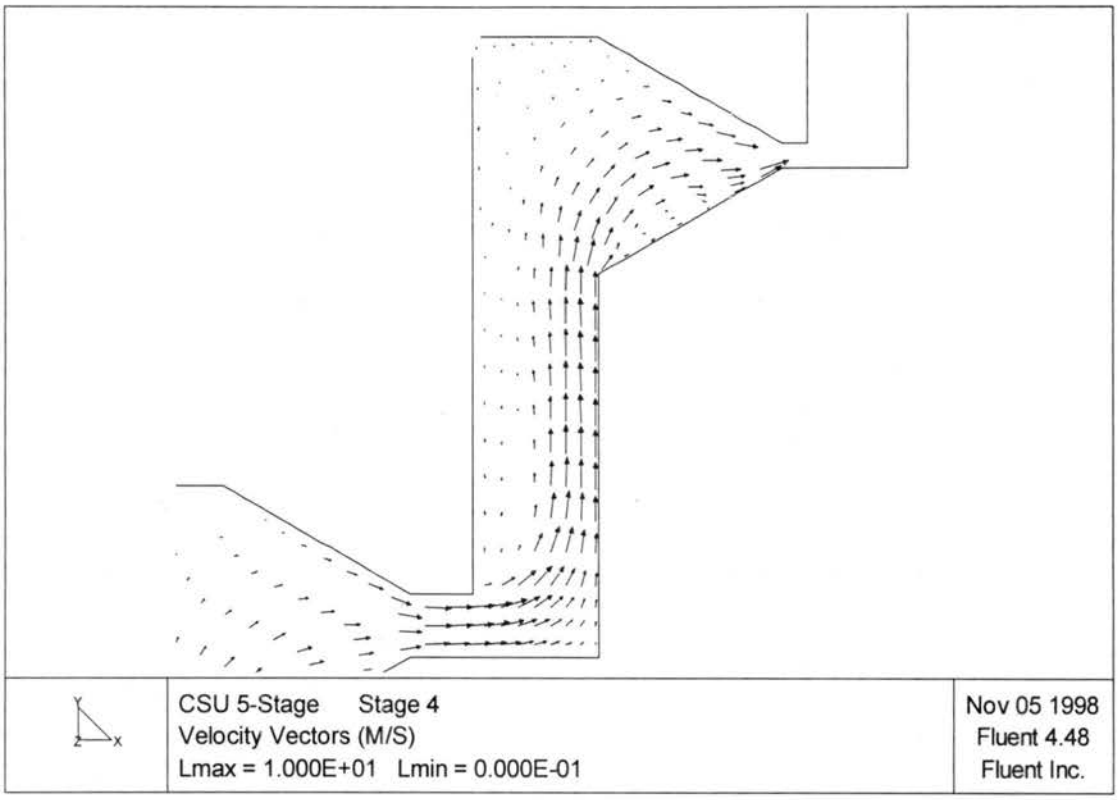

Figure 5.5 **CSU 5-Stage collector stage 4 continuous phase flow field.**

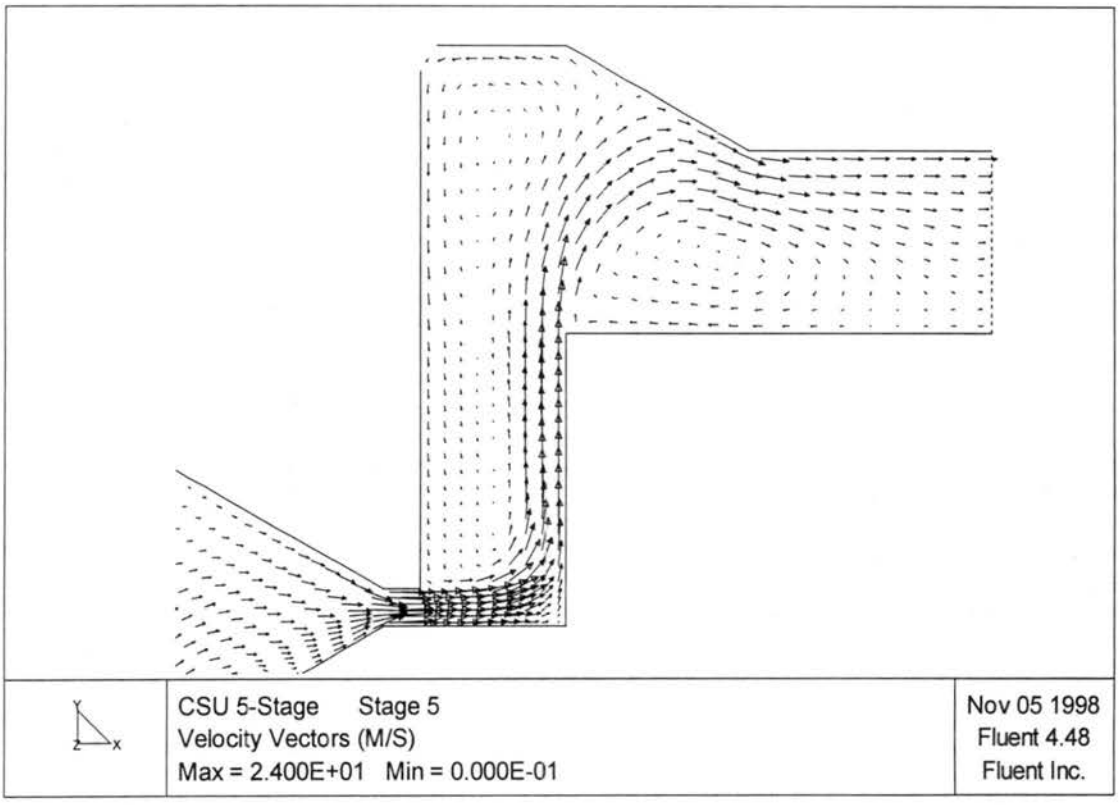

Figure 5.6 **CSU 5-Stage collector stage 5 continuous phase flow field.**

5.1.2 Drop trajectories

Based on the solution to the continuous phase flow field throughout the CSU 5-Stage collector, drop trajectory calculations were performed. Drops were released into the continuous phase solution at 100 points along the collector inlet. The drops were all given initial velocities of 1.25 m/s to match the continuous phase inlet velocity. The inlet angle of the drops, however, was varied across the inlet in order to match the inlet geometry. Drops immediately adjacent to the inlet walls were injected with a velocity vector at a 30° angle with respect to the inlet centerline so that their initial trajectories would be parallel to the walls. Drops at the inlet centerline were injected with a velocity vector normal to the inlet. The inlet velocity vectors of the remaining drops varied continuously between these extremes.

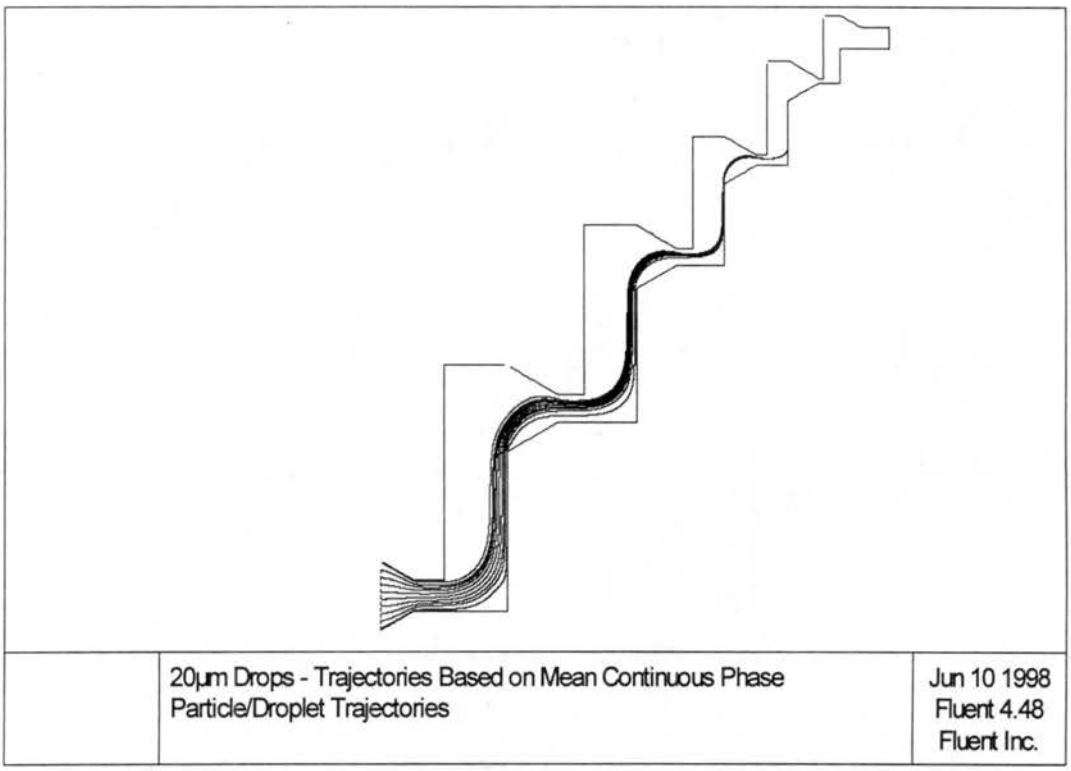

Figure 5.7 20 μm drop sample trajectories based on the mean continuous phase flow field of the CSU 5-Stage collector.

To illustrate the behavior of the drops as they interact with the continuous phase in their progression through the collector, sample trajectories of 20 μm drops are provided in Figures 5.7

and 5.8. Figure 5.7 shows 10 representative trajectories based on the mean continuous phase flow patterns. In this case, the paths that the drops assume essentially follow the bulk air flow patterns without significant deviation. The 20 μm drops pass through the first, second, and third stages before they possess enough inertia to diverge from the streamlines and impact the fourth stage collection surface. As the drops pass through each stage, the stage inlets and jet throats continuously focus the drop stream into a narrow band. This focusing effect, as well as other stage interactions, would not be captured if the collector's stages had been analyzed individually.

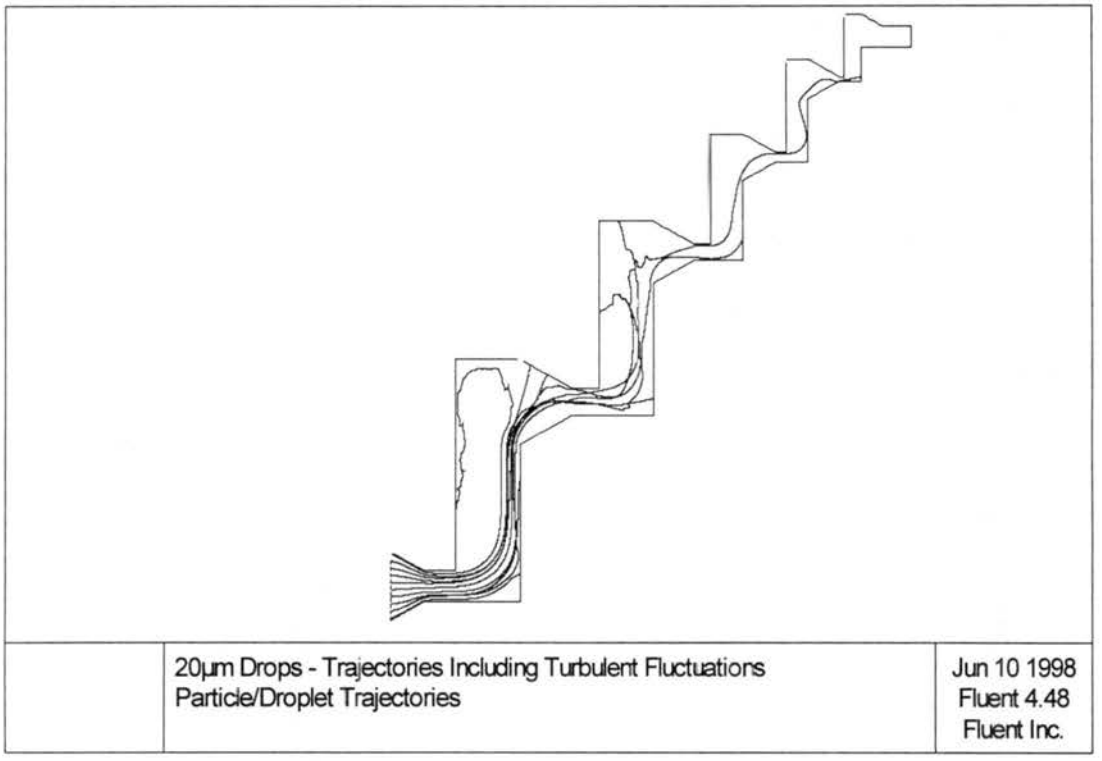

Figure 5.8 20 μm drop sample trajectories that include the effects of continuous phase velocity fluctuations.

Figure 5.8 shows 10 representative trajectories in which drop motion is affected by turbulent velocity fluctuations with $\alpha = 0.09$. The 20 μm drops are injected into the continuous phase solution from 10 locations distributed across the collector inlet. These drops no longer simply follow the bulk air flow through the collector. The drops exhibit irregular motion with rapid directional changes at times. These fluctuations permit the drops to more readily depart

from the air streamlines allowing the drops to enter the low velocity recirculation zones or deposit on interstage wall surfaces throughout the collector. In the 20 μm example, this substantially affects the drop collection patterns on the impaction surfaces and interstage walls. The collection efficiency is increased in the first three stages while being reduced in the fourth stage.

5.1.3 Efficiency curves

The drop collection patterns revealed through trajectory simulations for each drop size in the range of 2 to 60 μm were then used to construct efficiency curves for the CSU 5-Stage collector. Figure 5.9 shows collection efficiency curves in which the underlying trajectory calculations were based on the mean continuous phase velocities. The first stage efficiency curve has the "S" shape characteristic of most impactors while the efficiency curves of the remaining stages more closely resemble the step function shape of an "ideal" impactor. The sharpness of the efficiency curves in stages two through five is a result of the focusing that occurs at the inlet of each stage as previously described. An interesting consequence of the focusing effect is that the first and second stage efficiency curves cross at about 42 μm, resulting in higher collection efficiencies for drops sizes between 30 and 42 μm on the first stage than the second stage. Also note that the numerically predicted 50% cut diameters of 44, 43, 27, 17.5, and 7 μm that are displayed here, although for laboratory conditions, are far higher than the design 50% cut diameters of 30, 25, 15, 10, and 4 μm.

When turbulent velocity fluctuations (assuming $\alpha = 0.09$) are included in the trajectory calculations, the efficiency curves presented in Figure 5.10 result. As was the case with the addition of turbulent fluctuations to drop motion in the FROSTY collector modeling, the effect here is to significantly reduce the slopes of the efficiency curves for all stages. On any given stage, the turbulent fluctuations induce a significant portion of drops larger than the 50% cut diameter to pass by the collection surface while causing some portion of drops smaller than the 50% cut diameter to be collected. Unlike the FROSTY collector results, however, the 50% cut

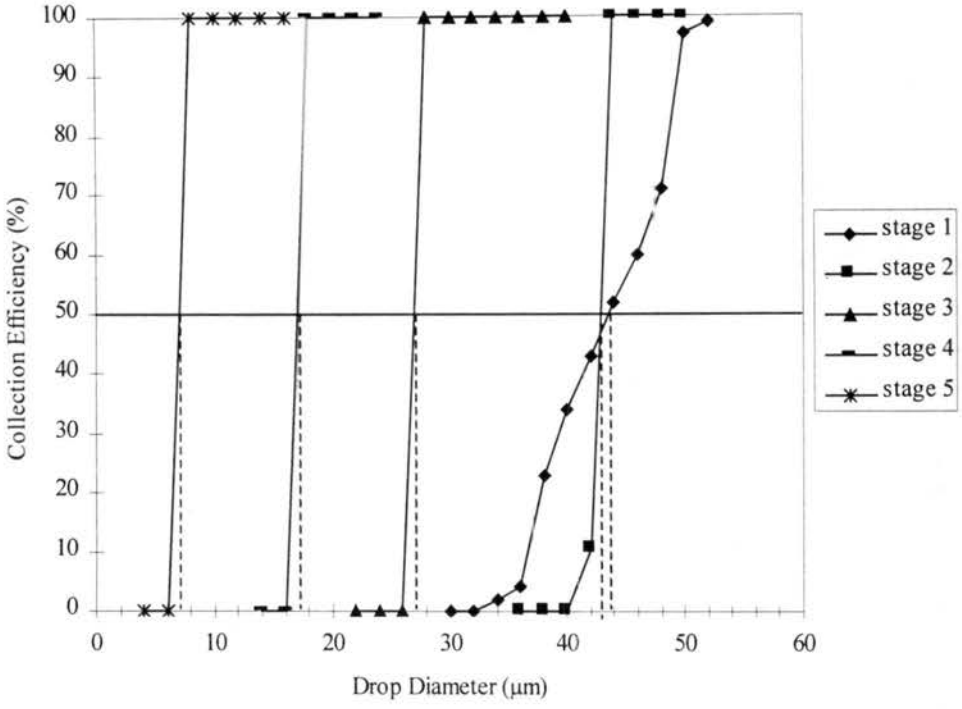

Figure 5.9 Numerically derived efficiency curves for the CSU 5-Stage cloud collector assuming trajectories that are based on the mean continuous phase velocity field. Stage 50% cut diameters are 44, 43, 27, 17.5, and 7 μm.

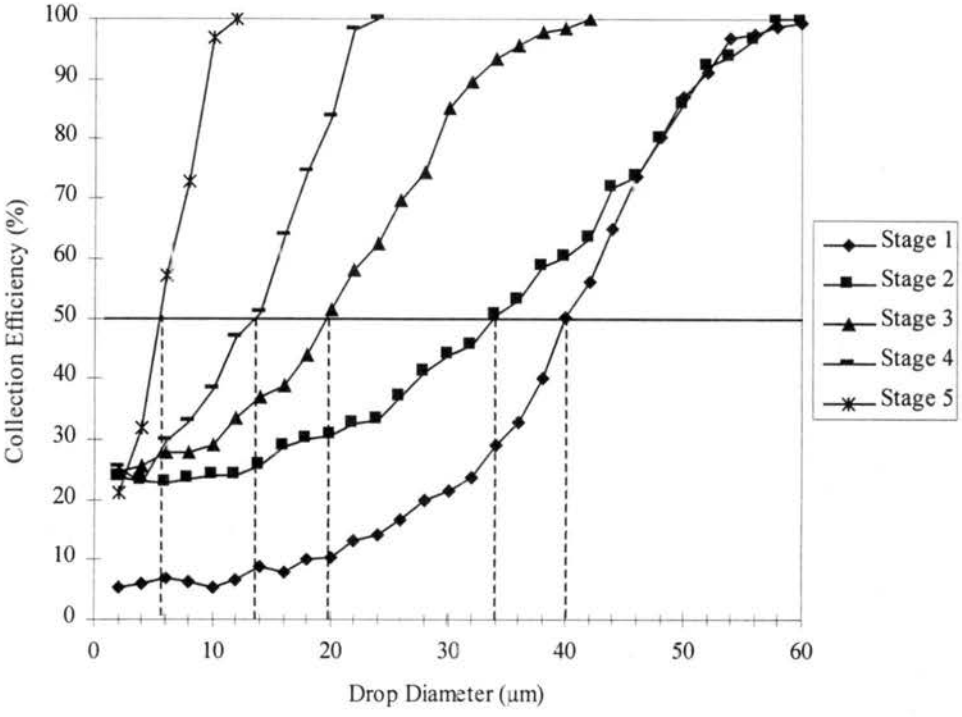

Figure 5.10 Numerically derived collection efficiency curves for the CSU 5-Stage collector assuming trajectories that include turbulent velocity fluctuations with $\alpha = 0.09$. Stage 50% cut diameters are 40, 34, 19.5, 13.5, and 5.5 μm.

diameters are also modified with the inclusion of turbulent fluctuations. For this case, the 50% cut diameters are 40, 34, 19.5, 13.5, and 5.5 μm.

5.2 Experimental Results

Collection efficiency curves derived from the experimental fluorimetric analysis of drop collection patterns through the CSU 5-Stage collector are presented in Figures 5.11, 5.12, and 5.13. Figure 5.11 shows experimental efficiency curves corrected only for multiplets. As discussed previously, except for the first stage, these curves do not have the traditional "S" shape due to wall losses and drop removal by previous stages. These curves do, however, provide a measure of the actual percentage of drops that are collected on each of the impaction surfaces. This information is necessary to define the populations of cloud drops that are collected by each stage during operation. These efficiency curves, corrected only for multiplets, indicate that unique populations of drops are collected on each stage, although considerable overlap does exist. Figure 5.12 repeats these efficiency curves, but includes error bars reflecting the 95% confidence limits discussed in section 3.2.5. For a listing of data obtained during the experimental calibration of the CSU 5-Stage collector, see Appendix C.

After correction for previous stage drop collection and wall losses, the resulting collection efficiency curves are shown in Figure 5.13. The 95% confidence limits are displayed as error bars. The first stage 95% confidence limits in Figure 5.13 are identical to those in Figure 5.12, however, the second and third stage 95% confidence limits account for the uncertainty in all of the measurements required to calculate the corrected efficiency curves. The 50% cut diameters can be identified in Figure 5.12 and compared to the model results. The first stage 50% cut diameter is 25.5μm, while the second stage 50% cut diameter is actually higher at 29 μm. The third, fourth, and fifth stage 50% cut diameters are 17.5 μm, 10.5 μm, and 4.5 μm, respectively. The portions of these efficiency curves in which the correction for wall losses and previous stage collection yielded highly uncertain results, as explained in section 3.4.2, have been removed.

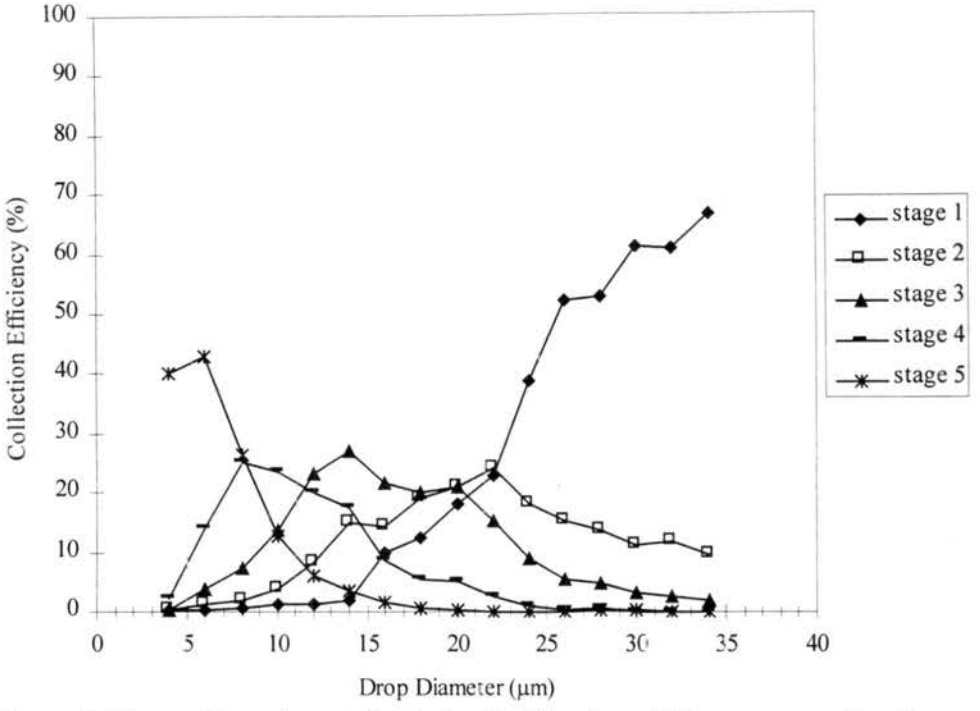

Figure 5.11 Experimentally derived collection efficiency curves for the CSU 5-Stage collector corrected to account for the presence of multiplets.

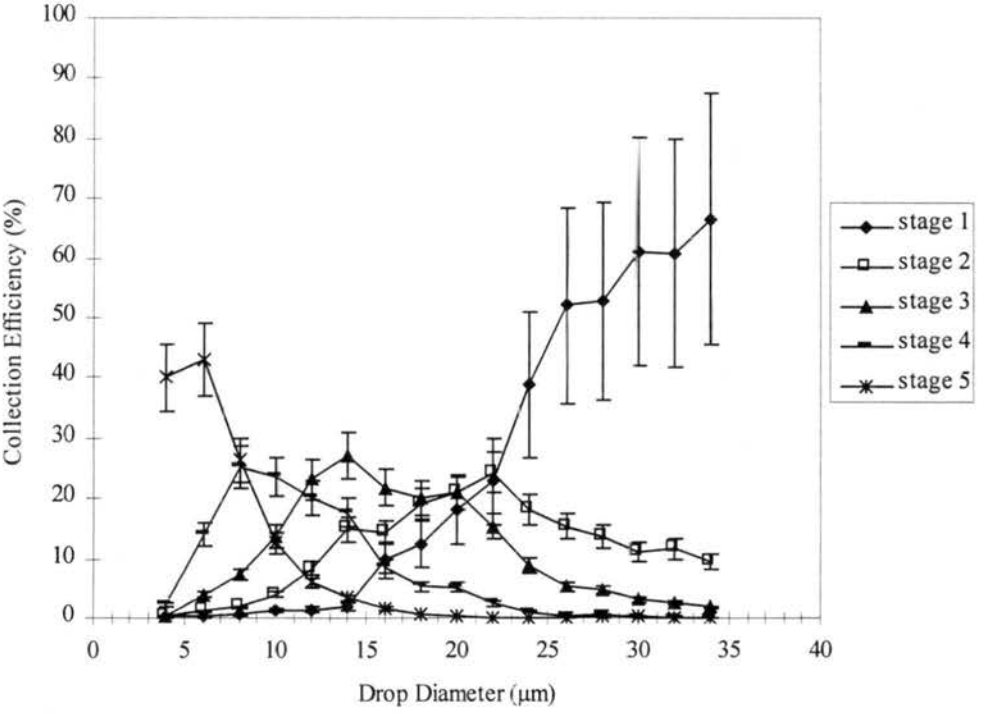

Figure 5.12 Experimentally derived collection efficiency curves for the CSU 5-Stage collector corrected to account for the presence of multiplets. Error bars represent 95% confidence limits.

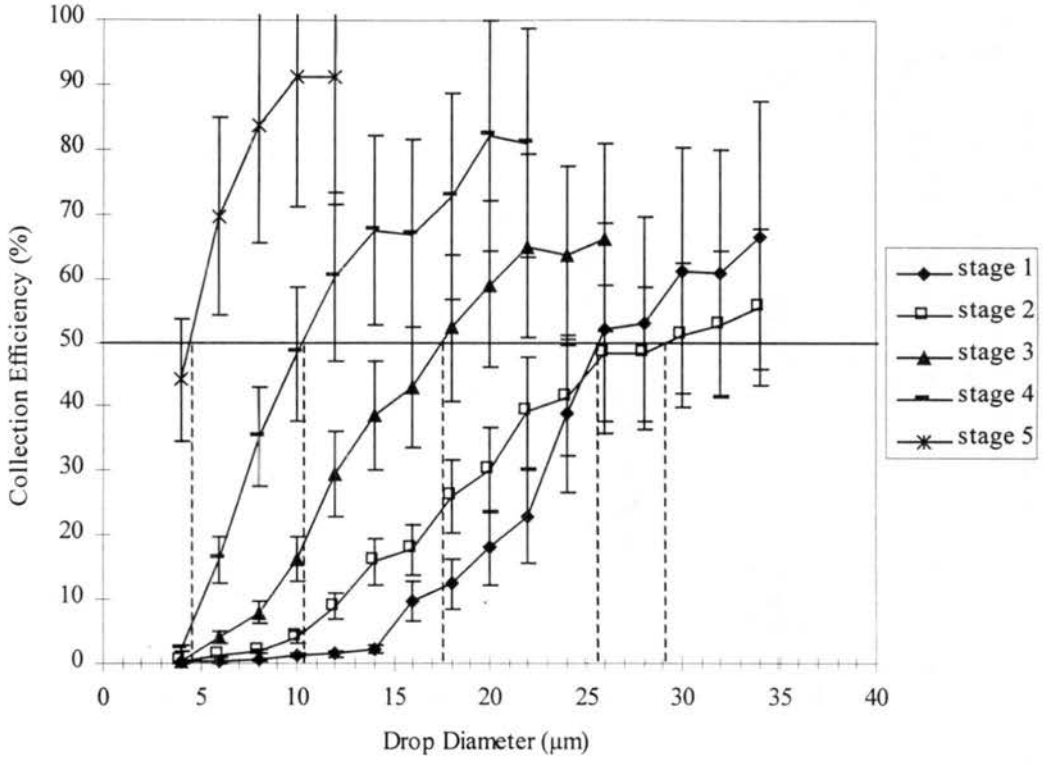

Figure 5.13 Experimentally derived collection efficiency curves for the CSU 5-Stage collector corrected for the presence of multiplets, previous stage collection, and wall losses. Stage 50% cut diameters are approximately 25.5, 29, 17.5, 10.5, and 4.5 μm. Error bars represent 95% confidence limits.

Drop collection on various interstage walls of the CSU 5-Stage collector was measured during the experimental calibration procedure in order to obtain an estimate of interstage wall losses. Results of these measurements, corrected for the presence of multiplets, are presented in Figure 5.14. Note that the range of the y-axis scale is from 0 to 50%. Total interstage wall losses increase with increasing diameter, peak in the 10 to 18 μm diameter range, and then begin to decrease again. At the maximum, losses to the interstage walls account for the fates of nearly 45% of the incoming drops. Because losses to the walls are fairly abundant across the drop size spectrum, drops collected on these surfaces may coalesce and flow under the influence of gravity toward the sample ports located at the bottom of each of the stages. As a result of this process, the cloudwater captured by the interstage walls will eventually accumulate in the sample vials

along with the cloudwater captured by the impaction surfaces. Unfortunately, determining which of the stage sample vials the cloudwater from a particular interstage wall surface is collected in was not straightforward due to the geometry and orientation of the collector. An investigation into the eventual fate of cloud drops captured by interstage wall surfaces was beyond the scope of this work. However, because of the significant fraction of cloudwater involved, the final destination of cloud drops lost to the interstage regions of the CSU 5-Stage collector should be quantified.

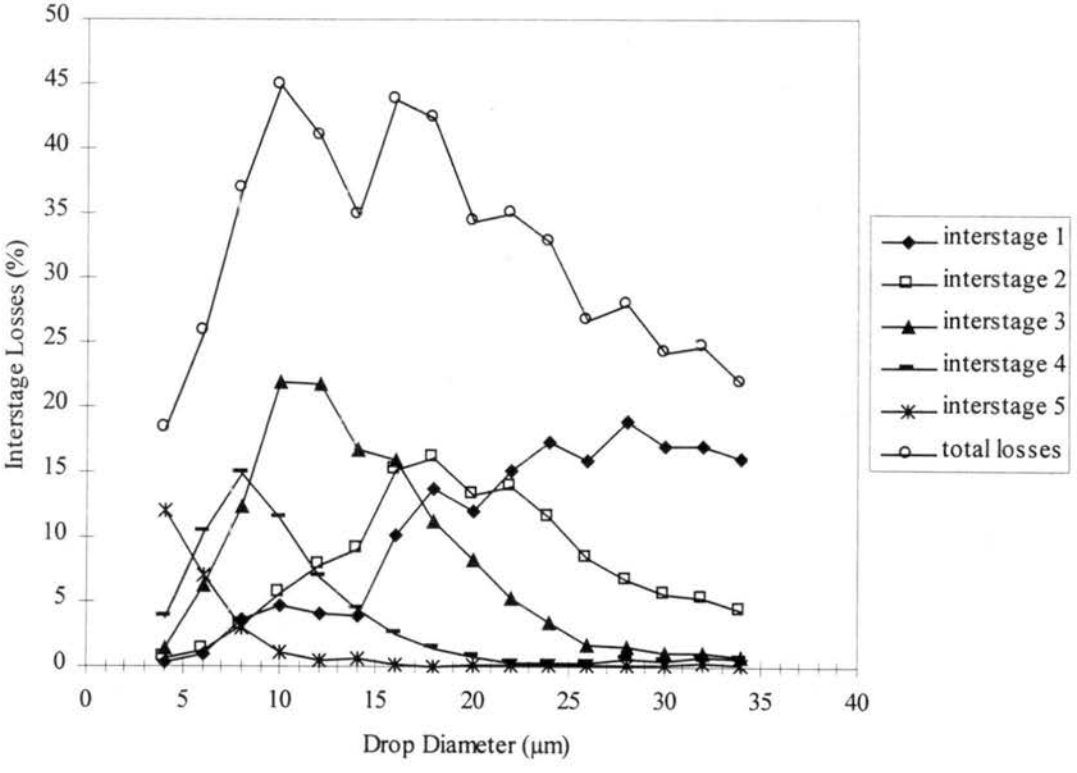

Figure 5.14 Experimentally measured interstage wall losses for the CSU 5-Stage cloud collector.

5.3 Discussion

5.3.1 Comparison of numerical and experimental results

The numerical and experimental collection efficiency curves for the CSU 5-Stage collector presented in the previous sections are compared in Figures 5.15 –5.19. As seen in

Figure 5.15, the numerical efficiency curves for stage 1, both with and without the effects of turbulent fluctuations on drop motion, inadequately predict the 50% cut diameters or the shape of the experimental efficiency curve. Both of the numerically derived curves indicate a 50% cut diameter that is far larger than the measured 50% cut diameter. This discrepancy could be due to inaccuracies in the continuous phase flow field solution, errors in the dispersed phase trajectory calculations, or inadequate specification in the model of the drop inlet conditions experienced during the experimental calibration. It was noted through visual inspection during the experimental calibration that drops were collected in the corner of the first stage whereas the numerical trajectory simulations indicated that no drops would be captured in that area. The numerically predicted, large continuous phase stagnation region formed as the jet impinges on the first stage impaction surface prevents drops from reaching the impaction surface in that area in the numerical modeling. The observation that drops actually do reach those surfaces during the experimental calibration affirms that modeling error such as an over prediction of the stagnation region or inadequacies in drop interaction with that stagnation region may be responsible for the efficiency curve discrepancies. Another possibility may be that the velocities and distribution of the calibration drops experienced at the CSU 5-Stage collector inlet during the experimental work were not accurately represented in the model. To investigate this possibility, several variations in the modeling of the continuous and dispersed phases at the CSU 5-Stage collector inlet were explored. The results of this investigation will be discussed in the following section.

The second stage numerical and experimental efficiency curves show better agreement in some areas than the first stage curves. This comparison is provided in Figure 5.16. As in the first stage, the numerical curve based on the mean continuous phase trajectories possess a 50% cut diameter that is far too high and, in this case, a slope that is unreasonably steep. However, the curve that includes turbulent fluctuations provides a better representation of the experimental efficiency curve, at least for drop diameters greater than 18 μm. The second stage 50% cut diameter is predicted with much greater accuracy than the first stage 50% cut diameter. For drops

smaller than 18 μm, however, the numerically predicted second stage curve levels out at about 25% collection whereas the measured collection efficiency curve drops to nearly zero with decreasing drop size. This excessive drop collection at smaller drop sizes was also noticed during the modeling of the FROSTY collector when excessive wall losses were observed in the numerical simulations. In each of these cases the flow patterns were similar, defined by a core of drop-laden air flow parallel to and adjacent to a wall surface for some distance. In the FROSTY collector, this pattern existed along the interstage wall surfaces; in the CSU 5-Stage collector, flow along the impaction surfaces fit this description. It appears that when this flow pattern exists, trajectory calculations that include turbulent velocity fluctuations over predict deposition of drops from the continuous phase flow to surfaces. Losses of smaller sized drops to wall surfaces can be reduced in this situation by decreasing the value of α to reduce interaction time between the drops and the turbulent eddies. This results in trajectories that deviate less from the paths defined by the mean continuous phase velocity field and therefore have less of a tendency to intersect wall surfaces. However, the reduction of drop losses by this method may be at the expense of accurate drop collection behavior in other situations, such as the collection of larger drops on an impaction surface due to drop laden jet impingement. In this case, values of α that are low enough to improve small drop wall loss predictions produce efficiency curves at larger drop sizes that no longer match experimental observations.

The third, fourth, and fifth stage efficiency curve comparisons in Figures 5.17, 5.18, and 5.19, respectively, show trends similar to those discussed for the second stage comparison. In all cases, the efficiency curves derived from trajectories based on average continuous phase velocities overestimate the 50% cut diameter and efficiency curve slope. Numerical efficiency curves in which the trajectories include dispersed phase turbulence produce 50% cut diameters and overall efficiency curve shapes that agree fairly well with the experimentally determined 50% cut diameters. However, at smaller drop sizes, drop collection is over predicted.

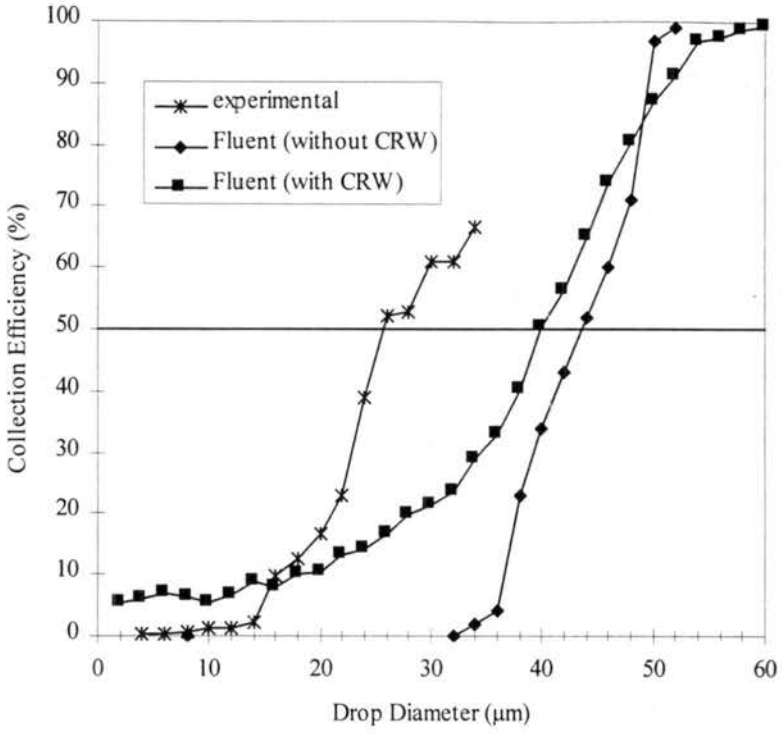

Figure 5.15 Stage 1 comparison between numerical and experimental efficiency curves for the CSU 5-Stage collector. The two numerical efficiency curves are based on drop trajectories that include (solid squares) and do not include (solid diamonds) the effects of turbulent velocity fluctuations.

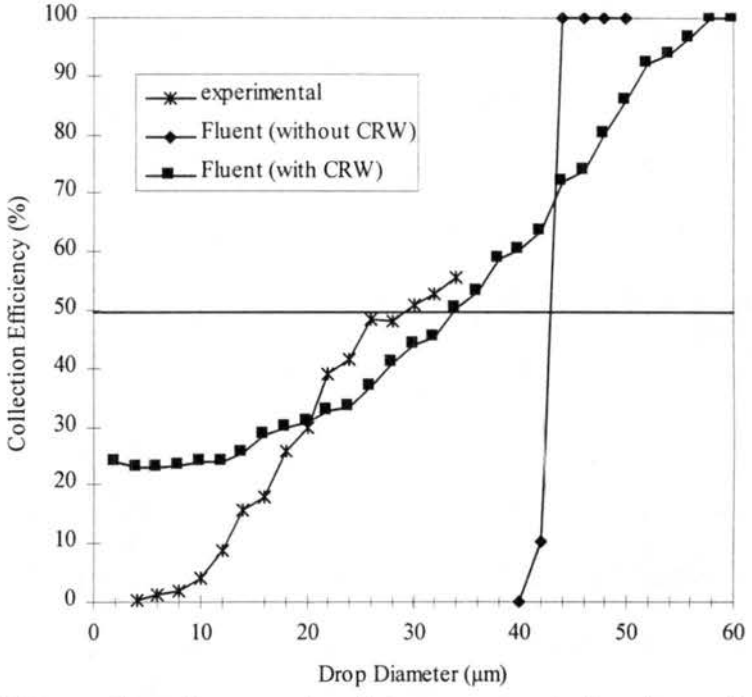

Figure 5.16 Stage 2 comparison between numerical and experimental efficiency curves for the CSU 5-Stage collector. The two numerical efficiency curves are based on drop trajectories that include (solid squares) and do not include (solid diamonds) the effects of turbulent velocity fluctuations.

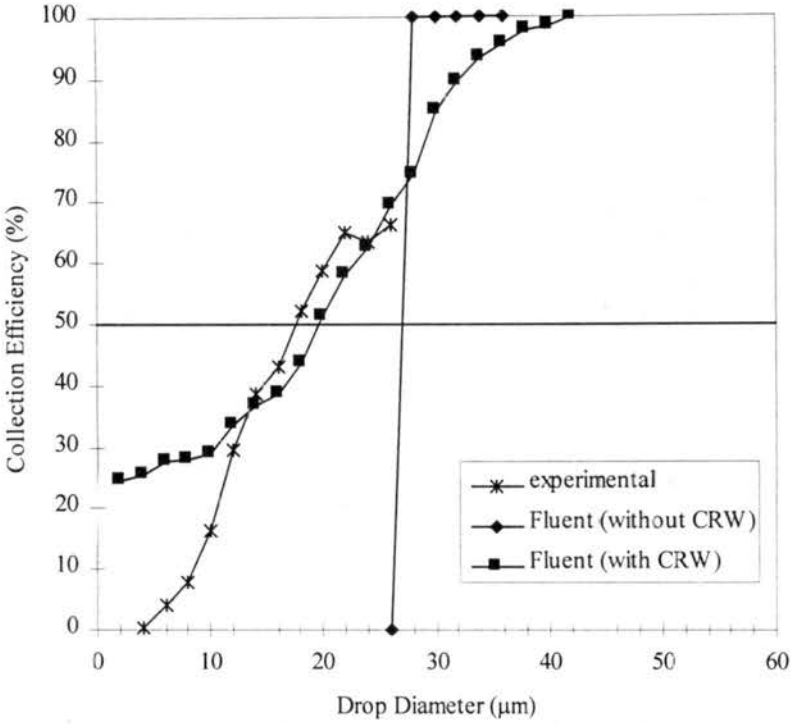

Figure 5.17 Stage 3 comparison between numerical and experimental efficiency curves for the CSU 5-Stage collector. The two numerical efficiency curves are based on drop trajectories that include (solid squares) and do not include (solid diamonds) the effects of turbulent velocity fluctuations.

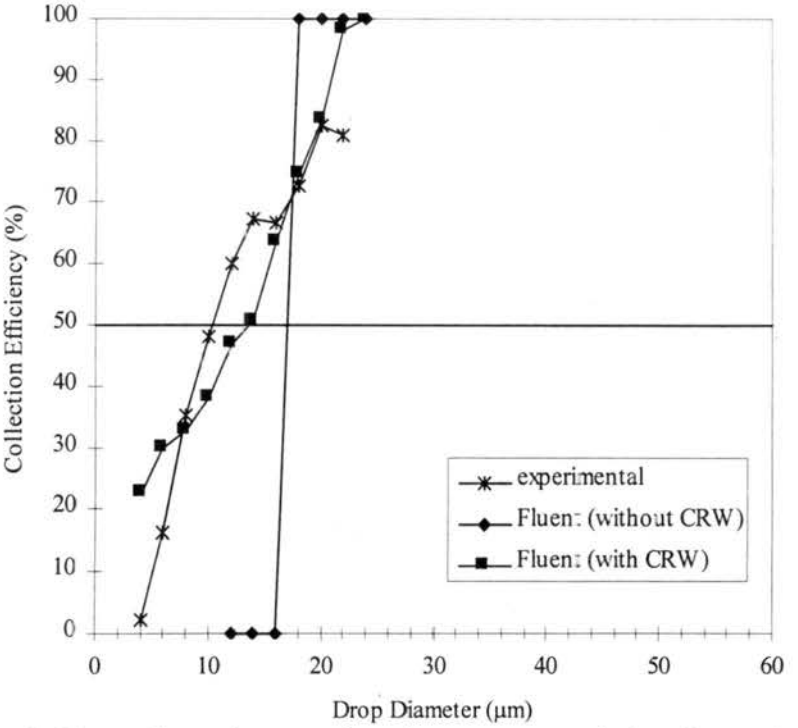

Figure 5.18 Stage 4 comparison between numerical and experimental efficiency curves for the CSU 5-Stage collector. The two numerical efficiency curves are based on drop trajectories that include (solid squares) and do not include (solid diamonds) the effects of turbulent velocity fluctuations.

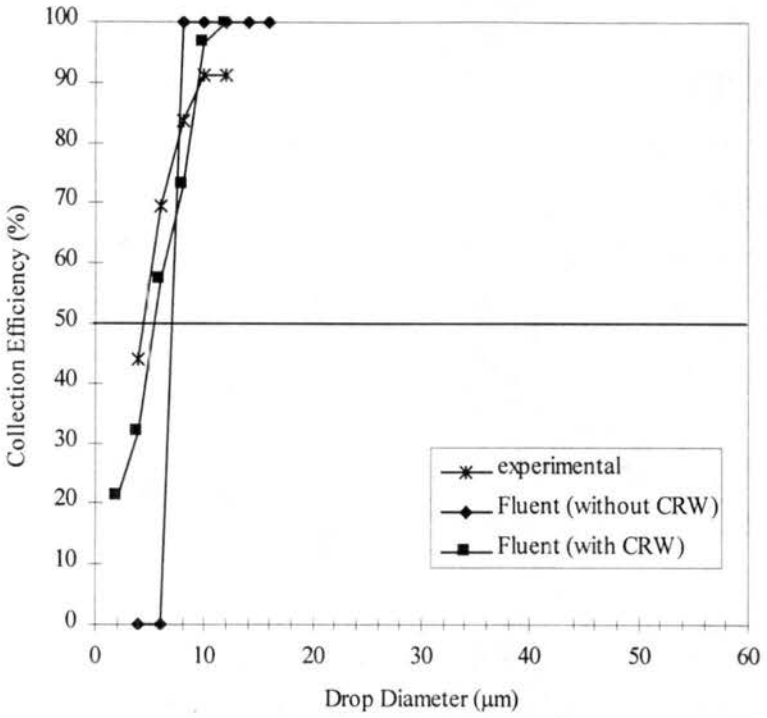

Figure 5.19 Stage 5 comparison between numerical and experimental efficiency curves for the CSU 5-Stage collector. The two numerical efficiency curves are based on drop trajectories that include (solid squares) and do not include (solid diamonds) the effects of turbulent velocity fluctuations.

5.3.2 Inlet Modeling

Additional modeling of the CSU 5-Stage collector inlet was performed in an attempt to explain the discrepancy between the first stage numerical and experimental collection efficiency curves seen in Figure 5.15. In particular, two variations in the modeling of the collector inlet region were explored. The first examined the effects of changes in the distribution of the calibration drop stream across the inlet. The second variation extended the continuous phase flow domain beyond the collector inlet to include a region of ambient air upstream of the inlet.

In all of the numerical modeling presented to this point, it was assumed that the drops entering the CSU 5-Stage collector were distributed evenly across the width of the inlet. Therefore, drop trajectory simulations were initiated from locations along the entire width of the inlet. If, during the experimental calibration procedure, the calibration drop stream was instead focused toward the center of the inlet, the above assumption would be inaccurate. This could

possibly result in incorrect first stage collection patterns and therefore explain the previously observed numerically predicted efficiency curve discrepancies. To examine this possibility, drops were introduced into the continuous phase solution distributed across only the center half of the inlet width. Only trajectories that included the effects of continuous phase velocity fluctuations on drop motion were calculated. Efficiency curves were constructed as described in section 2.4.6 based on these trajectory simulations. These efficiency curves are displayed as dashed lines in Figure 5.20, while the original efficiency curves that assume that drops enter the collector distributed evenly across the inlet are included in solid lines for comparison. The main effect of focusing the calibration drops toward the center of the inlet is to lower the first stage efficiency curve slightly at drop sizes smaller than about 32 μm. The efficiency curves for the second through fourth stages remain essentially unchanged. This indicates that changes in the distribution of drops across the inlet has relatively little effect on the efficiency curves and can not account for the discrepancy between the CSU 5-Stage collector's first stage numerical and experimental efficiency curves.

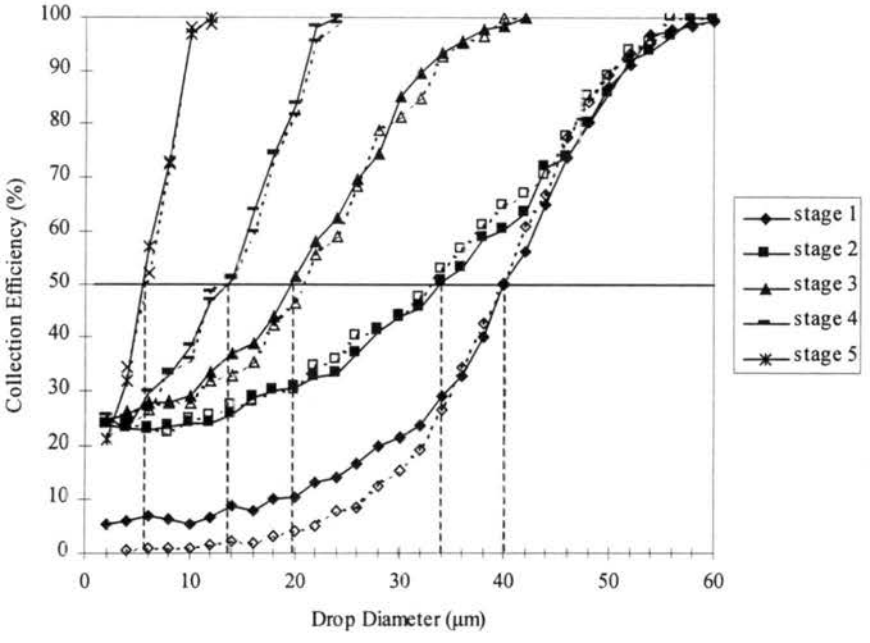

Figure 5.20 Numerically derived collection efficiency curves for the CSU 5-Stage collector that include turbulent velocity fluctuations with $\alpha = 0.09$. Solid lines indicate curves for drops distributed across the entire inlet while dashed lines indicate curves for drops focused toward the center half of the inlet.

To provide a more accurate representation of continuous and dispersed phase conditions at the CSU 5-Stage collector's inlet, the computational domain was extended to include a region directly upstream of the inlet. The additional 10.2 cm by 10.2 cm flow domain is illustrated in Figure 5.21. For this configuration, a continuous phase solution was generated only for the first two stages of the CSU 5-Stage collector. A pressure drop across the two stages was specified in order to provided the required flow rate through the collector. In addition, in order to simulate the flow of air containing the calibration drops from the VOAG outlet, which would be located at the left boundary of the flow domain, a velocity of 0.8 m/s was specified along a portion of that boundary. The resulting flow field can be seen in Figure 5.21. At the center of the inlet, air is drawn in normal to the inlet plane as was observed when the additional flow domain was not modeled. However, at the inlet walls, where air is drawn in from around the edges of the inlet, the flow is nearly parallel to the inlet plane. This results in a significant focusing of the calibration drop stream toward the center of the inlet.

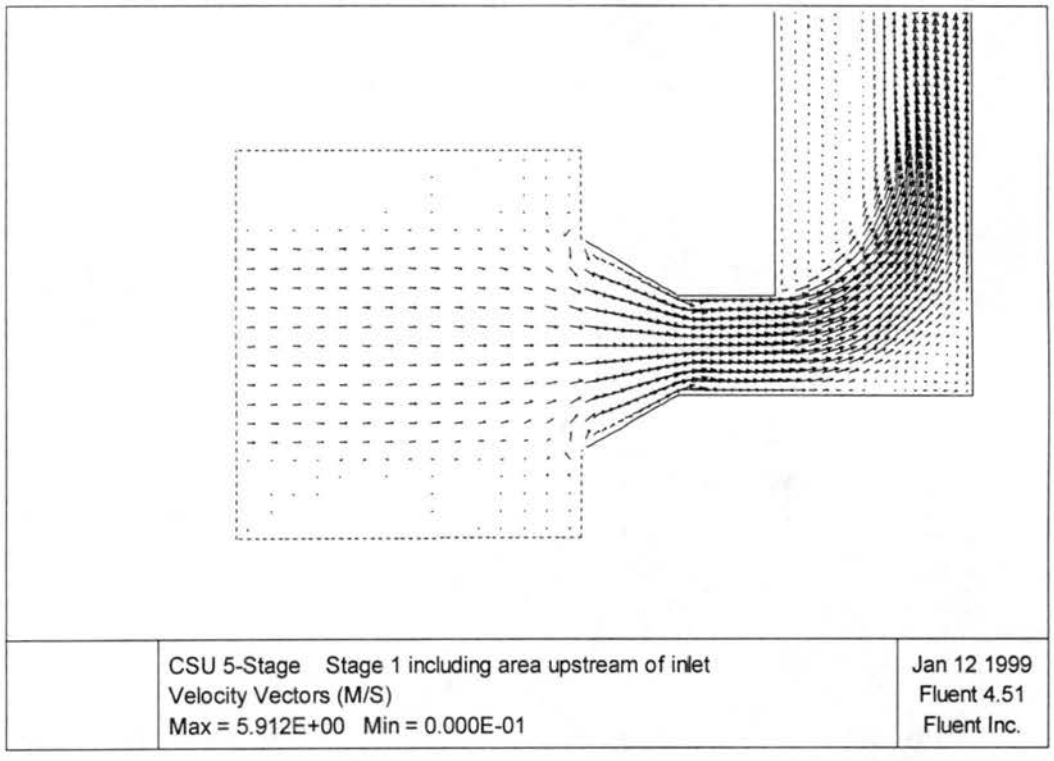

Figure 5.21 Continuous phase flow field for the CSU 5-Stage collector inlet and extended upstream flow region.

For this investigation, ten drops were released from each of 100 locations at the left boundary, distributed across a distance of 3.8 cm to correspond to the width of the VOAG outlet. Trajectories were calculated with the inclusion of turbulent velocity fluctuations. The resulting efficiency curve for the first stage can be seen in Figure 5.22. Included for comparison in this figure is the original first stage numerical efficiency curve as well as the first stage experimental efficiency curve. The focusing that occurs when the additional region upstream of the inlet is modeled results in a first stage efficiency curve with a steeper slope. In addition, the 50% cut diameter is shifted to much smaller drop sizes. With the additional upstream region modeled, the first stage numerical efficiency curve is in slightly better agreement with the experimentally derived curve. However, a significant discrepancy between the numerical and experimental efficiency curves still exists.

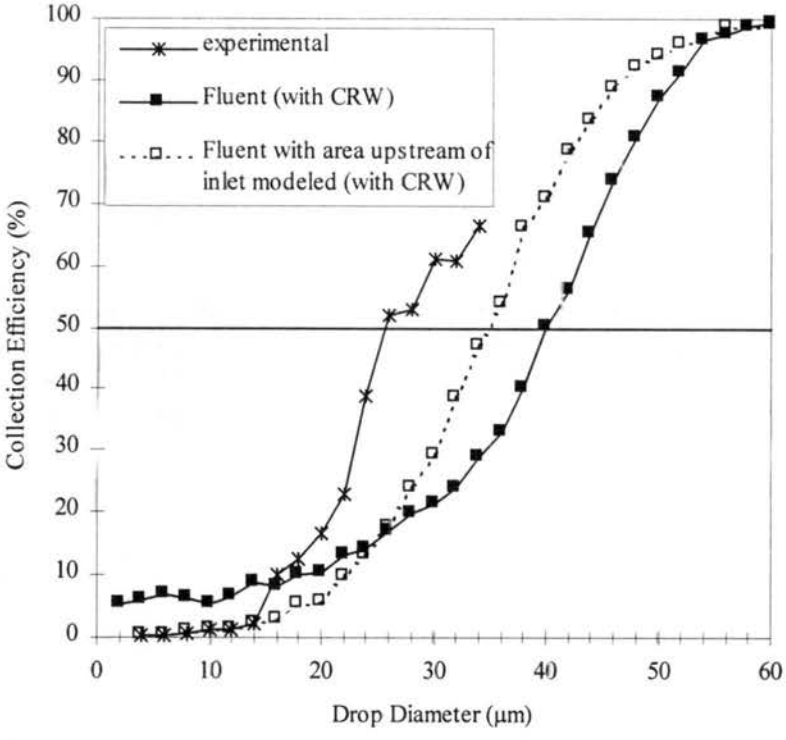

Figure 5.22 Stage 1 comparison between efficiency curves based on the original numerical modeling (solid squares), numerical modeling in which an extended flow region upstream of the inlet is included (open squares), and experimental work (asterisks) for the CSU 5-Stage collector.

The new and original numerical efficiency curves for the second stage of the CSU 5-Stage collector are shown in Figure 5.23. In this figure, the two numerical efficiency curves are nearly identical, indicating that variations in inlet conditions become negligible by the second stage. The over prediction of small drop collection, as noted earlier, still exists.

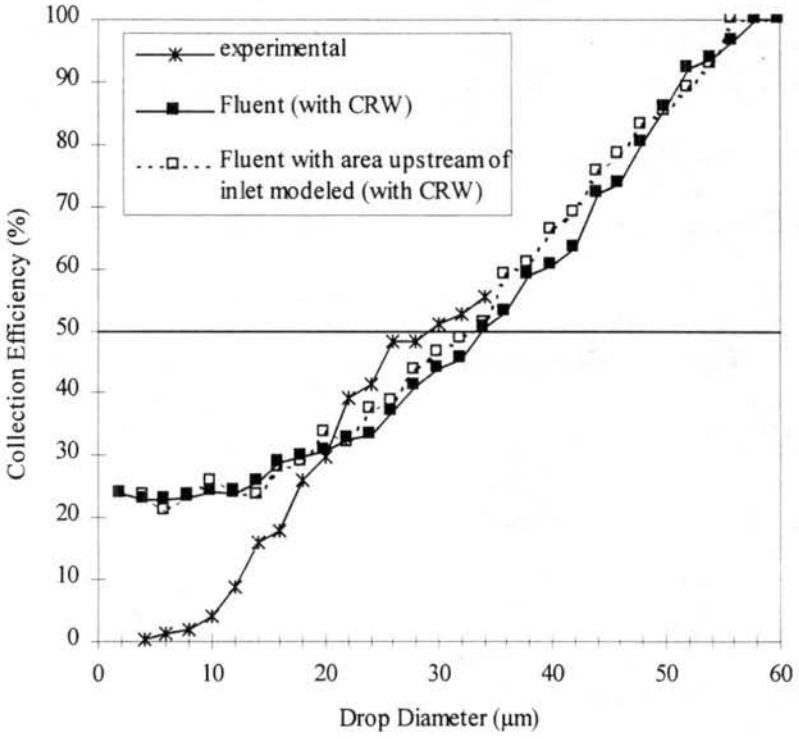

Figure 5.23 Stage 2 comparison between efficiency curves based on the original numerical modeling (solid squares), numerical modeling in which an extended flow region upstream of the inlet is included (open squares), and experimental work (asterisks) for the CSU 5-Stage collector.

5.3.3 Calibration at design conditions

The ambient conditions under which the experimental calibration of the CSU 5-Stage collector was performed correspond to a laboratory setting at 1500 m elevation, and are described in section 2.3.6. In addition, the calibration drop density of 0.9 g/cm^3 was slightly lower than the density of water. The CSU 5-Stage collector was designed for use in an environment associated with warm cloud sampling near sea level. Numerical simulations of the collector's performance were therefore performed at these design conditions in order to provide an estimate of the effects

that ambient conditions have on collection performance. The sea level standard atmosphere (0 m, 15° C) properties that represent design conditions include a continuous phase density of 1.23 kg/m^3 and viscosity of 1.79×10^{-5} Ns/m^2. A dispersed phase density of 1 g/cm^3 is used. A comparison between the simulations at laboratory conditions and design conditions is provided in Figure 5.24. Apart from some slight variations, the two sets of curves are very similar. The increase in the continuous phase density from Simlab to design conditions tends to decrease drop collection at a given diameter and therefore shifts the efficiency curves to larger diameters. The increase in dispersed phase density increases collection at a give diameter and therefore shifts the efficiency curves to smaller drop sizes. The decrease in viscosity from Simlab to design conditions would tend to shift the efficiency curves to smaller drop sizes, however, the change in viscosity was minor and the effects are probably negligible. It appears these competing effects largely offset one another.

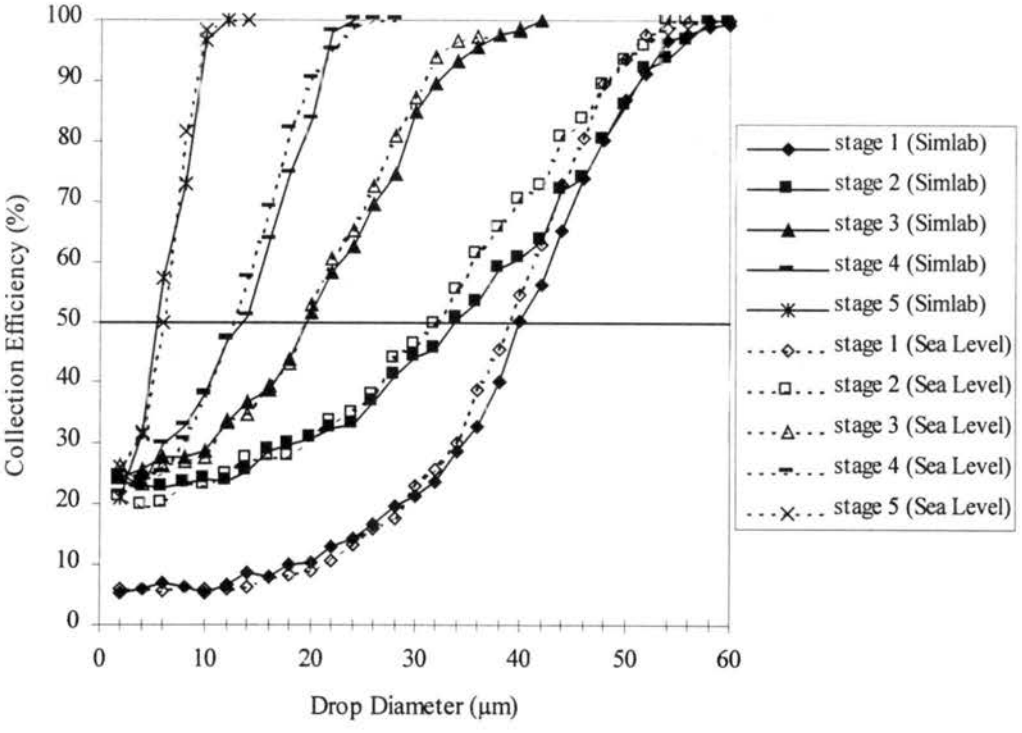

Figure 5.24 Comparison of collection efficiency curves based on numerical trajectory simulations at laboratry conditions and design conditions for the CSU 5-Stage collector.

5.3.4 Populations of drops expected on each surface for typical ambient cloud drop size distributions

An exercise similar to the one described in section 4.3.4 for the FROSTY collector was conducted to illustrate the populations of drops that would be collected on the five stages of the CSU 5-Stage cloud collector during operation. The experimentally derived collection efficiency curves corrected only for multiplets presented in section 5.2, modified to remove the influence of the calibration drop density, were applied to two ambient cloud drop distributions representative of cloudy environments that could be encountered during sampling. CSU 5-Stage collector efficiencies at the bin midpoint diameters of the ambient distribution were linearly interpolated from known calibration points. The ambient volume distributions, with volume weighted average diameters of 12.6 and 17.7 μm, are depicted in the top two panels of Figure 5.25. Directly below these top panels are the associated volume distributions of drops that would be collected by the five stages of the collector. Note the change in the y-axis scale between panels. The vertical lines in each panel indicate the volume weighted average diameter for each distribution of collected drops. The error bars represent the 95% confidence limits described in section 3.2.5.

The volume weighted mean diameters of the collected cloudwater fractions would be 16.2, 13.8, 12.9, 11.7, and 10.2 μm for stages 1 through 5 if the CSU 5-Stage cloud collector were used to sample the 12.6 μm volume average diameter distribution illustrated in Figure 5.25. If the 17.7 μm volume average diameter distribution were sampled, the resulting populations of collected drops would have volume weighted mean diameters of 20.1, 18.2, 17.0, 15.1, and 12.6 μm on stages 1 through 5. This demonstrates that unique populations of drops can be collected on each of the CSU 5-Stage cloud collector's five stages during field study operations. The bottom panel in Figure 5.25 shows the distribution of cloud drops that would be lost to interstage wall surfaces during sampling.

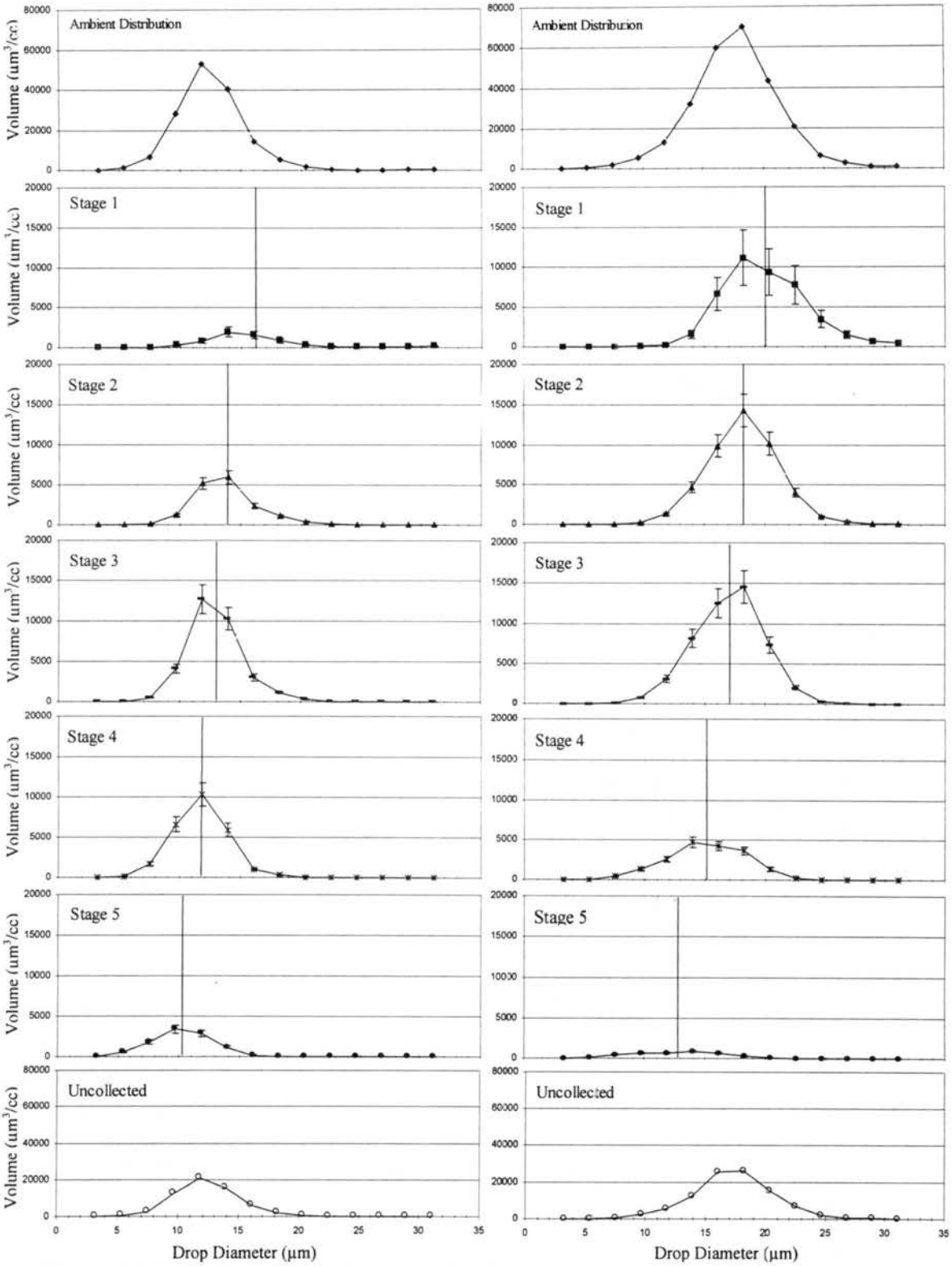

Figure 5.25 Volume distributions showing the ambient, collected, and uncollected drop populations for two cases for the CSU 5-Stage cloud collector. Volume weighted mean diameters indicated by the vertical lines for the first through fifth stages are 16.2, 13.8, 12.9, 11.7, and 10.2 μm for case 1 and 20.1, 18.2, 17.0, 15.1, and 12.6 μm for case 2. Note the change in y-axis scale between panels.

6 Conclusions, Recommendations, and Future Work

An evaluation of the collection characteristics of two new multi-stage cascade inertial impactors designed for size-resolved cloud drop collection has been performed. The FROSTY supercooled cloud collector is intended for the collection of supercooled cloud drops in a winter environment in three independent size fractions with stage 50% cut diameters of 15 μm, 10 μm, and 4 μm. The CSU 5-Stage cloud collector is designed for sampling warm clouds in five distinct fractions on five stages that have 50% cut diameters of 30, 25, 15, 10, and 4 μm. The established inertial impactor design guidelines of Marple (1970) and Marple and Rubow (1986) provided the foundation for the development of these cloud collectors. In order to verify the desired performance, as predicted by these guidelines, calibrations of the FROSTY and CSU 5-Stage cloud collectors were performed to quantitatively assess the populations of cloud drops collected on each of the collectors' stages. This work ensures that accurate conclusions regarding the nature of chemical variations with cloud drop size can be made using data from the two collectors.

Two approaches were selected for the evaluation of the FROSTY and CSU 5-Stage cloud collectors. Numerical simulations provided a visualization of the air flow patterns and drop trajectories through the collectors while experimental laboratory calibrations provided a quantitative analysis of true collection performance. For each of these methods, 50% cut diameters, efficiency curves, and wall losses for each stage of the FROSTY and CSU 5-Stage collectors were derived. Comparisons between the numerically and experimentally generated results provided insight into the capabilities and limitations of the numerical modeling.

The experimental calibration work was performed in a laboratory setting at 1500 m elevation with calibration drops that had a slightly lower density than water. Therefore, slight modifications of the experimental results must be made when applying these results to different sampling conditions. At laboratory conditions, the experimentally determined 50% cut diameters for the three stages of the FROSTY supercooled cloud collector were 19, 11.5, and 5 μm. Drop losses to the interstage wall surfaces in the FROSTY collector peaked at approximately 35% for 16 μm drops and were lower for larger and smaller drop sizes. Although there is overlap between the efficiency curves for the three impaction surfaces, the experimental work does indicate that three distinct fractions of cloudwater can be collected. This was demonstrated by applying the measured collection efficiency curves to representative ambient cloud drop distributions to assess the distributions of cloud drops collected on each impaction surface.

Similar overlap between populations of collected drops was observed during the experimental calibration of the CSU 5-Stage cloud collector. Despite this overlap, it was again demonstrated that distinct distributions of cloud drops were collected on each of the five stages. The experimentally determined 50% cut diameters, measured at laboratory conditions, for the CSU 5-Stage cloud collector were 25.5, 29, 17.5, 10.5, and 4.5 μm. Wall losses tended to be higher than those for the FROSTY cloud collector across the drop size range under consideration. Losses peaked at nearly 45% for drops between 10 and 18 μm and decreased to about 20% at the largest and smallest drop sizes. Because the CSU 5-Stage collector samples warm clouds, drops collected in the interstage regions may accumulate and flow under the influence of gravity and aerodynamic drag into the preceding or succeeding stage sample collection vials. Further investigation in this area is needed to quantify these effects.

The large volume of air that needs to be processed to provide sufficient cloudwater for chemical analysis in time periods that allow for adequate time resolution of composition changes results in high flow rates through the collectors. The FROSTY and CSU 5-Stage collectors were designed for operation at flow rates of 1500 and 2000 l/min, respectively. A desire to minimize

the overall size of the collectors required high jet Reynolds numbers to accommodate the high flow rates. The design jet Reynolds numbers for both collectors are 10,000, which is at the upper limit recommended for impactor design. The collection efficiency curve overlap observed during the experimental calibration efforts appears to be the result of turbulence in the flow field associated with collector operation at high Reynolds numbers.

The numerical modeling of the FROSTY and CSU 5-Stage cloud collectors was performed with the commercially available Computational Fluid Dynamics (CFD) software package FLUENT, from Fluent, Inc. FLUENT's multiphase capabilities were used to examine the air flow patterns as well as drop trajectories through the two collectors. Conditions reflecting the air and drop properties of the laboratory experimental calibration were applied in the model to allow comparison between the numerical analysis and experimental observations. Additional numerical modeling was conducted at conditions representing the design environment of the collectors to provide an estimate of the changes in collector performance that would be expected.

When performing numerical trajectory simulations, FLUENT offered two alternatives for the treatment of continuous phase velocities in the equations that describe drop motion. Drop trajectory calculations could be based on the average continuous phase velocity field or they could optionally include turbulent velocity fluctuations statistically derived from continuous phase turbulent parameters. Trajectories were calculated for both alternatives. The resulting drop collection patterns were used to generate collection efficiency curves for each stage of the collectors. Subsequent comparison of the numerically predicted collection efficiency curves with curves established through experimental calibration indicated that the inclusion of turbulent fluctuation effects on drop motion provided better agreement with experimental observations. However, the use of velocity fluctuations defined by default parameters also produced unrealistic losses to wall surfaces for small drop sizes. This phenomenon occurred primarily in situations in which drop-laden flow travels parallel and adjacent to a wall surface. Adjustment of the drop / turbulent eddy interaction time, T_L, allowed some modification of turbulent drop behavior. It was

determined that reductions in the interaction time, accomplished by lowering the interaction time constant, α, to a value of 0.09, produced drop collection patterns that were in better agreement with experimental data. However, even with this reduced interaction time, wall losses at small drop size were over predicted. Further reductions of the interaction time were unable to eliminate the excessive wall losses before a decrease in the accuracy of drop collection patterns at larger drop sizes was apparent. Additional investigation into the effects of drop / turbulent eddy interaction or other parameters that control turbulent drop dispersion may be needed to provide improvements in numerical trajectory simulations. Despite this shortcoming, the FLUENT software does appear to be capable of offering significant insight into flow patterns and drop trajectories that may be valuable during the cloud collector design process.

Numerically derived efficiency curves based on mean flow trajectories for the FROSTY collector predicted 50% cut diameters of 21.5, 12, and 4.5 μm. These values matched experimental values reasonably well. However, the slopes of the efficiency curves for all three stages were excessively steep. Assuming a value of $\alpha = 0.09$, efficiency curves including the effects of turbulent velocity fluctuations on drop motion provided similar predictions of the 50% cut diameters (20.5, 13.5, and 5 μm) but offered better agreement with the overall experimental efficiency curve shape. Numerical simulations suggest that the 50% cut diameters for the first, second, and third stages decrease approximately 2, 1, and 0.5 μm, respectively, for operation at 3000 m elevation in winter conditions.

The numerical simulations for the CSU 5-Stage collector did not agree as well with the experimental data. As with the FROSTY collector, the slopes of the efficiency curves produced from mean flow based drop trajectories were overly steep. In addition, however, the 50% cut diameters for the five stages (44, 43, 27, 17.5, and 7 μm) were significantly over predicted as well. The agreement of efficiency curve slopes and 50% cut diameters with experimental results both improved when turbulent velocity fluctuations were included in trajectory calculations with

$\alpha = 0.09$. In this case, the predicted 50% cut diameters for the five stages were 40, 34, 19.5, 13.5, and 5.5 μm at laboratory conditions. Numerical simulations at design conditions revealed that minimal changes in the 50% cut diameters from those measured at laboratory conditions should be expected. The large discrepancy between numerically predicted and experimentally observed collection characteristics for the first stage were never resolved. Possible sources of error include inaccuracies in the continuous phase flow field solution for that stage or incorrect drop interaction with that flow field. Continued modeling efforts may help establish the cause of this discrepancy.

In addition to the supplemental work suggested above, further research can be conducted to extend the numerical and experimental results presented here. This includes performing CSU 5-Stage collector experimental calibrations at drop sizes larger than 34 μm to completely describe stage collection characteristics. Also, additional calibration replicates would help reduce the uncertainty associated with the experimental collection efficiency curves. The effects of drop-drop interactions in the FROSTY and CSU 5-Stage collectors, especially as polydisperse cloud drop streams are focused into very narrow regions as the flow is accelerated through each jet, has not been explored. Further study to address the significance of this issue would be beneficial. Finally, numerical modeling extensions in three dimensions could provide characterization of jet end effects that were neglected in the two-dimensional modeling and could possibly provide more realistic turbulence parameterization.

References

Asgharian, B., and Godo, M. N. (1997). Transport and deposition of spherical particles and fibers in an improved virtual impactor. *Aerosol Sci Technol.* **27**:499-506.

Asgharian, B., Zhang, L., and Fang, C. P. (1997). Theoretical calculations of the collection efficiency of spherical particles and fibers in an impactor. *J. Aerosol Sci.* **28**(2)277-287.

Abuzeid, S., Busnaina, A. A., and Ahmadi, G. (1991). Wall deposition of aerosol particles in a turbulent channel flow. *J. Aerosol Sci.* **22**(1)43-62.

Bator, A., and Collett, J. L. Jr. (1997). Cloud chemistry varies with drop size. *J. Geophys. Res.* **102**(D23):28071-28078.

Berglund, R. N., and Liu, B. Y. H. (1973). Generation of monodisperse aerosol standards. *Environ. Sci. Technol.* **7**(2):147-153.

Berner, A., Dusek, U., Galambos, Z., and Kruisz, C. (1998). Sampling of fog droplets by cascade impactors. *Contr. Atmos. Phys.* **71**(1):101-114.

Chen, Q., and Ahmadi, G. (1997). Deposition of particles in a turbulent pipe flow. *J. Aerosol Sci.* **28**(5)789-796.

Collett, J. L. Jr., Oberholzer, B., and Staehelin, J. (1993). Cloud chemistry at Mt. Rigi Switzerland: Dependence on drop size and relationship to precipitation chemistry. Atmos. Environ. **27A**:33-42.

Collett, J. L. Jr., Bator, A., Rao, X. and Demoz, B. B. (1994) Acidity variations across the cloud drop size spectrum and their influence on rates of atmospheric sulfate production. *Geophys. Res. Lett.* **21**(22):2393-2396.

Collett, J. Jr., Iovinelli, R., and Demoz, B. (1995). A three-stage cloud impactor for size-resolved measurements of cloud drop Chemistry. *Atmos. Environ.* **29**(10):1145-1154.

Demoz, B.B., Collett, J. L. Jr., and Daube, B. C. Jr. (1996). On the caltech active strand cloudwater collectors. *Atmos. Res.* **41**:47-62.

Durst, F., Milojevic. D., and Schonung, B. (1984). Eulerian and Lagrangian predictions of particulate two-phase flows: a numerical study. *Appl. Math. Modelling.* **8**:101-115.

Fan, J., Zhang, X., Cheng, L., and Cen, K. (1997). Numerical simulation and experimental study of two-phase flow in a vertical pipe. *Aerosol Sci. Technol.* **27**:281-292.

Ferziger, J. H., and Peric, M. (1996). *Computational Methods for Fluid Dynamics.* Springer, Berlin, pp.25-37,67-83,162-168.

Fluent Incorporated. (1996). *FLUENT User's Guide, Release 4.4.* Lebanon, N.H., Vol. 1-4.

Frank, T., and Schulze I. (1994). Numerical simulation of gas-droplet flow around a nozzle in a cylindrical chamber using a Lagrangian model based on a multigrid Navier-Stokes solver. *ASME Numerical Methods in Multiphase Flows - 1994* (Crowe, C. T., Johnson, R., Prosperetti, A., Sommerfeld, M., and Tsuji, Y., eds.) **FED-Vol. 185**:93-107.

Freitas, C. J. (1995). Perspective: Selected benchmarks from commercial CFD codes. *ASME Journal of Fluids Engineering.* **117**:208-218.

Gong, H., Anand, N. K., and McFarland, A. R. (1993). Numerical prediction of the performance of a shrouded probe sampling turbulent flow. *Aerosol Sci. Technol.* **19**:294-304.

Griffiths, W. D., and Boysan, F. (1996). Computational Fluid Dynamics (CFD) and empirical modeling of the performance of a number of cyclone samplers. *J. Aerosol Sci.* **27**(2)281-304.

Hillamo, R. E., and Kauppinen, E. I. (1991). On the performance of the Berner low pressure impactor. *Aerosol Sci. Technol.* **14**:33-47.

Hindman, E. E., Carter, E. J., Borys, R. D., and Mitchell, D. L. (1992). Collecting supercooled cloud droplets as a function of droplet size. *J. Atmos. Oceanic Tech.* **9**(4)337-353.

Hoffmann, M. R. (1986). On the kinetics and mechanism of oxidation of aquated sulfur dioxide by ozone. *Atmos. Environ.* **20**:1145-1154.

Hoag, K. J. (1997). *Heterogeneous fog chemistry and S(IV) oxidation in the San Joaquin Valley.* M.S. thesis, Colorado State University.

Hoag, K. J., Collett, J. L. Jr., and Pandis, S. N. (1999). The influence of drop size-dependent fog chemistry on aerosol processing by San Joaquin Valley fogs. *Atmos. Environ.* Submitted July, 1998.

Ibusuki, T., and Takeuchi, K. (1987). Sulfur dioxide oxidation by oxygen catalyzed by mixtures of manganese (II) and iron (III) in aqueous solutions at environmental reaction conditions. *Atmos. Environ.* **21**:1555-1560.

Iovinelli, R. (1994). *Design and calibration of a multistage cloudwater cascade jet impactor based on a prototype two-stage impactor.* M.S. thesis, University of Illinois, Urbana, Illinois.

Jurcik, B., and Wang, H. C. (1995). On the shape of impactor efficiency curves. *J. Aerosol Sci.* **26**(7):1139-1147.

Laj, P., Fuzzi, S., Lazzari, A., Ricci, L., Orsi, G., Berner, A., Dusek, U., Schell, D., Gunther, A., Wendisch, M., Wobrock, W., Frank, G., Martinsson, B. G., Hillamo, R. (1998). The size dependent composition of fog droplets. *Contr. Atmos. Phys.* **71**(1):115-130.

Laucks, M. L., and Twohy, C. H. (1998). Size-dependent collection efficiency of an airborne Counterflow Virtual Impactor. *Aerosol Sci. Technol.* **28**:40-61.

Launder, B. E. (1989). Second-moment closure: present... and future? *Int. J. Heat and Fluid Flow.* **10**(4):282-300.

Launder, B. E., and Spalding, D. B. (1974). The numerical computation of turbulent flows. *Computer Methods in Applied Mechanics and Engineering.* **3**:269-289.

Leonard, B. P. (1979). A stable and accurate convective modelling procedure based on quadratic upstream interpolation. *Computer Methods in Applied Mechanics and Engineering.* **19**:59-98.

Li, A., and Ahmadi, G. (1992). Dispersion and deposition of spherical particles from point sources in a turbulent channel flow. *Aerosol Sci. Technol.* **16**:209:226.

Marple, V. A. (1970). *A fundimental study of inertial impactors.* Ph.D. thesis, University of Minnesota.

Marple, V. A., and Liu, B. Y. (1974). Characteristics of laminar jet impactors. *Environ. Sci. Technol.* **8**(7):648-654.

Marple, V. A., and Willeke, K. (1976). Impactor design. *Atmos. Environ.* **10**:891-896.

Marple, V. A., and Rubow, K. L. (1986). *Cascade Impactor Sampling and Data Analysis.* (J. P. Lodge, Jr. and T. L. Chan, eds.) AIHA, Akron, pp.X-X.

Marple, V. A., Rubow, K. L., Turner, W., and Spengler, J. D. (1987). Low flow rate sharp cut impactors for indoor air sampling: design and calibration. *JAPCA.* **37**(11):1303-1307.

Marple, V. A., Olson, B. A., and Miller, N. C. (1995). A low-loss cascade impactor with stage collection cups: calibration and pharmaceutical inhaler applications. *Aerosol Sci. Technol.* **22**:124-134.

McFarland, A. R., Gong, H., Muyshondt, A., Wente, W. A., and Anand, N. K. (1997). Aerosol deposition in bends with turbulent flow. *Environ. Sci. Technol.* **31**(12)3371-3377.

Millet, M., Wortham, H., and Mirabel, PH. (1995). Solubility of polyvalent cations in fogwater at an urban site in Strasbourg (France). *Atmos. Environ.* **29**(19):2625-2631.

Morsi, S. A., and Alexander, A. J. (1972). An investigation of particle trajectories in two-phase flow systems. *J. Fluid Mech.* **55**(2):193-208.

Munger, J. W., Collett, J. L. Jr., Daube, B. Jr., and Hoffmann, M. R. (1989). Chemical composition of coastal stratus clouds: Dependence on droplet size and distance from the coast. *Atmos. Environ.* **23**:2305-2320.

Munson, B.R., Young, D. F., and Okiishi, T. H. (1990). *Fundamentals of Fluid Mechanics.* John Wiley & Sons, New York, pp.146,319-338,372-373,484-502.

Muyshondt, A., McFarland, A. R., and Anand, N. K. (1996). Deposition of aerosol particles in contraction fittings. *Aerosol Sci. Technol.* **24**:205-216.

Noone, K. J. (1987). *Size selective cloud drop sampling using a counterflow virtual impactor.* Ph.D. thesis, University of Washington.

Noone, K. J., Charlson, R. J., Covert, D. S., Ogren, J. A., and Heintzenberg, J. (1988). Cloud droplets: solute concentration is size dependent. *J. Geophys. Res.* **93D**:9477-9482.

Ogren, J. A., Heintzenberg, J., Zuber, A., Noone, K. J., and Charlson, R. J. (1989). Measurement of the size-dependence of solute concentrations in cloud droplets. *Tellus.* **41B**:24-31.

Ogren, J. A., and Charlson, R. J. (1992). Implications for models and measurements of chemical inhomogeneities among cloud droplets. *Tellus.* **44B**:208-225.

Olan-Figueroa, E., McFarland, A. R., and Ortiz, C. A. (1982). Flattening coefficients for DOP and oleic acid droplets deposited on treated glass slides. *Am. Ind. Hyg. Assoc.* **43**:395-399.

Patankar, S. V. (1980). *Numerical heat Transfer and Fluid Flow.* Hemisphere Publishing Corp., Washington, D. C.

Radar, D. J., and Marple, V. A. (1985). Effect of ultra-stokesian drag and particle interception on impaction characteristics. *Aerosol Sci. Technol.* **4**:141-156.

Rao, X., and Collett, J. L. Jr. (1998). The drop size-dependence of iron and manganese concentrations in clouds and fogs: implications for sulfate production. *J. Atmos. Chem.* **30**:273-289.

Schell, D., Maser, R., Wobrock, W., Jaeschke, W., Georgii, H. W., Kos, G. P. A., Arends, B. G., Beswick, K. M., Bower, K. N., and Gallagher, M. W. (1997). A two-stage impactor for fog droplet collection: design and performance. *Atmos. Enviro.* **31**(16)2671-2679.

Schmitt, G. *Methoden und Ergebnisse der Nebelanalyse.* Ph.D. thesis, Institute of Meteorology and Geophysics, University of Frankfurt.

Seinfeld, J.H., and Pandis, S. N. (1998). *Atmospheric Chemistry and Physics.* John Wiley & Sons, New York, pp.480-484.

Shirolkar, J. S., Coimbra, C. F. M., and McQuay, M. Q. (1996). Fundamental aspects of modeling turbulent particle dispersion in dilute flows. *Prog. Energy Combust. Sci.* **22**:262-399.

Swanson, P. D., Muzzio, F. J., Annapragada, A., and Abjei, A. (1996). Numerical analysis of motion and deposition of particles in cascade impactors. *Int. J. Pharm.* **142**:33-51.

Thomson, D. J. (1987). Criteria for the selection of stochastic models of particle trajectories in turbulent flows. *J. Fluid Mech.* **180**:529-556.

Vong, R. J., Baker, B. M., Brechtel, F. J., Collier, R. T., Harris, J. M., Kowalski, A. S., McDonald, N.C., and McInnes, L. M. (1997). Ionic and trace element composition of cloud water collected on the Olympic Peninsula of Washington State. *Atmos. Environ.* **31**(13):1991-2001.

Xu, G., Sherman, D. E., Andrews, E., Moore, K., Hoag, K., and Collett, J. L. Jr. (1999). The influence of chemical heterogeneity among cloud drop populations on aerosol processing in winter clouds. *Atmos. Res.* Accepted subject to minor revision.

Appendix A - Conversion of Partial Differential Conservation Equations to Algebraic Equivalents

The governing conservation equations of fluid motion (equations 2.1 and 2.2) must be converted from partial differential equations to algebraic equivalents so that a solution can be obtained through numerical methods. For an illustration of this transformation, the equations in differential form are applied in steady state to a one-dimensional grid with cell center nodes W, P, and E, and cell faces w and e, as seen in Figure A.1.

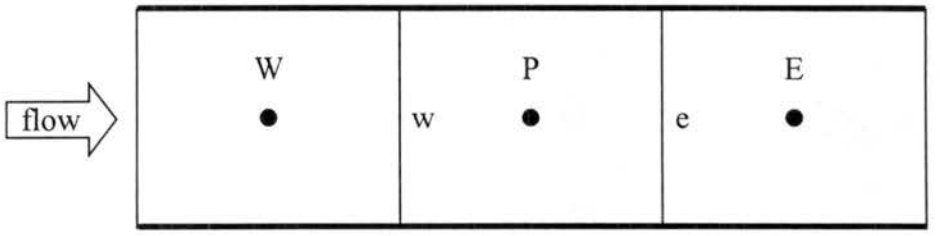

Figure A.1 One-dimensional grid illustrating wall and cell center positions.

Equations 2.1 and 2.2 are integrated over the volume of each element, with the use of the divergence theorem to reduce the volume integrals to surface integrals:

$$\int_{Volume} \nabla \cdot F \; dV = \int_{S} F \cdot n \; dS \qquad \text{(A.1)}$$

where the function F represents a function in three dimensions (Pi+Qj+Rk) and n is normal to the surface S.

In the case of one dimensional, steady state flow with no source or sink terns, the continuity equation reduces to:

$$\frac{\partial}{\partial x}(\rho u) = 0 \qquad \text{(A.2)}$$

where ρ and u are the fluid density and velocity. If equation A.2 is integrated over the control volume with cell center P in Figure A.1, the divergence theorem would yield:

$$\int_{Volume} \frac{\partial}{\partial x}(\rho u) dV = \int_{S} \rho u \; dS \tag{A.3}$$

where S is the control volume surface. The net flux ρu through the control volume's boundary is evaluated as the sum of the integrals over the two faces (designated e and w in Figure A.1) of the control volume (or the sum of four faces for a two-dimensional control volume, or sum of six faces for a three-dimensional control volume):

$$\int_{S} \rho u \; dS = \int_{S_e} \rho u \; dS_e + \int_{S_w} \rho u \; dS_w \tag{A.4}$$

where the subscripts e and w refer to evaluation at the cell faces e and w in Figure A.1.

The surface integrals are then approximated as the product of the integrand and the area of the face surface. For example, the first integral on the right hand side of equation A.4 would be approximated as:

$$\int_{S_e} \rho u \; dS_e = \rho_e u_e S_e \tag{A.5}$$

The algebraic form of the continuity equation can then be expressed as:

$$(\rho u S)_e + (\rho u S)_w = 0 \tag{A.6}$$

Similarly, the momentum equation in the one-dimensional case:

$$\frac{\partial}{\partial x}(\rho u u) = -\frac{\partial p}{\partial x} + \frac{\partial}{\partial x}\left(\mu \frac{\partial u}{\partial x}\right) + F_x \tag{A.7}$$

can be transformed into an algebraic equivalent through volume integration and evaluation to yield the following algebraic equivalent:

$$(\rho u^2 S)_e + (\rho u^2 S)_w = -((pS)_e + (pS)_w) + \left(\mu\left[\frac{u_E - u_P}{\Delta x}\right]S\right)_e + \left(\mu\left[\frac{u_P - u_W}{\Delta x}\right]S\right)_w + F\Delta V \tag{A.8}$$

When the equations of motion (equations 2.1 and 2.2) are integrated over each control volume in a flow domain, a simultaneous set of equations in algebraic form with unknowns in terms of neighboring cell center and cell face values results. A solution to this set of equations is then possible using numerical methods. Of course, FLUENT extends these simplified equations into two or three dimensions depending on the nature of the problem being solved.

Appendix B – FROSTY Experimental Data

FROSTY Collector Measurement	Mass of Fluorescein Extracted from Filters and Collector Surfaces (µg)							
	4 µm drops	4 µm drops	6 µm drops	8 µm drops	10 µm drops	12 µm drops	14 µm drops	16 µm drops
filter 1 (pre-filter)	17.53	12.10	50.25	65.37	74.45	55.56	58.77	38.23
filter 2 (post-filter)	17.90	12.43	49.19	64.09	72.29	54.17	57.76	37.54
Stage 1 - Extraction 1	0.05	0.14	1.41	2.58	6.18	7.74	13.12	13.46
Stage 2 - Extraction 1	0.31	0.29	7.50	17.17	26.74	19.28	20.21	9.48
Stage 3 - Extraction 1	4.03	3.11	27.66	33.97	29.02	11.01	6.84	2.08
Stage 1 Inlet	N/A	N/A	N/A	N/A	0.08	N/A	N/A	N/A
DI	0.00	0.00	0.00	0.00	0.00	0.00	0.00	0.00
Stage 1 - Wall Blank	0.00	0.00	0.00	N/A	N/A	N/A	0.00	N/A
Stage 2 - Wall Blank	0.00	0.00	0.00	N/A	N/A	N/A	0.00	N/A
Stage 3 - Wall Blank	0.00	0.00	0.00	N/A	N/A	N/A	N/A	N/A
Stage 1 - Wall Losses	0.08	0.12	1.50	2.86	N/A	N/A	6.41	N/A
Stage 2 - Wall Losses	0.03	0.04	0.69	1.83	N/A	N/A	1.80	N/A
Stage 3 - Wall Losses	0.42	0.32	1.12	0.12	N/A	N/A	0.09	N/A

FROSTY Collector Measurement	Mass of Fluorescein Extracted from Filters and Collector Surfaces (µg)							
	18 µm drops	18 µm drops	18 µm drops	18 µm drops	18 µm drops	20 µm drops	22 µm drops	24 µm drops
filter 1 (pre-filter)	40.80	46.26	44.16	44.56	46.42	38.42	30.39	21.13
filter 2 (post-filter)	41.23	46.84	44.98	44.41	47.12	39.35	29.63	21.72
Stage 1 - Extraction 1	20.14	22.75	20.89	20.62	25.88	23.85	21.62	17.36
Stage 2 - Extraction 1	7.88	8.57	8.17	7.93	7.93	4.48	1.73	0.75
Stage 3 - Extraction 1	0.96	1.03	0.90	0.88	0.95	0.34	0.11	0.07
Stage 1 Inlet	N/A	N/A	N/A	N/A	N/A	N/A	N/A	0.15
DI	0.00	0.00	-0.01	0.00	-0.01	0.00	0.00	0.00
Stage 1 - Wall Blank	N/A	N/A	0.00	N/A	N/A	N/A	N/A	N/A
Stage 2 - Wall Blank	N/A	N/A	0.00	N/A	N/A	N/A	N/A	N/A
Stage 3 - Wall Blank	N/A	N/A	0.00	N/A	N/A	N/A	N/A	N/A
Stage 1 - Wall Losses	N/A	N/A	5.30	N/A	N/A	N/A	N/A	N/A
Stage 2 - Wall Losses	N/A	N/A	0.78	N/A	N/A	N/A	N/A	N/A
Stage 3 - Wall Losses	N/A	N/A	0.02	N/A	N/A	N/A	N/A	N/A

FROSTY Collector Measurement	Mass of Fluorescein Extracted from Filters and Collector Surfaces (µg)							
	26 µm drops	28 µm drops	28 µm drops	30 µm drops				
filter 1 (pre-filter)	18.44	15.00	12.62	12.19				
filter 2 (post-filter)	19.38	15.25	12.10	12.46				
Stage 1 - Extraction 1	16.06	12.67	10.40	10.76				
Stage 2 - Extraction 1	0.35	0.18	0.17	0.14				
Stage 3 - Extraction 1	0.03	0.04	0.08	0.01				
Stage 1 Inlet	N/A	0.22	N/A	0.25				
DI	0.00	0.00	0.00	0.00				
Stage 1 - Wall Blank	0.00	0.00	N/A	0.00				
Stage 2 - Wall Blank	0.00	0.00	N/A	0.00				
Stage 3 - Wall Blank	0.00	0.00	N/A	0.00				
Stage 1 - Wall Losses	1.12	0.56	N/A	0.38				
Stage 2 - Wall Losses	0.04	0.03	N/A	0.02				
Stage 3 - Wall Losses	0.00	0.00	N/A	0.00				

Fluorescein Collected on Impaction Surfaces, Inlets, and Walls as a Percentage of Total Fluorescein Mass Entering Collector

FROSTY Collector		4 µm drops	4 µm drops	6 µm drops	8 µm drops	10 µm drops	12 µm drops	14 µm drops	16 µm drops
Avgerage fluorescein mass on filters	µg	17.71	12.27	49.72	64.73	73.37	54.86	58.26	37.89
% difference between filters	%	2.11	2.71	2.16	2.01	2.99	2.56	1.73	1.84
Stage 1 Impaction Surface	%	0.28	1.17	2.84	3.99	8.43	14.11	22.52	35.52
Stage 2 Impaction Surface	%	1.74	2.39	15.09	26.53	36.45	35.14	34.69	25.02
Stage 3 Impaction Surface	%	22.76	25.36	55.63	52.48	39.55	20.07	11.74	5.48
Stage 1 Inlet	%	N/A	N/A	N/A	N/A	0.11	N/A	N/A	N/A
Stage 1 Wall	%	0.85	1.93	6.04	8.82	N/A	N/A	22.01	N/A
Stage 2 Wall	%	0.29	0.63	2.77	5.66	N/A	N/A	6.18	N/A
Stage 3 Wall	%	4.77	5.23	4.50	0.37	N/A	N/A	0.29	N/A
total mass collected on 3 stages	µg	4.39	3.55	36.58	53.72	61.94	38.03	40.17	25.02
total mass collected on interstage walls	µg	1.05	0.96	6.62	9.61	N/A	N/A	16.60	N/A
total mass collected on all surfaces	µg	5.44	4.50	43.20	63.33	61.94	38.03	56.77	25.02
% collected on all 3 stages	%	24.78	28.92	73.56	82.99	84.42	69.32	68.95	66.03
% collected on interstage walls	%	5.92	7.79	13.31	14.85	0.00	0.00	28.48	0.00
% collected on all surfaces	%	30.70	36.71	86.87	97.84	84.42	69.32	97.44	66.03

Fluorescein Collected on Impaction Surfaces, Inlets, and Walls as a Percentage of Total Fluorescein Mass Entering Collector

FROSTY Collector		18 µm drops	18 µm drops	18 µm drops	18 µm drops	18 µm drops	20 µm drops	22 µm drops	24 µm drops
Avgerage fluorescein mass on filters	µg	41.02	46.55	44.57	44.49	46.77	38.88	30.01	21.43
% difference between filters	%	1.04	1.25	1.87	0.33	1.51	2.41	2.58	2.77
Stage 1 Impaction Surface	%	49.09	48.89	46.87	46.35	55.32	61.35	72.04	81.02
Stage 2 Impaction Surface	%	19.22	18.41	18.33	17.84	16.96	11.52	5.76	3.50
Stage 3 Impaction Surface	%	2.34	2.22	2.01	1.98	2.03	0.86	0.37	0.34
Stage 1 Inlet	%	N/A	N/A	N/A	N/A	N/A	N/A	N/A	0.69
Stage 1 Wall	%	N/A	N/A	11.88	N/A	N/A	N/A	N/A	N/A
Stage 2 Wall	%	N/A	N/A	1.75	N/A	N/A	N/A	N/A	N/A
Stage 3 Wall	%	N/A	N/A	0.04	N/A	N/A	N/A	N/A	N/A
total mass collected on 3 stages	µg	28.98	32.36	29.96	29.43	34.76	28.67	23.46	18.18
total mass collected on interstage walls	µg	N/A	N/A	12.18	N/A	N/A	N/A	N/A	N/A
total mass collected on all surfaces	µg	28.98	32.36	42.14	29.43	34.76	28.67	23.46	18.18
% collected on all 3 stages	%	70.65	69.52	67.22	66.17	74.31	73.73	78.17	84.86
% collected on interstage walls	%	0.00	0.00	27.34	0.00	0.00	0.00	0.00	0.00
% collected on all surfaces	%	70.65	69.52	94.56	66.17	74.31	73.73	78.17	84.86

Fluorescein Collected on Impaction Surfaces, Inlets, and Walls as a Percentage of Total Fluorescein Mass Entering Collector

FROSTY Collector		26 µm drops	28 µm drops	28 µm drops	30 µm drops				
Avgerage fluorescein mass on filters	µg	18.91	15.12	12.36	12.33				
% difference between filters	%	5.08	1.66	4.33	2.16				
Stage 1 Impaction Surface	%	84.90	83.75	84.18	87.30				
Stage 2 Impaction Surface	%	1.84	1.22	1.38	1.16				
Stage 3 Impaction Surface	%	0.17	0.25	0.69	0.08				
Stage 1 Inlet	%	N/A	1.45	N/A	2.04				
Stage 1 Wall	%	5.94	3.70	N/A	3.08				
Stage 2 Wall	%	0.20	0.17	N/A	0.14				
Stage 3 Wall	%	0.03	0.02	N/A	0.02				
total mass collected on 3 stages	µg	16.44	12.89	10.66	10.91				
total mass collected on interstage walls	µg	2.34	1.18	0.00	0.80				
total mass collected on all surfaces	µg	18.77	14.07	10.66	11.71				
% collected on all 3 stages	%	86.90	85.22	86.24	88.53				
% collected on interstage walls	%	12.35	7.80	0.00	6.49				
% collected on all surfaces	%	99.25	93.01	86.24	95.03				

Appendix C – CSU 5-Stage Experimental Data

CSU 5-Stage Collector Measurement	Mass of Fluorescein Extracted from Filters and Collector Surfaces (µg)							
	4 µm drops	6 µm drops	8 µm drops	10 µm drops	12 µm drops	14 µm drops	16 µm drops	18 µm drops
filter 1 (pre-filter)	21.92	48.34	59.39	64.13	64.45	59.35	37.74	38.89
filter 2 (post-filter)	21.76	46.69	59.49	62.14	63.40	59.72	37.77	40.01
Stage 1 - Extraction 1	0.04	0.11	0.34	0.76	1.31	1.75	3.57	4.83
Stage 2 - Extraction 1	0.06	0.51	1.17	2.85	5.16	7.20	4.77	6.24
Stage 2 - Extraction 1	0.09	1.85	4.49	8.77	12.67	12.06	6.69	6.15
Stage 4 - Extraction 1	0.57	6.44	13.12	12.99	10.27	7.26	2.60	1.58
Stage 5 - Extraction 1	7.77	17.01	12.55	6.52	2.89	1.35	0.48	0.17
DI	0.00	0.00	0.00	0.00	0.00	0.00	0.00	0.00
Stage 1 - Extraction 2	0.00	0.00	0.01	0.03	0.04	0.07	0.12	0.20
Stage 2 - Extraction 2	0.01	0.03	0.03	0.08	0.16	0.17	0.22	0.24
Stage 2 - Extraction 2	0.02	0.06	0.10	0.18	0.30	0.30	0.34	0.27
Stage 4 - Extraction 2	0.01	0.19	0.14	0.17	0.17	0.20	0.07	0.05
Stage 5 - Extraction 2	0.14	0.35	0.20	0.07	0.07	0.05	0.01	0.01
Stage 1 - Blank	0.00	0.01	0.00	0.01	0.01	0.04	0.01	0.00
Stage 2 - Blank	0.01	0.02	0.00	0.03	0.01	0.04	0.01	0.00
Stage 3 - Blank	0.01	0.05	0.00	0.02	0.01	0.03	0.01	0.01
Stage 4 - Blank	0.00	0.02	0.00	0.01	0.00	0.00	0.00	0.02
Stage 5 - Blank	0.00	0.01	0.00	0.01	0.00	0.00	0.00	0.02
Stage 1 Inlet	N/A	N/A	N/A	N/A	N/A	0.02	N/A	N/A
Stg 1 Lid / Stg 2 Inlet	0.04	0.11	0.98	0.61	1.07	2.56	2.36	3.59
Stg 2 Lid / Stg 3 Inlet	0.09	0.27	0.65	1.68	3.58	4.83	3.92	4.34
Stg 3 Lid / Stg4 Inlet	0.13	1.35	4.79	8.18	8.89	7.53	3.62	2.86
Stg 4 Lid / Stg 5 Inlet	0.35	3.38	4.94	4.14	2.77	1.88	0.57	0.29
Stg 5 Lid / Exit	2.35	2.98	1.61	0.66	0.29	0.28	0.05	0.02
Stage 2 Lower Inlet	0.04	0.46	1.06	2.10	1.64	0.76	1.10	1.13
Stage 3 Lower Inlet	0.05	0.41	1.25	1.87	1.28	0.96	0.99	0.89
Stage 4 Lower Inlet	0.22	1.71	2.66	4.23	2.75	N/A	1.24	0.61
Stage 5 Lower Inlet	0.49	1.33	2.64	1.97	0.71	N/A	0.18	0.12
Stage 1 Wall	N/A	0.01	N/A	N/A	N/A	0.03	N/A	N/A
Stage 2 Wall	N/A	0.01	N/A	N/A	N/A	0.07	N/A	N/A
Stage 3 Wall	N/A	0.13	N/A	N/A	N/A	N/A	N/A	N/A
Stage 4 Wall	N/A	0.58	N/A	N/A	N/A	N/A	N/A	N/A
Stage 5 Wall	N/A	0.46	N/A	N/A	N/A	N/A	N/A	N/A

CSU 5-Stage Collector Measurement	Mass of Fluorescein Extracted from Filters and Collector Surfaces (µg)							
	20 µm drops	22 µm drops	24 µm drops	26 µm drops	28 µm drops	30 µm drops	32 µm drops	34 µm drops
filter 1 (pre-filter)	53.36	36.42	32.38	11.88	8.31	8.76	8.23	9.68
filter 2 (post-filter)	54.80	36.01	32.15	11.93	8.17	8.82	8.52	9.89
Stage 1 - Extraction 1	11.65	7.76	12.29	5.74	4.09	4.69	4.46	5.65
Stage 2 - Extraction 1	8.19	6.57	4.96	1.55	0.96	0.78	0.78	0.77
Stage 2 - Extraction 1	6.58	3.94	2.34	0.51	0.31	0.21	0.16	0.14
Stage 4 - Extraction 1	1.58	0.63	0.27	0.04	0.04	0.01	0.01	0.01
Stage 5 - Extraction 1	0.11	0.03	0.04	0.00	0.01	0.02	0.01	0.00
DI	0.00	0.00	0.00	0.00	0.00	0.00	0.00	0.00
Stage 1 - Extraction 2	0.52	0.47	0.42	0.24	0.35	0.24	0.21	0.31
Stage 2 - Extraction 2	0.31	0.42	0.21	0.08	0.07	0.05	0.05	0.05
Stage 2 - Extraction 2	0.58	0.34	0.11	0.03	0.03	0.02	0.02	0.01
Stage 4 - Extraction 2	0.06	0.03	0.02	0.00	0.01	0.00	0.00	0.00
Stage 5 - Extraction 2	0.01	0.00	0.01	0.00	0.00	0.00	0.00	0.00
Stage 1 - Blank	0.04	0.10	0.01	0.01	0.01	0.00	0.01	0.01
Stage 2 - Blank	0.03	0.06	0.01	0.01	0.03	0.00	0.01	0.02
Stage 3 - Blank	0.05	0.08	0.01	0.00	0.02	0.00	0.01	0.01
Stage 4 - Blank	0.01	0.02	0.01	0.00	0.01	0.00	0.00	0.00
Stage 5 - Blank	0.00	0.00	0.01	0.00	0.01	0.01	0.00	0.00
Stage 1 Inlet	N/A	N/A	N/A	0.01	N/A	N/A	0.13	0.07
Stg 1 Lid / Stg 2 Inlet	5.95	4.77	4.57	1.54	1.35	1.18	1.12	1.24
Stg 2 Lid / Stg 3 Inlet	5.23	3.99	2.75	0.76	0.44	0.37	0.33	0.33
Stg 3 Lid / Stg4 Inlet	2.78	1.48	0.75	0.16	0.08	0.06	0.06	0.06
Stg 4 Lid / Stg 5 Inlet	0.27	0.13	0.08	0.02	0.02	0.02	0.04	0.05
Stg 5 Lid / Exit	0.04	0.03	0.03	0.02	0.02	0.01	0.03	0.01
Stage 2 Lower Inlet	N/A	N/A	0.67	0.23	0.14	0.10	0.11	0.13
Stage 3 Lower Inlet	N/A	N/A	0.49	0.13	0.08	0.06	0.05	0.05
Stage 4 Lower Inlet	N/A	N/A	0.20	0.02	0.03	0.02	0.01	0.01
Stage 5 Lower Inlet	N/A	N/A	0.03	0.02	0.03	0.01	0.01	0.01
Stage 1 Wall	N/A	N/A	N/A	N/A	0.02	0.01	N/A	N/A
Stage 2 Wall	N/A	N/A	N/A	N/A	0.04	0.02	N/A	N/A
Stage 3 Wall	N/A	N/A	N/A	N/A	N/A	N/A	N/A	N/A
Stage 4 Wall	N/A	N/A	N/A	N/A	N/A	N/A	N/A	N/A
Stage 5 Wall	N/A	N/A	N/A	N/A	N/A	N/A	N/A	N/A

Fluorescein Collected on Impaction Surfaces, Inlets, and Walls as a Percentage of Total Fluorescein Mass entering Collector

		4 µm drops	6 µm drops	8 µm drops	10 µm drops	12 µm drops	14 µm drops	16 µm drops	18 µm drops
Avgerage fluorescein mass on filters	µg	21.84	47.52	59.44	63.13	63.93	59.53	37.76	39.45
% difference between filters	%	0.75	3.52	0.17	3.20	1.65	0.63	0.08	2.89
Stage 1 Impaction Surface	%	0.21	0.23	0.59	1.25	2.11	3.05	9.78	12.75
Stage 2 Impaction Surface	%	0.33	1.13	2.02	4.64	8.33	12.38	13.21	16.43
Stage 3 Impaction Surface	%	0.48	4.02	7.73	14.18	20.29	20.75	18.63	16.27
Stage 4 Impaction Surface	%	2.66	13.96	22.30	20.84	16.33	12.54	7.09	4.14
Stage 5 Impaction Surface	%	36.23	36.53	21.45	10.43	4.63	2.34	1.30	0.45
Stage 1 Inlet	%	N/A	N/A	N/A	N/A	N/A	0.04	N/A	N/A
Stg 1 Lid / Stg 2 Inlet	%	0.19	0.22	1.65	0.97	1.67	4.30	6.25	9.10
Stg 2 Lid / Stg 3 Inlet	%	0.40	0.57	1.09	2.65	5.59	8.11	10.38	11.01
Stg 3 Lid / Stg4 Inlet	%	0.59	2.84	8.06	12.96	13.91	12.64	9.59	7.26
Stg 4 Lid / Stg 5 Inlet	%	1.62	7.11	8.30	6.56	4.34	3.15	1.52	0.74
Stg 5 Lid / Exit	%	10.76	6.27	2.72	1.04	0.45	0.48	0.12	0.06
Stage 2 Lower Inlet	%	0.19	0.97	1.78	3.32	2.56	1.28	2.91	2.86
Stage 3 Lower Inlet	%	0.21	0.86	2.11	2.96	2.01	1.62	2.63	2.25
Stage 4 Lower Inlet	%	1.02	3.61	4.47	6.70	4.30	N/A	3.29	1.55
Stage 5 Lower Inlet	%	2.24	2.80	4.43	3.12	1.11	N/A	0.47	0.30
Stage 1 Wall	%	N/A	0.02	N/A	N/A	N/A	0.05	N/A	N/A
Stage 2 Wall	%	N/A	0.03	N/A	N/A	N/A	0.11	N/A	N/A
Stage 3 Wall	%	N/A	0.28	N/A	N/A	N/A	N/A	N/A	N/A
Stage 4 Wall	%	N/A	1.22	N/A	N/A	N/A	N/A	N/A	N/A
Stage 5 Wall	%	N/A	0.96	N/A	N/A	N/A	N/A	N/A	N/A
total mass collected on 5 stages	µg	8.72	26.55	32.15	32.42	33.05	30.40	18.88	19.74
total mass collected on lids/inlets	µg	2.96	8.09	12.97	15.27	16.60	17.10	10.52	11.11
total mass collected on lower inlets	µg	0.80	3.92	7.61	10.17	6.38	1.72	3.51	2.75
total mass collected on walls	µg	0.00	1.19	0.00	0.00	0.00	0.10	0.00	0.00
total mass collected on all surfaces	µg	12.48	39.75	52.73	57.85	56.02	49.33	32.92	33.60
% collected on all 5 stages	%	39.91	55.87	54.09	51.35	51.69	51.07	50.01	50.04
% collected on interstage walls	%	17.21	27.77	34.62	40.29	35.94	31.79	37.17	35.13
% collected on all surfaces	%	57.12	83.65	88.70	91.63	87.64	82.86	87.18	85.17

Fluorescein Collected on Impaction Surfaces, Inlets, and Walls as a Percentage of Total Fluorescein Mass entering Collector

		20 µm drops	22 µm drops	24 µm drops	26 µm drops	28 µm drops	30 µm drops	32 µm drops	34 µm drops
Avgerage fluorescein mass on filters	µg	54.08	36.21	32.26	11.91	8.24	8.79	8.38	9.79
% difference between filters	%	2.69	1.14	0.72	0.42	1.74	0.71	3.48	2.20
Stage 1 Impaction Surface	%	22.50	22.73	39.38	50.23	53.82	56.12	55.67	60.94
Stage 2 Impaction Surface	%	15.70	19.30	16.03	13.65	12.58	9.45	9.94	8.35
Stage 3 Impaction Surface	%	13.23	11.83	7.59	4.52	4.15	2.54	2.14	1.54
Stage 4 Impaction Surface	%	3.04	1.83	0.89	0.34	0.60	0.14	0.14	0.12
Stage 5 Impaction Surface	%	0.22	0.09	0.14	0.05	0.20	0.18	0.08	0.06
Stage 1 Inlet	%	N/A	N/A	N/A	0.08	N/A	N/A	1.57	0.76
Stg 1 Lid / Stg 2 Inlet	%	11.00	13.16	14.16	12.93	16.35	13.41	13.37	12.72
Stg 2 Lid / Stg 3 Inlet	%	9.67	11.01	8.52	6.35	5.39	4.18	3.96	3.36
Stg 3 Lid / Stg4 Inlet	%	5.14	4.10	2.33	1.35	0.98	0.67	0.74	0.57
Stg 4 Lid / Stg 5 Inlet	%	0.49	0.35	0.24	0.20	0.24	0.25	0.51	0.54
Stg 5 Lid / Exit	%	0.08	0.08	0.10	0.15	0.23	0.15	0.34	0.09
Stage 2 Lower Inlet	%	N/A	N/A	2.08	1.93	1.66	1.16	1.31	1.28
Stage 3 Lower Inlet	%	N/A	N/A	1.52	1.07	1.00	0.63	0.64	0.47
Stage 4 Lower Inlet	%	N/A	N/A	0.63	0.20	0.41	0.18	0.18	0.11
Stage 5 Lower Inlet	%	N/A	N/A	0.10	0.13	0.35	0.11	0.12	0.05
Stage 1 Wall	%	N/A	N/A	N/A	N/A	0.20	0.16	N/A	N/A
Stage 2 Wall	%	N/A	N/A	N/A	N/A	0.51	0.25	N/A	N/A
Stage 3 Wall	%	N/A	N/A	N/A	N/A	N/A	N/A	N/A	N/A
Stage 4 Wall	%	N/A	N/A	N/A	N/A	N/A	N/A	N/A	N/A
Stage 5 Wall	%	N/A	N/A	N/A	N/A	N/A	N/A	N/A	N/A
total mass collected on 5 stages	µg	29.57	20.20	20.66	8.19	5.88	6.01	5.70	6.95
total mass collected on lids/inlets	µg	14.27	10.39	8.18	2.51	1.91	1.64	1.72	1.77
total mass collected on lower inlets	µg	0.00	0.00	1.40	0.40	0.28	0.18	0.19	0.19
total mass collected on walls	µg	0.00	0.00	0.00	0.00	0.06	0.04	0.00	0.00
total mass collected on all surfaces	µg	43.85	30.59	30.23	11.10	8.13	7.87	7.60	8.90
% collected on all 5 stages	%	54.69	55.77	64.03	68.80	71.35	68.42	67.97	71.01
% collected on interstage walls	%	26.39	28.70	29.67	24.38	27.33	21.16	22.75	19.95
% collected on all surfaces	%	81.07	84.47	93.71	93.18	98.68	89.58	90.72	90.96

Appendix D – FLUENT Operational Flowchart

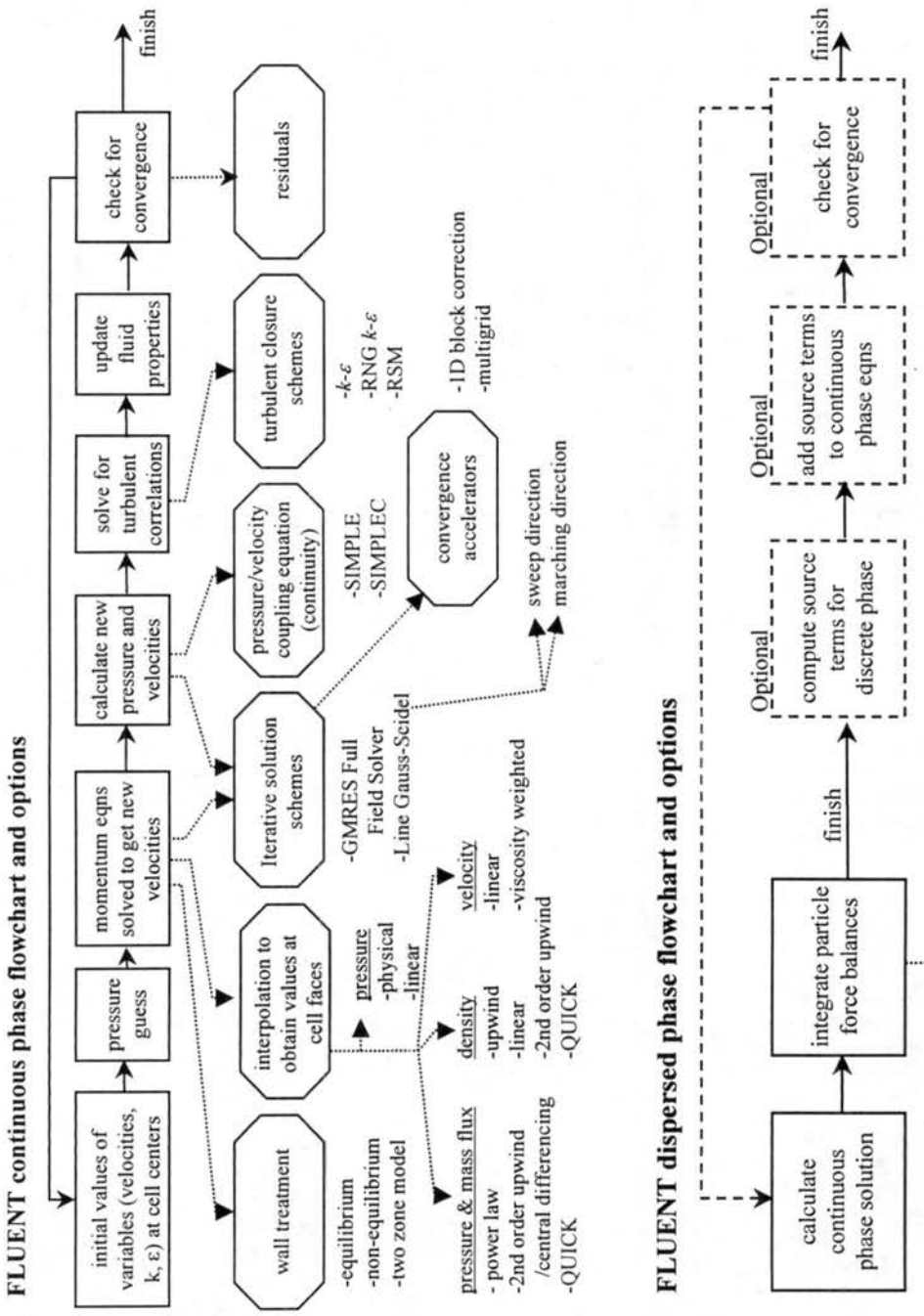

Appendix E – FLUENT Model Files

FROSTY .cas& .dat files	stages modeled	turbulence model	wall treatment	inlet vel ft/s	density lbm/ft^3	dyn. visc lbm/ft s	turb int %	char length ft	press/vel coupling	interpolation scheme	solver	comments
frosty_1a	1	ke	std	17.49	7.647E-02	6.048E-04	3	0.167	SIMPLE	power law	LGS	problems with convergence due to inlet fillet
frosty_1b	1	RNG ke	std	17.49	7.647E-02	6.048E-04	3	0.167	SIMPLE	power law	LGS	removed inlet fillet
frosty_1c	1	RNG ke	non-equil	17.49	7.647E-02	6.048E-04	3	0.167	SIMPLE	power law	LGS	(wrong geom?)
frosty_1d	1	RNG ke	non-equil	18.86	5.676E-02	1.138E-05	3	0.05	SIMPLE	power law	LGS	corrected inlet velocity, corrected for 3000m conditions
frosty_1e	1	RNG ke	2 zone	18.86	5.676E-02	1.138E-05	3	0.05	SIMPLE	power law	LGS	tried 2 zone wall treatment
frosty_1f	1	RNG ke	non-equil	18.86	5.676E-02	1.138E-05	3	0.05	SIMPLE	power law	LGS	finer mesh
frosty_1g	1	RNG ke	non-equil	18.86	5.676E-02	1.138E-05	3	0.05	SIMPLE	power law	LGS	same as frosty_1d (file was corrupted)
frosty_1h	1	RNG ke	non-equil	18.86	5.676E-02	1.138E-05	1	0.05	SIMPLE	power law	LGS	tried new turb. intensity to see its effect on particle motion
frosty_1i	1	RMS	non-equil	18.86	5.676E-02	1.138E-05	1	0.05	SIMPLE	power law	LGS	tried RSM
frosty_1j	1	RNG ke	non-equil	18.86	5.676E-02	1.138E-05	1	0.05	SIMPLE	QUICK	LGS	same as frosty_1j but with QUICK
frosty_1k	1	RSM	non-equil	18.86	5.676E-02	1.138E-05	1	0.05	SIMPLE	QUICK	LGS	tried RSM with QUICK
frosty_1l	1	RNG ke	non-equil	18.86	5.676E-02	1.138E-05	3	0.05	SIMPLE	power law	LGS	reduced grid spacing at impaction surface for wall treatment study
frosty_1m	1	RSM	non-equil	18.86	5.676E-02	1.138E-05	3	0.05	SIMPLE	power law	LGS	RSM on fine mesh
frosty_1n	1	RSM	non-equil	18.86	5.676E-02	1.138E-05	3	0.05	SIMPLE	QUICK	LGS	RSM on fine mesh w/ QUICK
frosty_1o	1	RNG ke	non-equil	18.86	5.676E-02	1.138E-05	3	0.05	SIMPLE	QUICK	LGS	RNG on fine mesh w/ QUICK
frosty_1p	1	RNG ke?	non-equil	18.86	5.676E-02	1.138E-05	3	0.05	SIMPLE	power law?	LGS	inlet meshed / pressure inlets (corrupted file)
frosty_1q	1	RSM	non-equil	18.86	5.676E-02	1.138E-05	3	0.05	SIMPLE	QUICK	LGS	inlet meshed / pressure inlets
frosty_1r	1	RSM	non-equil	18.86	5.676E-02	1.138E-05	3	0.05	SIMPLE	QUICK	LGS	same as _1n but coarse mesh
frosty_12a	1-2	RNG ke	non-equil	18.86	5.676E-02	1.138E-05	3	0.05	SIMPLE	power law	LGS	stages 1 and 2
frosty_13	1-3	RNG ke	non-equil	18.86	5.676E-02	1.138E-05	3	0.05	SIMPLE	power law	LGS	stages 1, 2, and 3
frosty_13a	1-3	RMS	non-equil	18.86	5.676E-02	1.138E-05	3	0.05	SIMPLE	power law	LGS	same as frosty_13 but with RMS
frosty_13b	1-3	RMS	non-equil	18.86	5.676E-02	1.138E-05	3	0.05	SIMPLE	QUICK	LGS	same as frosty_13a but with QUICK
frosty_13c	1-3	RMS	non-equil	18.86	5.676E-02	1.138E-05	3	0.05	SIMPLE	power law	LGS	remeshed stage 3 inlet
frosty_13d	1-3	RMS	non-equil	18.86	5.676E-02	1.138E-05	3	0.05	SIMPLE	QUICK	LGS	same as frosty_13c but with QUICK
frosty_13e	1-3	RMS	non-equil	18.86	6.31E-02	1.23E-05	3	0.05	SIMPLE	QUICK	LGS	modeled at Simlab conditions
frosty_1dbl	1-3	RMS	non-equil	18.86	6.31E-02	1.23E-05	3	0.05	SIMPLE	QUICK	LGS	mesh density increased by 1.5

5-Stage .cas& .dat files	stages modeled	turbulence model	wall treatment	inlet vel ft/s	density lbm/ft^3	dyn. visc lbm/ft s	turb int %	char length ft	press/vel coupling	interpolation scheme	solver	comments
stage_12a.cas/ _12a.dat	1-2	RSM	non-equil	4.09	7.66E-02	1.204E-05	3	0.167	SIMPLE	Power Law	LGS	test runs of stages 1&2
stage_12a.cas/ _12b.dat	1-2	RSM	non-equil	4.09	7.66E-02	1.204E-05	10	0.167	SIMPLE	QUICK	LGS	changed to QUICK interpolation / sea level std. Atmos.
stage_12a.cas/ _12c.dat	1-2	RSM	non-equil	4.09	7.66E-02	1.204E-05	3	0.167	SIMPLE	QUICK	LGS	included viscosity-weighted velocity interpolation
stage_12a.cas/ _12d.dat	1-2	RSM	non-equil	4.09	7.66E-02	1.204E-05	3	0.167	SIMPLE	QUICK	LGS	included directional diffusivity
stage_12dbl	1-2	RSM	non-equil	4.09	7.66E-02	1.204E-05	3	0.083	SIMPLE	QUICK	LGS	mesh refined
stage_13	1-3	RSM	non-equil	3.81	7.65E-02	1.203E-05	3	0.083	SIMPLE	QUICK	LGS	new inlet velocity, μ, density / 3 stages modeled
stage_15a	1-5	RSM	non-equil	3.81	7.65E-02	1.203E-05	3	0.083	SIMPLE	QUICK	LGS	all 5 stages modeled
stage_15b	1-5	RSM	non-equil	3.81	7.65E-02	1.203E-05	3	0.083	SIMPLE	QUICK	LGS	mesh density increased by 1.5
stage_15c	1-5	RSM	non-equil	3.81	6.31E-02	1.230E-05	3	0.083	SIMPLE	QUICK	LGS	Simlab conditions
stage_15c.cas/ _15c1.dat	1-5	RSM	non-equil	4.104	6.31E-02	1.230E-05	3	0.083	SIMPLE	QUICK	LGS	corrected inlet velocity and gravity terms
stage_15c.cas/ _15c2.dat	1-5	RSM	non-equil	4.104	6.31E-02	1.230E-05	3	0.083	SIMPLE	QUICK	LGS	included directional diffusivity and viscosity weighted vel. interp.
stage_15d	1-5	RSM	non-equil	4.104	6.31E-02	1.230E-05	3	0.083	SIMPLE	QUICK	LGS	renumbered walls to match experimental work
stage_15e	1-5	RSM	non-equil	4.104	7.65E-02	1.203E-05	3	0.083	SIMPLE	QUICK	LGS	same as stage_15d but at sea level conditions